

A SCUBA-2 SURVEY OF HIGH-REDSHIFT GALAXY
PROTOCLUSTERS & THE CALIBRATION OF THE JCMT
TRANSIENT REGIONS

by

Kevin M. Lacaille

Submitted in partial fulfillment of the requirements
for the degree of Master of Science

at

Dalhousie University
Halifax, Nova Scotia
April 2017

© Copyright by Kevin M. Lacaille, 2017

Table of Contents

List of Tables	iv
List of Figures	v
Abstract	vi
List of Abbreviations and Units Used	vii
Acknowledgements	viii
Chapter 1 Introduction	1
1.1 Sub-Millimetre Astronomy	1
1.2 Sub-Millimetre Galaxies	2
1.2.1 Spectral Energy Distribution	6
1.2.2 Negative K-Correction	10
1.3 Protostars	13
1.3.1 The Low Luminosity Problem	14
1.3.2 Variability	16
1.3.3 JCMT Transient Survey	16
1.4 Instrumentation & Data Reduction	17
1.4.1 JCMT	17
1.4.2 SCUBA-2	19
1.4.3 SCUBA-2 Data Reduction	23
Chapter 2 A SCUBA-2 Survey for Luminous Far-Infrared Galaxies in Protoclusters at $z > 2$	24
2.1 Introduction	24
2.2 Observations and Data Reduction	25
2.2.1 SCUBA-2 Observations	25
2.2.2 SMA Observations	26
2.2.3 Gemini GNIRS	26
2.2.4 Auxiliary Data	27
2.3 Results	28

2.3.1	Sub-Millimetre Source Detection	28
2.3.2	Number Counts	28
2.3.3	Counterpart Identification	33
2.4	Discussion	35
2.4.1	Cluster Membership	35
2.4.2	Star-Formation Activity	40
2.5	Conclusions	44
Chapter 3	The JCMT Transient Survey: Data Reduction and Cali-	
	bration Methods	46
3.1	Introduction	46
3.2	Observations	48
3.3	Data Reduction Methods	49
3.4	Image Alignment	54
3.4.1	The GAUSSCLUMPS Method	55
3.4.2	The Cross Correlation Method	56
3.5	Results	58
3.6	Discussion	58
3.7	Conclusions	63
Chapter 4	Conclusion	65
4.1	Chapter 2: A SCUBA-2 Survey for Luminous Far-Infrared Galaxies in	
	Protoclusters at $z > 2$	65
4.2	Chapter 3: The JCMT Transient Survey: Data Reduction and Cali-	
	bration Methods	65
Bibliography		66
Appendix A		78
HS1549	Cutouts	79
HS1700	Cutouts	84

List of Tables

2.1	HS1549 850 μm source catalogue	30
2.2	HS1700 850 μm source catalogue	31
2.3	IRAC counterparts for SCUBA-2 sources in HS1549	36
2.4	IRAC counterparts for SCUBA-2 sources in HS1700	37
2.5	Estimated star formation rates for contributing sources.	41
3.1	JCMT Transient Survey regions	52

List of Figures

1.1	Schematic diagram of sub-millimetre radiation	4
1.2	Lookback time of the Universe	5
1.3	Spectral energy distribution of an SMG	7
1.4	Negative K-correction at $850 \mu\text{m}$	12
1.5	Bolometric luminosity temperature plot for protostars	15
1.6	JCMT and SCUBA-2	20
1.7	Atmospheric transmission on Mauna Kea	21
1.8	SCUBA-2 scanning patterns	22
2.1	HS1549 and HS1700 with SCUBA-2	29
2.2	Cumulative number counts of $> 4\sigma$ $850 \mu\text{m}$	34
2.3	Mass normalized total star-formation rate	43
3.1	Four of the Transient fields	50
3.2	Four of the Transient fields	51
3.3	Ophiuchus Core region with different reduction methods	54
3.4	Example cross correlation of IC348	57
3.5	Offset distributions for the Cross Correlation method and the GAUSSCLUMPS method	60
3.6	Properties of the Cross Correlation method	61
3.7	Reliability of the Cross Correlation method and the GAUSS-CLUMPS method between reductions	62

Abstract

Part 1)

The brightest high-redshift sub-millimetre galaxies (SMGs) represent the rarest and most extreme star-forming events in the Universe and are thought to be the progenitors to some of the most massive local galaxies. While short-lived, these SMGs contain intense stellar nurseries which are host to enormous starburst events and hence greatly affect the Universe's evolution. The most active SMGs are found in protoclusters, the progenitors of the most massive local ($z = 0$) galaxy clusters. I present a sub-millimetre study of two high-redshift ($z > 2$) protoclusters in attempt to understand how galaxy assembly is accelerated in over-dense environments at the peak epoch of star formation. These protoclusters are the richest galaxy over-densities ever detected at $z > 2$, containing at least 15 SMGs with immense star formation rates (SFRs), $600 < \text{SFR} < 2000 \text{ M}_\odot \text{ yr}^{-1}$. By analyzing the distribution of these SMGs we find their host protoclusters collectively form over $23,000 \text{ M}_\odot \text{ yr}^{-1}$, and generate star formation rate densities (SFRDs) over 10,000 times larger than global SFRDs found at their respective epochs. These high-redshift protoclusters could help explain the galaxy assembly mechanisms that generated the massive galaxy clusters we see today at $z = 0$.

Part 2)

Though there has been a significant amount of work investigating the early stages of low-mass star formation in recent years, the evolution of the mass accretion rate remains largely unconstrained. Examining in depth the variation in the rate at which mass is assembled onto the central protostar is critical to understanding the physics of star formation. Instabilities in the outer and inner circumstellar disk can lead to episodic outbursts and observing these periodic brightness variations at infrared or sub-millimetre wavelengths sets constraints on the current accretion models. The JCMT Transient Survey is a three-year project dedicated to studying the variability of deeply embedded protostars in eight nearby star-forming regions at a one month cadence. We use the SCUBA-2 instrument to simultaneously observe these regions at wavelengths of $450 \mu\text{m}$ and $850 \mu\text{m}$. I present the survey's data reduction techniques and propose an improvement on their post-calibration image alignment methods for $850 \mu\text{m}$ data. The new Cross Correlation method achieves reliable spatial alignment of $0.03''$ ($100\times$ smaller than a pixel). This new spacial alignment algorithm proves to outperform the survey's current method to all degrees and will be implemented for the next Transient data release.

List of Abbreviations and Units Used

SCUBA-2	Sub-Millimetre Common User Bolometer Array 2
JCMT	James Clerk Maxwell Telescope
SMA	Sub-Millimetre Array
IRAC	The Infrared Array Camera
SMG	Sub-millimetre galaxy
SED	Spectral energy distribution
SNR	Signal-to-noise ratio
SFR	Star formation rate
SFRD	Star formation rate density
z	Redshift
\odot	Solar units
L_{\odot}	Solar luminosity
M_{\odot}	Solar mass
$'$	Arcminute
$''$	Arcsecond
Jy	Jansky
τ	Opacity
α	Right ascension
δ	Declination
pc	Parsec

Acknowledgements

First and foremost, I would like to thank my supervisor and friend Dr. Scott Chapman for the six incredible years of research. Not many professors would take the risk of taking on an undergraduate student after completing only their first year, but Scott has put so much trust in me and I could not be more grateful. Scott has given me the opportunity to work with the top scientists in the field, travel to Hawai'i to work with and on some of the world's leading sub-millimetre observatories. I will always be grateful for everything Scott has given to me, and I look forward to working in collaboration with him in the future.

I'd like to thank the East Asian Observatory for being gracious hosts during my six month stay in Hawai'i from January to July, 2016. Specifically, I'd like to thank Sarah Graves and Jessica Dempsey for being incredible co-supervisors, their seemingly unlimited amount of knowledge and caring personalities made my time at the EAO very useful. I would like to thank William Montgomerie and Jim Hoge for the amazing experiences at the summit. I'd also like to thank Geoff Bower at SMA/ASIAA for getting me involved in the JCMT Transient Survey.

My lab mates Tim Miller, Kaja Rotermund, and Colin Ross, and my great friend Simon Meynell for the useful discussions and the endless help and motivation these past six years.

Last, but certainly not least I'd like to thank my parents and my family for their never ending love and support.

Chapter 1

Introduction

1.1 Sub-Millimetre Astronomy

Sub-millimeter astronomy is a relatively new branch of observational astronomy, which deals primarily with radiation between wavelengths of 0.3 and 1 mm. This range is particularly important in understanding cold dust and gas in the high redshift universe because the blackbody emission from low temperature dust peaks in this region. Likewise, higher energy emission from young stars is generally reradiated by dust in the sub-millimetre range, which makes it an excellent probe of both star formation, and the interstellar medium.

Observations at sub-millimeter wavelengths have been undertaken by a wide variety of instruments both from the ground and in space. Sub-millimetre telescopes are comprised of either large, single dishes such as the James Clerk Maxwell Telescope (JCMT), or higher resolution multi-antennae interferometers like the Sub-Millimetre Array (SMA) or the Atacama Large Millimeter/Sub-Millimetre Array (ALMA). Space based sub-millimeter telescopes such as the *Herschel Space Observatory* have also been useful because they remove the problems with water vapour absorption in the Earth's atmosphere. Sub-millimetre astronomy has also been conducted from near-space telescopes, which use airborne telescopes to mitigate atmospheric problems. One of these near-space telescopes is the Stratospheric Observatory for Infrared Astronomy (SOFIA), which incorporates a 2.5 meter telescope attached to a modified Boeing 747SP wide-body aircraft. Another is the Balloon-borne Large Aperture Submillimeter Telescope (BLAST), which uses a 2 metre, sub-millimetre telescope attached to a high altitude monitoring balloon.

Continuum emission at sub-millimeter wavelengths has been historically difficult

to observe and combines methods used by both optical and radio telescopes. The detectors used in sub-millimeter telescopes generally use bolometer arrays, which employ materials with temperature-dependent resistance to measure incident radiation and has proven to be extremely effective at these wavelengths. Bolometer arrays usually consist of transition edge sensors (TES) and Superconducting Quantum Interface Device (SQUID) amplifiers. A TES array works by cooling the sensors to their sub-kelvin transition temperatures, where a small change in temperature from an incident photon will create a relatively small, but measurable change in resistance of the sensor. The signal is then boosted by a SQUID amplifier, which is a very sensitive magnetometer that boosts the faint electrical signal to assist in readout.

Though sub-millimetre astronomy is a relatively new field, sub-millimetre wavelength surveys have established an important role for understanding the assembly of stellar mass and the evolution of massive dusty, star-forming galaxies in the Universe. The most luminous of these galaxies, seen all the way back to just ~ 800 Myr after the Big Bang [19], have far-infrared luminosities greater than $10^{13} L_{\odot}$ ¹, with implied star-formation rates of thousands of solar masses per year [65], [10]. In comparison, these galaxies are over 1000 times brighter than our own galaxy, the Milky Way, forming stars thousands of times quicker than our own galaxy. Since their discovery, sub-millimetre detected galaxies residing in the early Universe (high redshift) have become a critical piece of the puzzle in our understanding of the cosmic galaxy formation and evolution.

1.2 Sub-Millimetre Galaxies

A key goal of modern cosmology is to understand how gravitationally bound structures, namely galaxies and galaxy clusters, and their constituent star populations formed from an initially uniform Universe and how they have evolved since then. To answer this question, cosmologists seek to obtain data from all observable wavelengths, and in combination with numerical simulations, attempt to derive a solution.

¹ \odot : Solar. e.g. L_{\odot} means the luminosity of the Sun.

Massive galaxy cluster cores are well-characterized by populations of passive, early-type galaxies (i.e. elliptical galaxies), whose properties distinctly contrast with the star forming galaxies found in surrounding lower-density fields [10]. The key formation phase of elliptical galaxies that exist in local clusters appears to have occurred in the early parts of the Universe, namely at redshifts $z > 2$ [37]. Galaxies with low star formation rates are predominately found in dense environments at $z \lesssim 1$ [37]. Observations made at $z > 1$ suggest that progenitors of local galaxy clusters, proto-clusters, should be structures of gravitationally bound dusty red galaxies existing in over-dense regions of space. However, studies have shown that the *star formation – galaxy density* relation could begin to weaken at the $z \sim 2$ epoch [76], [8], [37], [28], [86], [61], [51]. By analyzing star formation as a function of spatial mass distribution around this epoch may help provide strong constraints on galaxy formation and evolution [35].

A sub-millimetre galaxy (SMG) is a distant, dusty, active (star-forming) galaxy whose emissions are predominately in sub-millimetre wavelengths. When new stars are formed in massive, cold dust clouds they emit high-energy ultraviolet radiation, which then gets absorbed by the surrounding dust, consequently heating up the dust and re-radiating as thermal radiation in the infrared. As the infrared radiation travels through the Universe it gets doppler shifted to the red end of the spectrum in the sub-millimetre, which is known as red shifting (see Figure 1.1). The amount the light gets redshifted by is $\lambda_{\text{observed}} = (1 + z)\lambda_{\text{emitted}}$. SMGs are some of the most active star-forming galaxies in the Universe, and as a result most of an SMG’s energy is projected as thermal radiation [8].

Astronomers use light travel time as a proxy for distance, since the speed of light is finite. Since the Universe is expanding the more distant the object the more doppler shifted it’s light emission will be in the red end of the spectrum. As a result, in astronomy redshift, z , is used as a proxy for light travel time, and consequently distance. Figure 1.2 shows how lookback time, e.g. light travel time, acts as a function of redshift. This figure also gives a brief outline of cosmologically significant epochs.

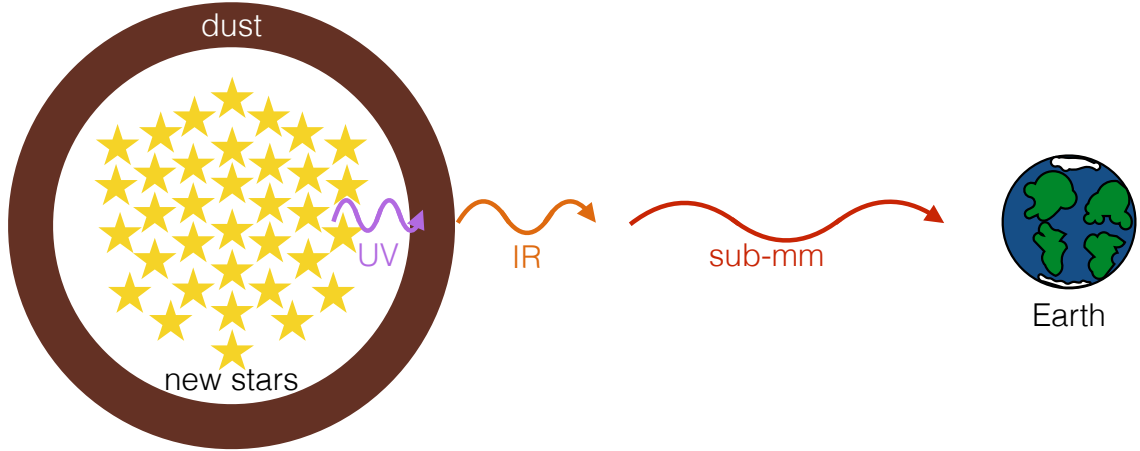


Figure 1.1: Schematic diagram (not to scale) of the process at which sub-millimetre radiation is observed from a distant, dusty, star-forming galaxy (e.g. an SMG).

When the Universe was only about 200 million years old the first stars began to form [72], and it wasn't until about another 200 million years later when the first galaxies began to form [10]. As time progressed, the Universe continued to expand and galaxies began to clump into gravitationally bound structures, known as galaxy protoclusters.

Blank-field millimetre and sub-millimetre continuum surveys have discovered hundreds of distant, dusty, star-forming SMGs over the past decade [8], [17], [12], [16], [33]. Large-scale sub-millimetre surveys have mapped almost 10^3 deg^2 in 500, 350, 250 μm wavelengths (e.g. *Herschel-SPIRE*) [15] where nearly $\sim 10^4$ SMGs have been being detected [10]. The search for the most luminous star forming galaxies in the Universe is an ongoing and exciting part of modern astrophysics, however some of the SMGs discovered in the first large-scale surveys still remain the brightest, most extreme stellar nurseries ever discovered [10].

The problem, however is no longer discovering these bright SMGs, but it has to do with their spacial distribution, namely their redshifts. Due to their inherently dusty environment and morphology, determining the redshifts of SMGs has posed great difficulty. SMGs have weak counterparts in the rest-frame ultraviolet and optical to make spectroscopic redshift measurements biased to only optically bright SMGs. By combining near- and mid-infrared (IR) photometry we're able to obtain reliable

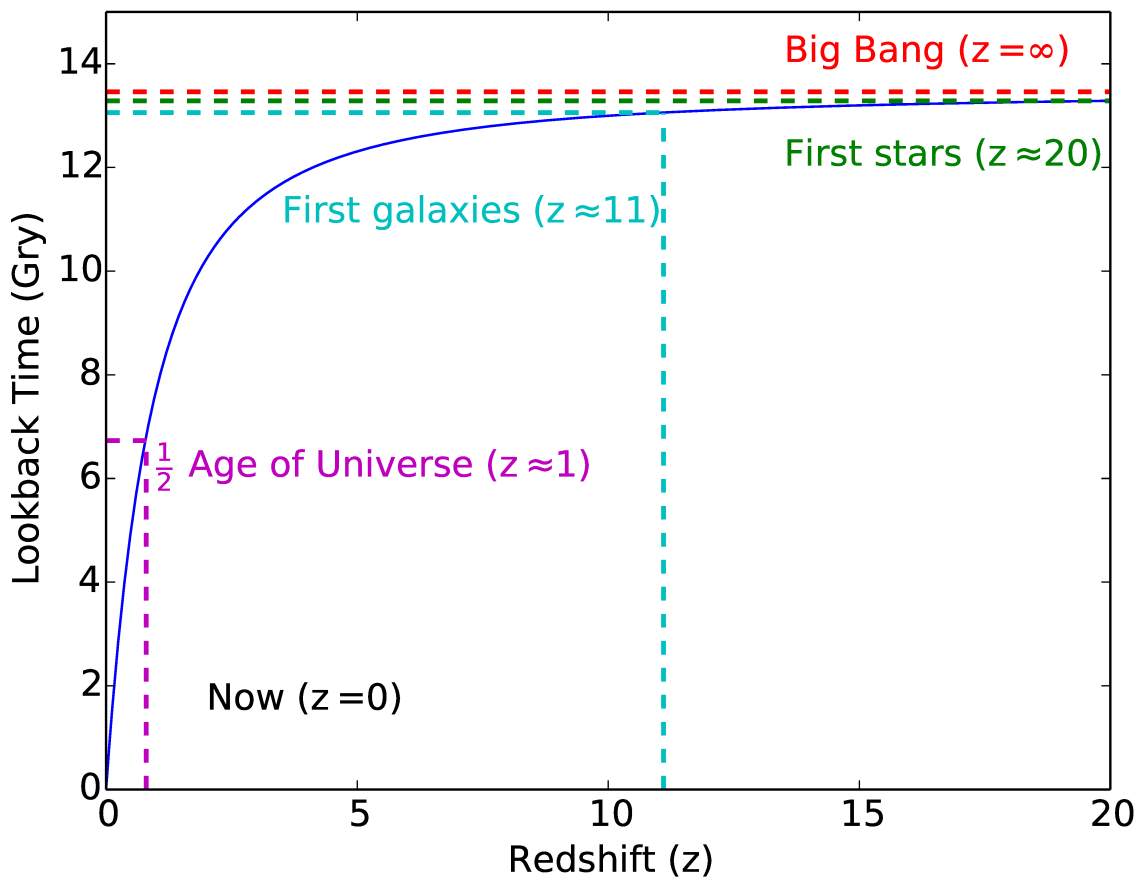


Figure 1.2: Lookback time for a flat Universe estimated using ASTROPY [64].

photometric redshift estimates. Nevertheless, due to their intrinsic dusty properties SMGs have high extinction resulting in very faint counterparts in the optical/near-IR. As a result not only are the spectroscopic redshift distributions biased, but even photometric redshift distributions remain incomplete and biased [77], [81], [90], [93].

The sub-millimetre wavelength regime is an exciting regime to observe since about half of the contribution to the star formation rate density is measured from sub-millimetre emissions [37] and between 60 – 70% of these emissions originate from SMGs with star formation rates $> 200 M_{\odot} \text{ yr}^{-1}$ [15]. The brightest high- z SMGs have observed sub-millimetre emissions of $S_{850\mu\text{m}} > 9 \text{ mJy}^2$ and have some of the most intense stellar nurseries with implied star formation rate of $> 1000 M_{\odot} \text{ yr}^{-1}$ [8], [74], [14], [13]. Therefore by searching for SMGs contained within protoclusters we may learn how the protoclusters themselves have formed, and whether there are any environmental triggers for SMGs from the protocluster’s high density environment.

1.2.1 Spectral Energy Distribution

Although we live in a 3D spatially distributed universe, astronomers are only able to study celestial objects as projected in a 2D plane, making it difficult to quantify important physical properties such as 3D spacial distribution, luminosity, star formation rate, size, mass, morphology, environment, and so on. Nevertheless, with knowledge of a galaxy’s rest-frame atomic emission lines we’re able to measure a galaxy’s redshift (3D projection) by measuring the redshift of spectral features, known as spectroscopic redshift (spec- z). However, high- z SMGs are inherently very dusty, making them subject to significant extinction (dimming) and therefore photometrically obscured by most modern spectrographs. As a result, spectroscopically selected galaxies are bias to optically luminous SMGs, which are only a fraction of all SMGs [10]. However, by measuring a galaxy’s spectral energy distribution (SED) we can begin to reveal some of its key distinguishing features. An SED describes a galaxy’s energy density (flux) per unit time as a function of wavelength. Therefore, by measuring apparent

²Jansky: $\text{Jy} = 10^{-26} \text{ W m}^{-2} \text{ Hz}^{-1}$

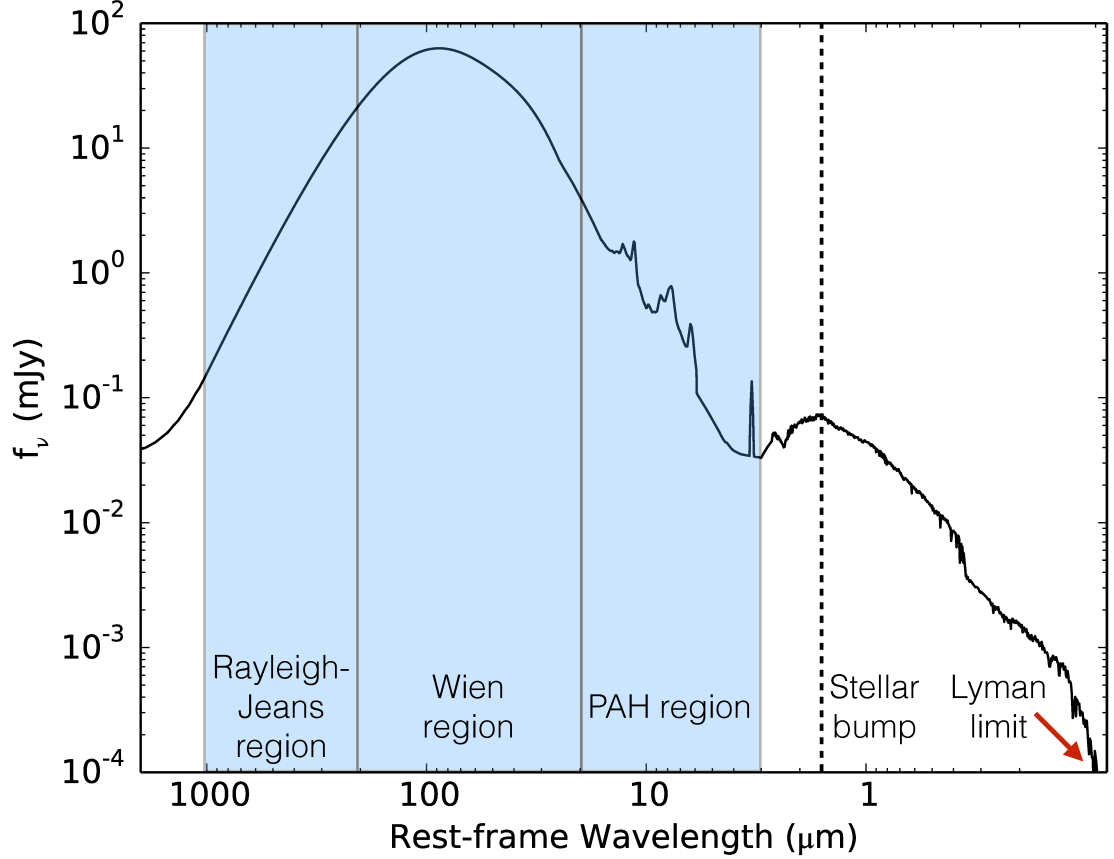


Figure 1.3: Rest-frame ($z = 0$) galactic spectral energy distribution (SED) template. Specifically, ALMA ALESS SMG composite SED [84]. Overlaid in blue are the astrophysical significant regions listed in § 1.2.1

flux values in different wavelengths we're able to construct a galactic SED, as shown in Figure 1.3

A galaxy's SED is often interrupted by molecular and atomic absorption and emission lines, but for simplicity we may characterize it as a series of black-body emission curves. Planck's law for black-body radiation characterizes flux as:

$$S_{\lambda}(T) = \frac{2hc^2}{\lambda^5} \frac{1}{\exp(hc/\lambda k_b T) - 1} \quad (1.1)$$

In the limit of short wavelength ($hc \gg \lambda k_b T$) we get the Wien limit:

$$S_{\lambda}(T) \propto \lambda^{-3} \exp(-hc/\lambda k_b T) \quad (1.2)$$

In the limit of long wavelength ($hc \ll \lambda k_b T$) we get the Rayleigh-Jeans limit:

$$S_\lambda(T) \propto T\lambda^{-2} \quad (1.3)$$

If we measure an observed radiation which has been redshifted as $\lambda'_{\text{observed}} = \lambda_{\text{observed}} + \lambda_{\text{emitted}}$, this results in a redshift of $z = (\lambda'_{\text{observed}} - \lambda_{\text{emitted}}) / \lambda_{\text{emitted}}$, which still results in a similar black-body distribution, however, the distribution is shifted by $\lambda_{\text{observed}} = (1 + z)\lambda_{\text{emitted}}$. Furthermore, since $S \propto 1/D_L^2$, where D_L is the luminosity distance³, then as the energy distribution is shifted by a factor of $(1 + z)$, its amplitude will also be diminished by a factor of $1/D_L^2$. It is also important to note that flux varies with wavelength, so the SED's magnitude will also diminish as a function of wavelength.

In reality, a galaxy's SED is composed of many different physical phenomena, and varies dramatically depending on its stellar composition, age, redshift, dust temperature, the viewing angle, and the astrophysical activity occurring within. Figure 1.3 shows a rest-frame ($z = 0$) SED template generated from observationally-based simulations [35]. For simplicity, we'll focus on a galaxy's total SED in 4 separate regions, for which 3 of them can all be approximated by individual black-body distributions.

1. Within the Rayleigh-Jeans limit, from $\sim 3\text{mm} - 400 \mu\text{m}$ (rest frame), cold dust ($\sim 30\text{K}$) emissions distinctly dominate the regime with a well-characterized modified black-body distribution. Dust SEDs are steeper than black-body spectra in the Rayleigh-Jeans regime. If the SED is represented by the function $\nu^\beta S_\nu$, then the Rayleigh-Jeans spectral index is $-2 - \beta$.
2. The mid-IR, from $\sim 400 - 20 \mu\text{m}$, is estimated by Wien's law. This regime can be estimated as a grey-body because dust SEDs do not fall exponentially like black-bodies in the Wien regime, due to the contribution from additional hot dust components in the interstellar medium [10]. Primarily composed of Si, the cold dust is contained within the interstellar medium and has peak emissions $\sim 100 \mu\text{m}$ [45], [63], [10].

³Luminosity distance: $D_L = \sqrt{\frac{L}{4\pi S}} = (1 + z)D_M$

3. Unlike the far-infrared's smooth continuum, the mid-infrared portion has emission and absorption features generated by heavy molecules and smaller dust grains. Dominating features in this region are primarily due to Polycyclic Aromatic Hydrocarbons, Å-diameter heavy molecules containing hundreds of carbon atoms which exist in cold molecular clouds and when irradiated by young stars, emit spectral line features at discrete wavelengths from $\sim 20 - 3 \mu\text{m}$ [49].
4. The underlying the black-body distribution from far-infrared emissions is overcome by the relative rise in emissions generated from old stellar populations, this is often referred to as the $1.6 \mu\text{m}$ stellar bump [69]. Old stars which evolve into cooler red giant stars and supernovae have inherently low metallicity⁴, with their metal-rich emissions represented by a modified black-body peaking at about $1.6 \mu\text{m}$ [10]. This feature however is not present in a galaxy's SED. If present, the emissions from active galactic nuclei (AGN) may dominate in this regime. Powered by mass accretion onto massive black holes, the emissions generated by friction between the falling dust grains may over-power all characteristic absorption and emission features present from old stellar populations [62], [45], [14], [35]. Similarly, the $1.6 \mu\text{m}$ bump is easily overpowered by extremely young ($\sim 1 \text{ Myr}$) stellar populations, where it is swamped by the essentially power-law spectra of very hot, massive young stars [69].
5. Regardless of stellar population, young and old stars have emission from $2.0 - 0.09 \mu\text{m}$, where $\lambda \approx 900 \text{ \AA}$ is known as the Lyman limit. The Lyman limit (or Ly- α transition) is the short-wavelength end of the Hydrogen-Lyman series, and corresponds to the ionization energy of hydrogen, $E_1 = -13.6\text{eV}$ (ultraviolet part of the spectrum). This ionization energy is the minimum energy required for an electron in the hydrogen ground state to escape from hydrogen's electric potential, thus creating a hydrogen ion in the process:



⁴Metallicity: $[\text{Fe}/\text{H}] = \log_{10} \left(\frac{N_{\text{Fe}\star}}{N_{\text{H}\star}} \frac{N_{\text{H}\odot}}{N_{\text{Fe}\odot}} \right)$

Therefore, any radiation $\lambda \gtrsim 0.09 \mu\text{m}$ is absorbed by neutral hydrogen which generates ionized hydrogen and is observed as an extreme “break” in the SED for all $\lambda \lesssim 0.09 \mu\text{m}$. A common source of this radiation comes from the Ly- α transition, which occurs when an electron decays from the $n = 2$ to the $n = 1$ state, happening around $\lambda \approx 0.12\mu\text{m}$. When a Ly- α transition occurs a photon is released, which is then absorbed by neutral hydrogen.

1.2.2 Negative K-Correction

The expansion of the Universe tells astronomers how quickly galaxies are recessing from our rest frame at redshift $z = 0$. These recession velocities can be translated into distances, and since light travels at $v = c$, it provides us with the lookback time (see Figure [1.2](#)). The lookback time to a celestial source is the difference between the age of the Universe now ($z = 0$) and the age of the Universe at the specific epoch ($z = z'$). The expansion of the Universe also provides us with the challenge that sources at different distances, and thus redshifts, have different apparent brightnesses. To measure a sources true rest-frame brightness you must evoke a photometric measurement known as the K-correction ([38](#); [59](#)).

The K-correction is defined as:

$$M = m - \mu - K \tag{1.5}$$

where M is the absolute magnitude of the source, m is the apparent magnitude of the source, $\mu = 5(\log_{10} d - 1)$ is it’s distance modulus, K is the K-correction, and d is it’s distance. Magnitude is a measure of a celestial object’s brightness. So, M is how bright the source inherently is, m is how bright the source appears to be when observed on Earth, μ is the measure between the apparent magnitude and the absolute magnitude ($\mu = m - M$), and therefore accounts for the dimming occurring due to the inverse-square law. The K-correction is only used for measuring light through a filter, thus it would not be required if one were to measure an object’s emission over all wavelengths (bolometric flux). Therefore, the K-correction is an adjustment to

the standard measure of brightness for a celestial object required to correct for the redshift.

The K-correction is one of the most useful properties for detecting SMGs. Since flux $\propto L/D_L^2$ (inverse-square law), one would expect that as the galaxy increases in distance, D_L , the observed flux would appear dimmer. However, this is not what is observed for SMGs at 850 μm . Shown by an SMG's SED in Figure [1.4](#), as the SMG becomes redshifted, the flux of the SED we measure at 850 μm remains constant from $1 \lesssim z \lesssim 10$, due to the negative K-correction. The SED of an SMG has a positive slope at sub-millimetre wavelengths because of the modified black-body emission produced by the massive amount of dust (see § [1.2.1](#)). In the rest-frame, this emission peaks at $\sim 100 \mu\text{m}$, meaning that the flux density between 850 μm and 2 mm is located in the Rayleigh-Jeans regime and increases with increasing redshift, hence the negative K-correction. The negative K-correction is so significant that it negates cosmological dimming, where an object's surface brightness decreases as luminosity distance increases, in accordance with:

$$I_{\text{observed}} = \frac{I_{\text{emitted}}}{(1+z)^4}, \quad \text{[85]} \quad (1.6)$$

where I is the surface brightness of the galaxy. Therefore, providing an extremely useful tool for investigating the early Universe.

The negative K-correction makes SMGs unique in the Universe because we can observe galaxies at high redshift as easily as we can observe galaxies in the relatively local Universe. This property alone provides some insight into the evolution of cosmic star formation rate density. If the occurrence of SMGs (and subsequently, the cosmic star formation rate) is independent of redshift, we should expect to see equal numbers of SMGs in the local Universe and at higher redshifts. However, the SMG's local counterpart, ultra-luminous infrared galaxies, are extremely rare in the Universe, whereas SMGs are comparatively more common at high redshift [\[10\]](#), which reinforces the already well established idea that the cosmic star formation rate density changes with redshift [\[37\]](#).

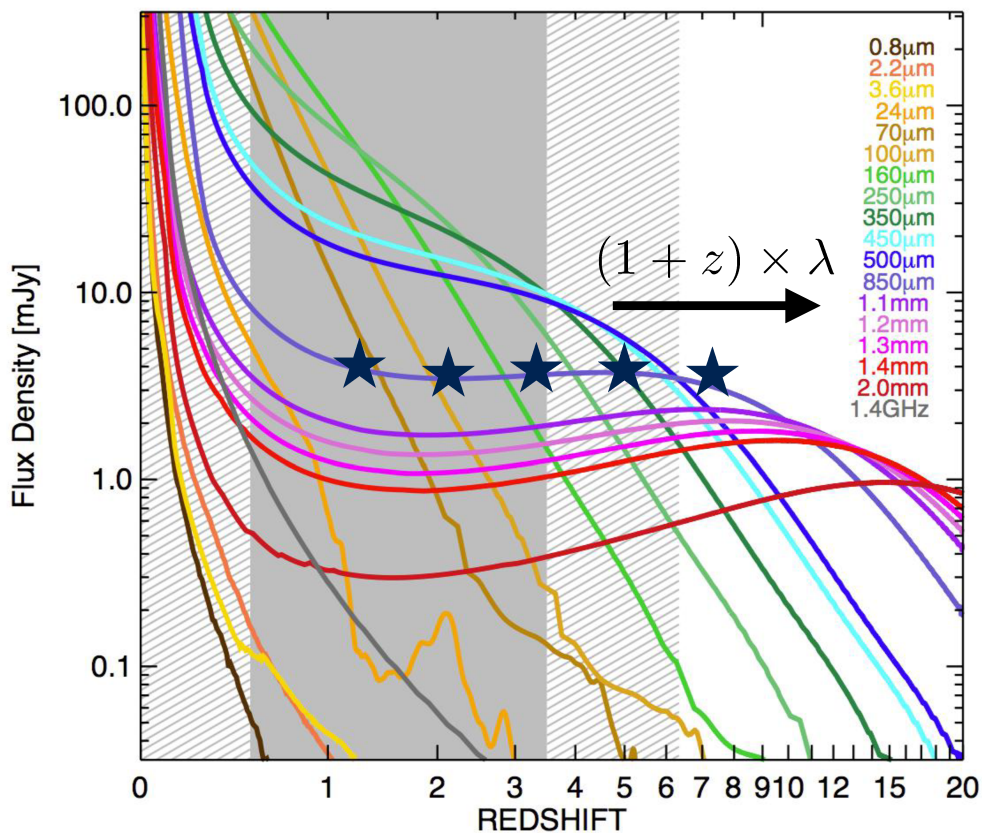
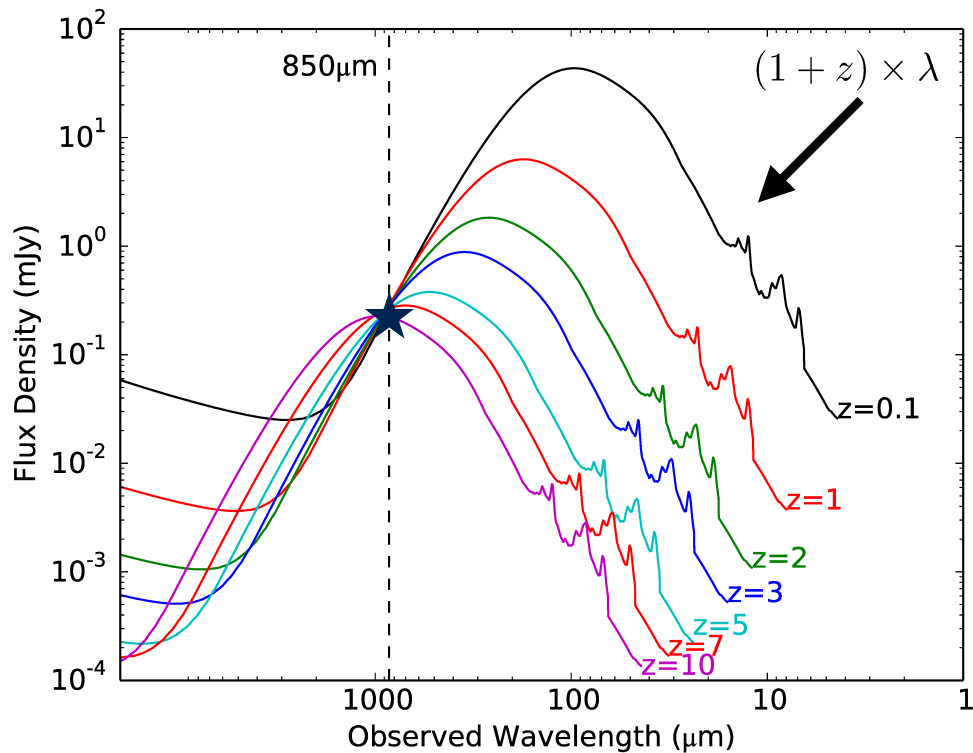


Figure 1.4: **Top:** Multiple template SEDs with increasing redshift. **Bottom:** Template spectrums of an SMG at different redshifts, with data courtesy of [8] the the figure courtesy of [10] with data from [8]. The black stars represent the emission at 850 μm .

1.3 Protostars

The formation of a star begins by the collapse of a molecular cloud [58]. The molecular cloud is an accumulation of dust and gas, primarily composed of molecular hydrogen, H_2 , and is at a very low temperature, usually between 10 to 30 K. As stars need to collapse from molecular hydrogen, hot molecular clouds are not ideal stellar nurseries, as they contain ionized hydrogen. This is not to be confused with the ionization of molecular hydrogen, which happens as a star forms and releases ultraviolet radiation, which then ionizes the molecular hydrogen. As the molecular cloud self gravitates it creates small molecular dense cores, each in balance with gravity (inward force), gas pressure (outward force), and magnetic pressure (outward force). As the dense core accretes mass from the surrounding molecular cloud, the gravitational collapse overwhelms both the gas and magnetic forces and the mass collapse is initiated. Models and simulations of molecular collapse of a protostar supported solely by gravity and gas pressure suggests that the collapse begins from the core and works it's way out [72], however spectroscopic surveys have yet to observe this predicted phenomenon [32]. The gas that collapses towards the centre of the dense core builds up a low-mass protostar. As the gas continues to collapse and combine into the core, the surrounding gas begins to impacts the disc instead of the star it self. Despite theoretical models, the exact process of which the material within the disc combines as it spirals inward onto the protostar is not fully understood [72].

The surrounding gas and dust makes the protostar nearly invisible to optical wavelengths. Typically, a protostar radiates between 2000 to 3000 K [88]. The gas that collapses onto the protostars heats up due to the collisions of the particles, which results in heat energy which is then reradiated into the surrounding molecular cloud. The surrounding material heats up and radiates between the near-infrared to microwave [88]. Infrared telescopes such as the *Spitzer Space Telescope*, *Wide-field Infrared Survey Explorer* (*WISE*), and the *Herschel-SPIRE* telescope and sub-millimetre telescopes such as the *JCMT*, *Atacama Large Millimeter/Sub-Millimeter Array* (*ALMA*)

and Sub-Millimeter Array (SMA) are able to detect protostars. Unfortunately, high-resolution images of protostars are difficult to obtain for two main reasons. 1) The protostar’s light is being absorbed by the entire surrounding cloud, and thus smearing the image of the protostar within. 2) Angular resolution goes as $\theta \propto \lambda/D$ where λ is the observed wavelength and D is the diameter of the telescope. Therefore, observing a small and distant celestial object in infrared and sub-millimetre wavelengths will result in a diffraction limited image, making it difficult or impossible to resolve a single protostar.

1.3.1 The Low Luminosity Problem

The “Standard Model” of star formation results from the predictions of the gravitational collapse that forms low-mass stars. This model suggests a singular isothermal sphere, initially at rest, which then proceeds to collapse in an inside-out fashion, starting at the core and moving outward at the speed of sound [72]. This gives rise to a *constant* mass accretion rate of $\sim 2 \times 10^{-6} M_{\odot} \text{ yr}^{-1}$. However, accretion luminosities for embedded protostars are observed to be a factor of 10 to 100 times higher than the predicted accretion rate, giving rise to the “Low Luminosity Problem” [46]. The problem has been further explored from studies using the *Spitzer Space Telescope* by looking at molecular cores to planet forming disks [26]. This program has made the first discoveries of a new class of star called Very Low Luminosity Objects (VeLLOs), which are stellar objects embedded within dense molecular cores with $L_{int} \leq 0.1 L_{\odot}$, which were previously undetected and classified as starless regions [22]. Since discovering VeLLOs, a low-luminosity class of protostars, the “Low Luminosity Problem” has been exasperated. From this survey, it has also been shown that protostellar luminosities are greatly scattered (see Figure 1.5), and are skewed largely towards low luminosities, namely $> 50\%$ of protostars have luminosities suggesting accretion rates less than $10^{-6} M_{\odot} \text{ yr}^{-1}$ [26], [31], [30].

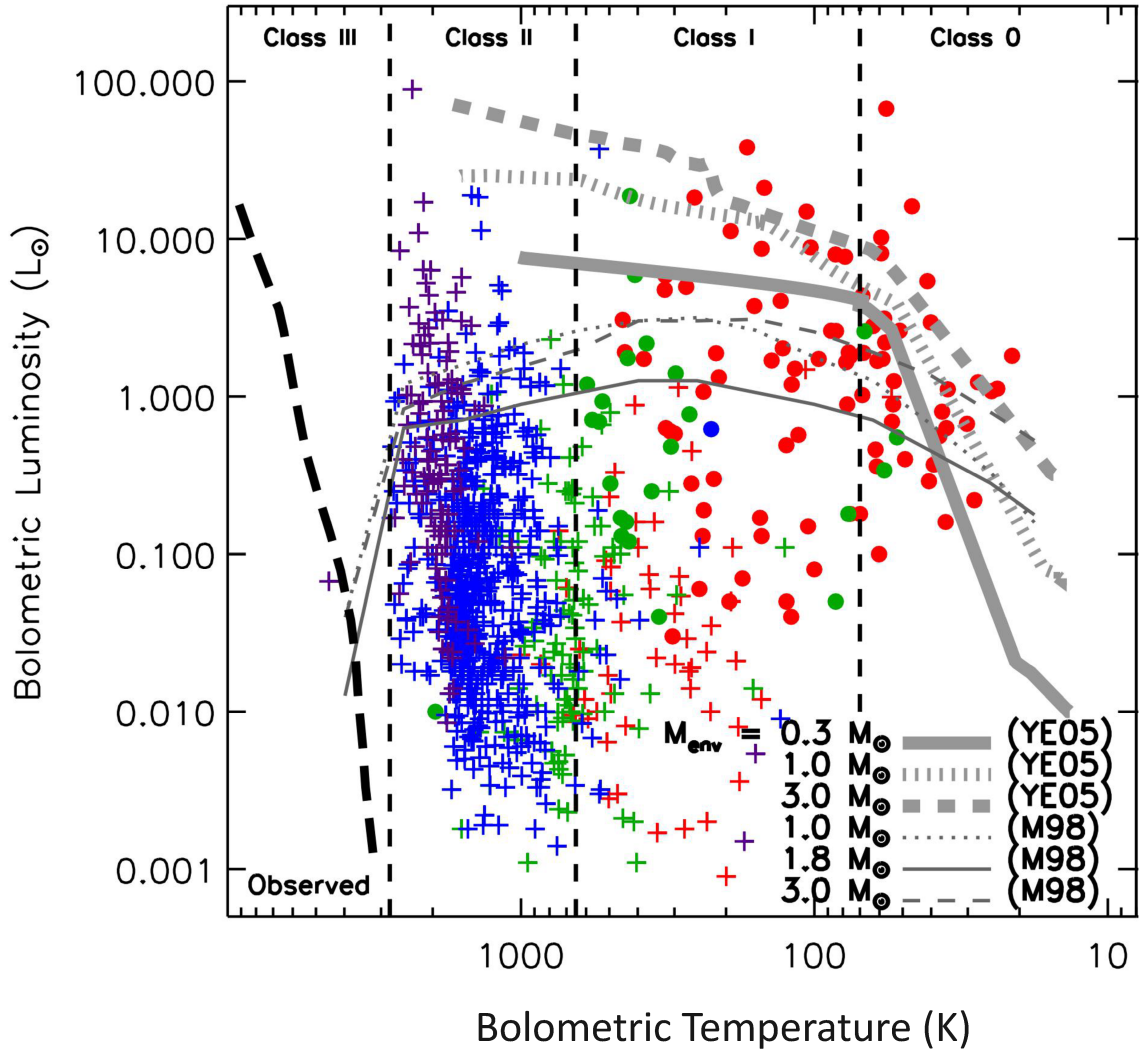


Figure 1.5: Courtesy of [31]. Bolometric luminosity temperature plot for protostars. Class I in red, Flat in green, Class II in blue, and Class III in purple. The filled circles represent protostars detected in the sub-millimetre, and plus signs indicate protostars undetected in sub-millimetre. The grey lines tracks represent stellar evolution tracks with different initial core masses. The thick grey line represents the zero age main sequence track from 0.1 to 2 M_{\odot} .

1.3.2 Variability

It has been suggested that a possible solution to the “Low Luminosity Problem” is that mass accretion does not occur at a constant rate, but either accretion rates decline with time, or accretion rates occur in episodic events, where accretion rates are very low most of the time, but occasionally very high [46]. Therefore, episodic accretion would feature prolonged periods of little accretion, followed by short outbursts of high amounts of accretion. This variability of the accretion, and therefore luminosity, would possibly account for the very large spread in observed luminosities and the statistically significant source of protostars at low luminosities [26], [31], [30]. Hydrodynamical simulations predict accretion rates that both decline with time and also feature short-term variability events and episodic outbursts [25], [27]. Their simulations are able to filter out accretion variability and outbursts, which do not provide good fits to observed luminosity data, suggesting that outbursts are in fact required.

1.3.3 JCMT Transient Survey

The Transient Survey is a two year long program using SCUBA-2 on JCMT in search of the solution to the “Low Luminosity Problem”. The solution to this problem may lie in episodic mass accretion – prolonged periods of very low accretion punctuated by short bursts of rapid accretion. However, the timescale and amplitude for variability at the protostellar phase is almost entirely unconstrained. Transient looks at deeply embedded protostars in several nearby star-forming regions to measure accretion variability of protostars, in attempt to understand the physics of disk instabilities that drive this variability (Mairs et al. in preparation). The selected fields include enough bright sources to allow for relative flux calibration to an accuracy of $\sim 3\%$ RMS. This is the first large dedicated sub-millimetre monitoring program to assess accretion variability in protostars, and is opening up a new field of study.

Episodic mass accretion is generally considered a two state process with a common, low-accretion, low-luminosity phase and a rare, high-accretion, high-luminosity phase.

In reality, both the amplitude of the non-steady accretion and the timescale over which the accretion varies are likely to span a wide range of values. Monitoring of the brightness of deeply embedded protostars with careful and precise calibration will allow for direct measurements of both the range of accretion events and their duration. The power spectrum of accretion variability on young objects would provide a diagnostic for the size and location of disk instabilities, independent of whether the majority of the mass is accreted in rare large events. A simple power-law argument demonstrates the feasibility of the search. If the accretion rate increases by two orders of magnitude once in a million years, the minimum threshold to resolve the “Low Luminosity Problem”, then one expects a 10% variation for any given source within a year (a 3σ detection at the anticipated flux calibration accuracy) for a cumulative power-law index of -2 . The large sample makes this experiment robust to shallower power laws. On the other hand, a non-detection of variability on this sample would indicate that the accretion flow moves smoothly through the inner disk, placing a stringent requirement on the instability physics in the inner disk at young ages.

1.4 Instrumentation & Data Reduction

The majority of the data presented in my thesis has been taken from the sub-millimetre camera, SCUBA-2, mounted on the James Clerk Maxwell Telescope. I had the opportunity to spend six months in Hawai’i at the JCMT where I conducted over 250 hours of observations for a variety of sub-millimetre astronomy projects, including my own research.

1.4.1 JCMT

The James Clerk Maxwell Telescope (JCMT), run by the East Asian Observatory, is the largest single-dish telescope optimized for sub-millimetre astronomy, residing at 4092 metres (13,425 feet) above sea level near the summit of Mauna Kea, Hawai’i. The JCMT has a 15-metre parabolic primary dish composed of 276 individual adjustable panels with surface accuracy finer than $50\ \mu\text{m}$. The telescope is entirely covered in a

single sheet of Gore-Tex, the largest piece of Gore-Tex in the world. The Gore-Tex material is opaque to short wavelengths, such as optical radiation, however is almost invisible to sub-millimetre radiation. The Gore-Tex acts as a shield to the telescope, protecting it from strong winds, sand, birds, and precipitation. The exterior of JCMT and it's primary dish are shown in Figure [1.6](#).

Mauna Kea is objectively one of the best sites for astronomy in the northern hemisphere due to its favourable observing conditions. The summit of the dormant volcano is 4,207 metres (13,802 feet) above sea level and is above the inversion layer, keeping most of the cloud cover bellow the summit, ensuring arid conditions, free of atmospheric pollution. As a result, the summit is exceptionally stable. Dry and stable conditions are important for sub-millimetre astronomy as image distortion occurs in moist unstable air caused by turbulent mixing in the atmosphere, causing variations in the optical refractive index.

Atmospheric transmisson in sub-millimetre wavelengths is mainly effected and defined by atmospheric opacity due to water vapour. The precipitable water vapour (PWV), measured in millimetres and the opacity (τ) measured at 225 GHz are measured and different weather grades are objectively measured by these values as: Band 1: $\tau < 0.05$ and $PWV < 0.83$ mm; Band 2: $0.05 < \tau < 0.08$ and $0.83 \text{ mm} < PWV < 1.58$ mm; Band 3: $0.08 < \tau < 0.12$ and $1.58 \text{ mm} < PWV < 2.58$ mm; Band 4: $0.12 < \tau < 0.2$ and $2.58 \text{ mm} < PWV < 4.58$ mm; and Band 5: $\tau > 0.2$ and $PWV > 4.58$ mm. The atmospheric transmission measured on Mauna Kea is represented in Figure [1.7](#). The transmission at $450 \mu\text{m}$ and $850 \mu\text{m}$ has been empirically derived as a function of the opacity by the East Asian Observatory⁵:

$$\begin{aligned} T_{450} &= \exp(-AM \times 26 (\tau - 0.01196)) \\ T_{850} &= \exp(-AM \times 4.6 (\tau - 0.00435)) \end{aligned} \tag{1.7}$$

⁵www.eaobservatory.org/jcmt/instrumentation/continuum/scuba-2/time-and-sensitivity/

where AM is the air mass near transit, also empirically derived as:

$$AM = \left(0.9 \cos \left[\frac{\pi}{180} (\delta - 19.823) \right] \right)^{-1} \quad (1.8)$$

where δ is the elevation, or declination of the source being observed.

1.4.2 SCUBA-2

The Sub-millimetre Common-User Bolometer Array 2, or SCUBA-2, is a 10,000 pixel bolometer camera mounted on the JCMT operating at sub-millimetre wavelengths [36]. Commissioned in 2011, SCUBA-2 has proven to be a revolutionary sub-millimetre camera capable of reaching unprecedented depths. SCUBA-2 is mounted with two imaging arrays working simultaneously at 450 μm and 850 μm , each with 5120 superconducting transition edge sensors recoding data at a rate of 200 Hz. Each array of bolometers is split up into four subarrays, each with 1280 bolometers. The SCUBA-2 450 μm and 850 μm bandpasses are overlaid on top of the atmospheric transmission at Mauna Kea in Figure 1.7.

The angular resolution, or beam size, of a telescope is defined as the full width half maximum of the collimated light entering the telescope’s camera, which defines the resolution of the image. The beam size of SCUBA-2’s two wavebands, 450 μm and 850 μm are 9.8'' and 14.6'' [20], respectively.

The confusion limit is a noise factor related to the astronomical background, which represents the limit at which the noise of the map will not be reduced any further. While dependent on the location of a source, the confusion limit of SCUBA-2 is approximately:

$$\begin{aligned} \sigma_{850} &= 0.7 \text{ [mJy beam}^{-1}\text{]} \\ \sigma_{450} &= 0.5 \text{ [mJy beam}^{-1}\text{]} \end{aligned} \quad [16] \quad (1.9)$$

SCUBA-2 has two main scanning patterns: CV Daisy and PONG. Observing

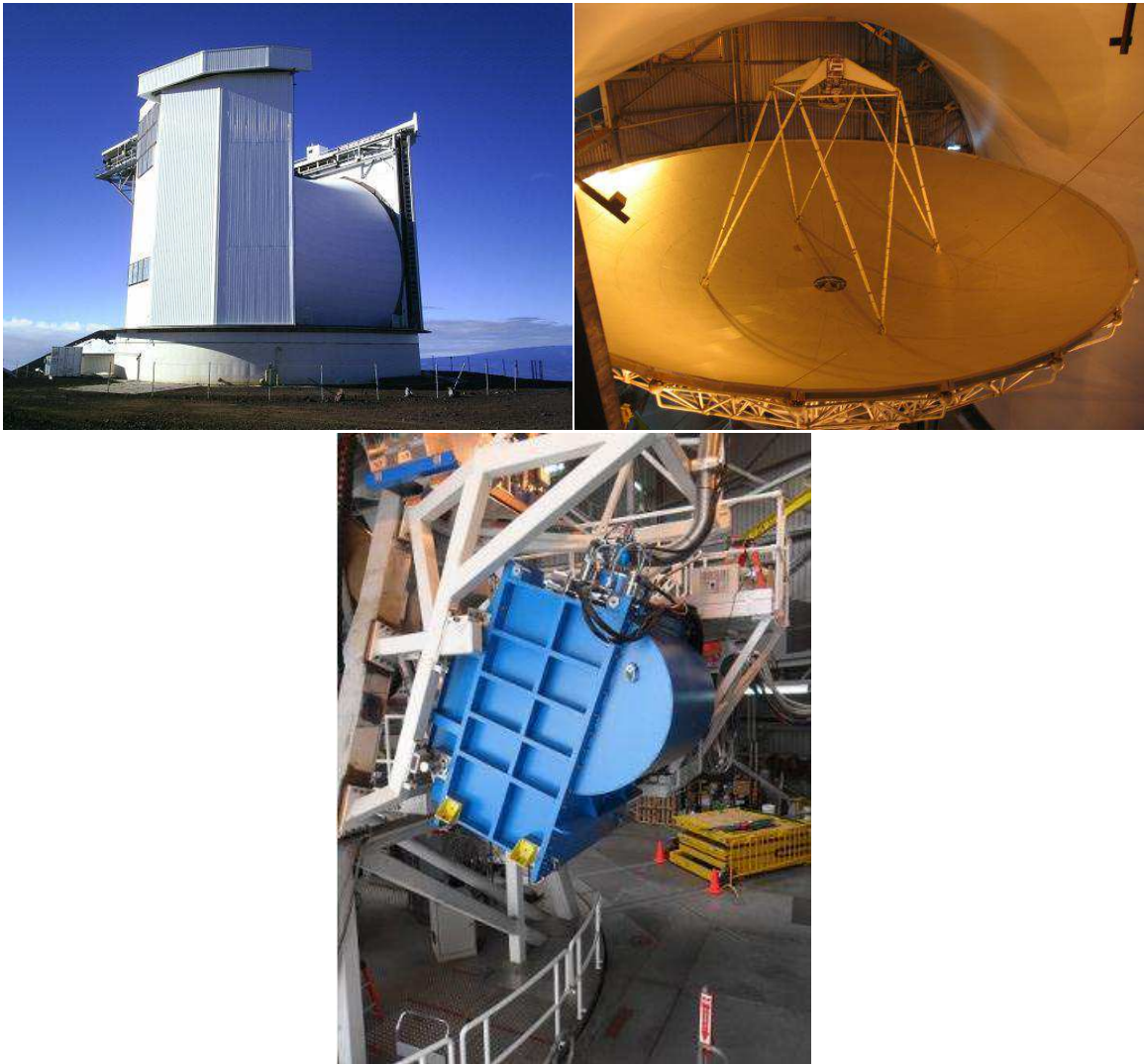


Figure 1.6: **Left:** The James Clerk Maxwell Telescope (JCMT). **Right:** JCMT's 15m primary dish. **Bottom:** SCUBA-2 mounted on the side of JCMT. All images have been sourced from: <http://www.eaobservatory.org/jcmt/public/jcmt/>.

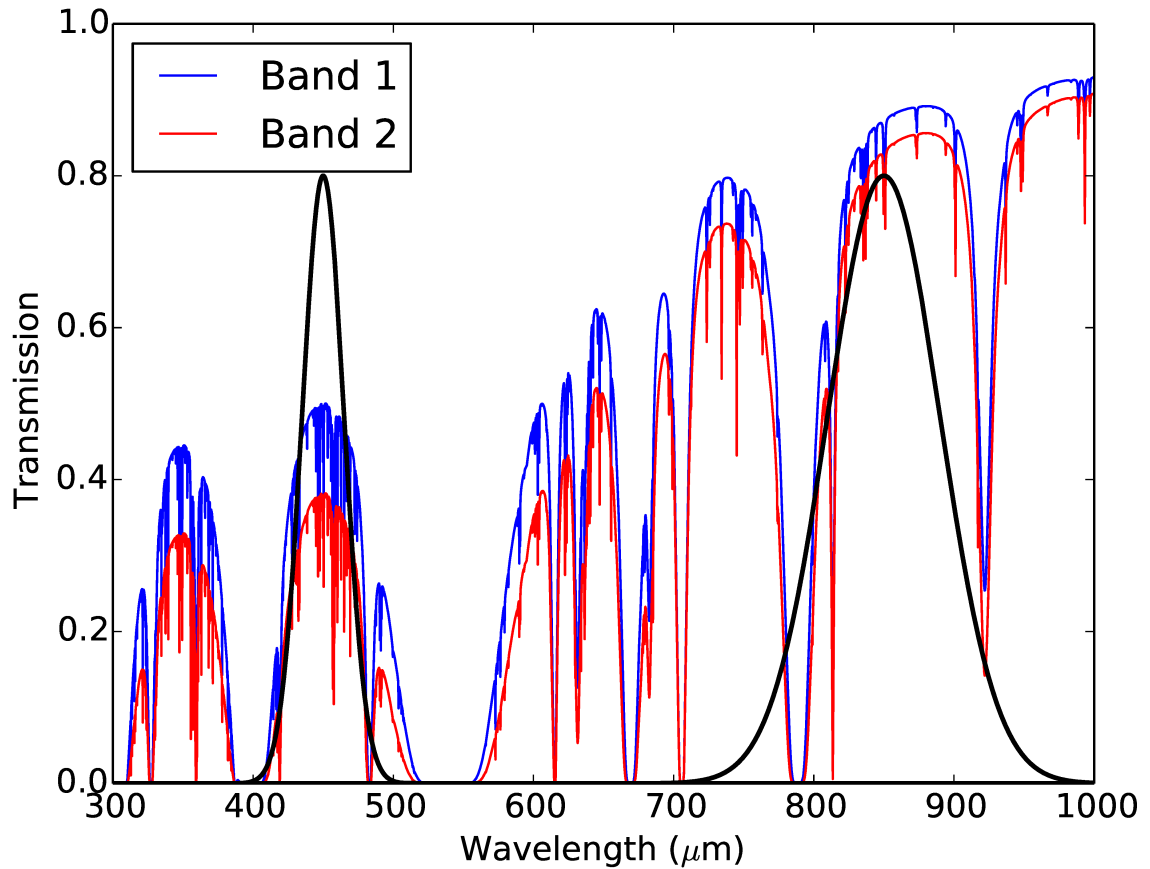


Figure 1.7: Atmospheric transmission on Mauna Kea for both Band 1 (blue curve) and Band 2 (red curve) weather. The black curves represent the 450 μm and 850 μm bandpasses for SCUBA-2. The atmospheric transmission data are provided courtesy of the Caltech Sub-millimetre Observatory from: <http://www.submm.caltech.edu/cso/weather/atplot.shtml>.

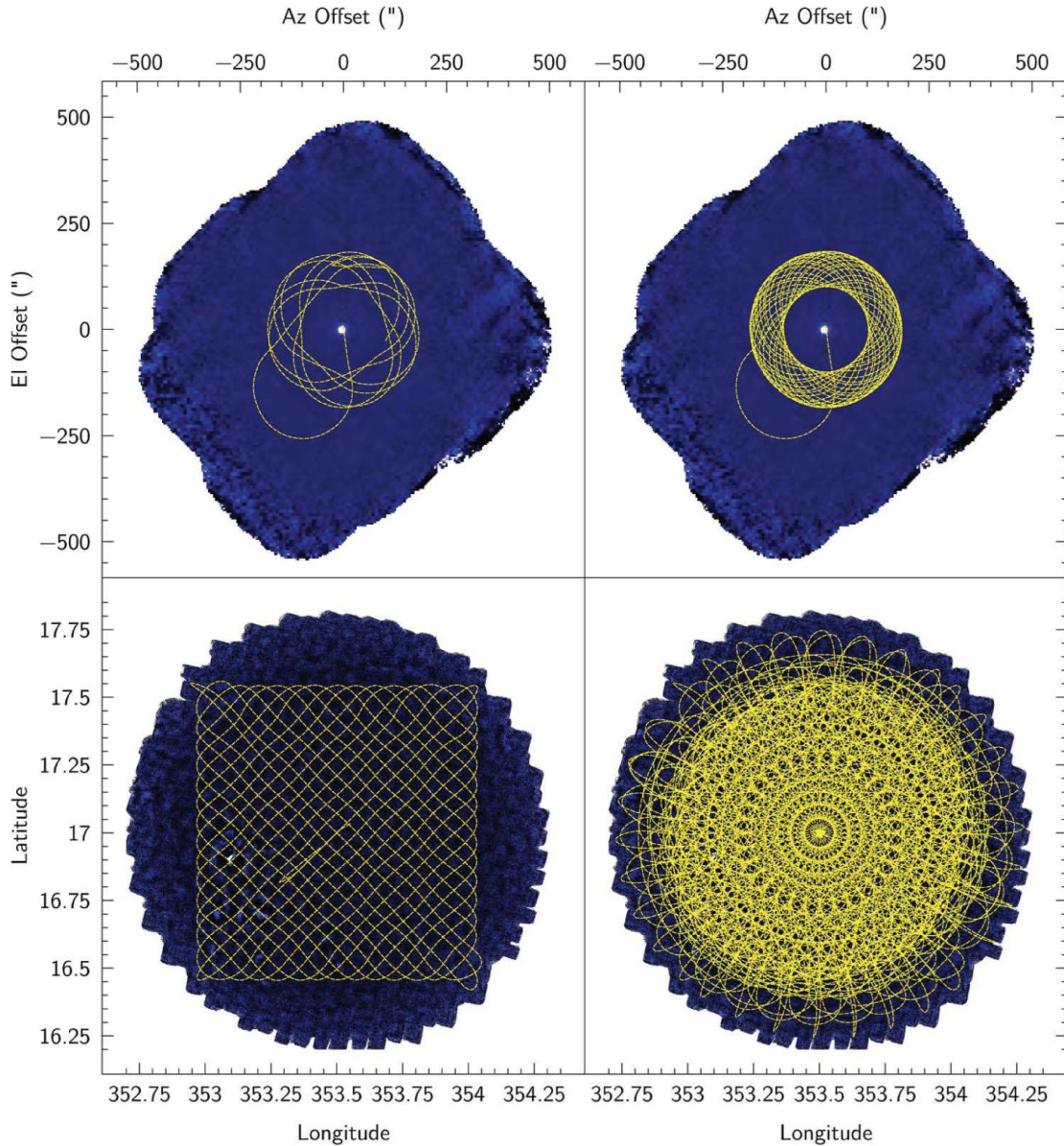


Figure 1.8: This figure is provided courtesy of [36]. The JCMT telescope track in offsets of azimuth (horizontal) and elevation (vertical) for the two SCUBA-2 scanning patterns. **Top left:** A single rotation of the daisy pattern; **Top right:** Multiple rotations of the daisy pattern for a typical map based on a 3-arcmin diameter core; **Bottom left:** A single pong pattern; **Bottom right:** Multiple rotations of the pong pattern for a typical map based on a 30-arcmin diameter map. The blue background represents the total covered area of sky during an observing pattern.

modes are chosen based on the size of the region being observed and the size scales of the structure you would like to contain. Examples of each observing mode are shown in Figure 1.8. The CV Daisy pattern is where the telescope moves in a Daisy-like pattern across the sky at constant velocity (CV). It is designed for either small, compact sources, or deep core maps, as the pattern yields a very deep 3-arcmin centre region in it’s map. The PONG pattern is designed for larger maps. The telescope scans across the sky in a grid-like pattern, yielding a lower sensitivity map, where the sensitivity is more evenly spread throughout the entire map.

1.4.3 SCUBA-2 Data Reduction

SCUBA-2 data reduction is preformed using an iterative map-making process, *makemap* in the Sub-Millimetre User Reduction Facility (SMURF) ([11]; [41]). The map-making process is split up into two sections, pre-processing and then iterative steps.

In pre-process, raw time series data is read in from each of the four subarrays. Exposure corrections, known as flat-fields, are applied, determined by the closed-shutter internment response measurements taken immediately prior to the observations. The data is then down-sampled to match the appropriate pixel size (e.g. number of arc-seconds per pixel), then the data are “cleaned”, by removing noise spikes in the data likely caused by cosmic ray events. Any gaps are filled in by interpolating between the gap, along with a Gaussian noise added.

The iterative process then begins by modelling the total on-sky integration time: astrophysical signal (AST), common-mode (or atmospheric) signal (COM), low-frequency noise (FLT), and other noise (NOI). The purpose of these iterative steps is to minimize the residuals in the Cleaned Value, where the Cleaned Value is the sum of each AST, COM, FLT, NOI, and some residuals consisting of both uncorrelated white noise, which cannot be minimized, and components correlated to the COM, AST, or FLT models. Once the maps are individually co-added in an optimal stack using the variance of the data contributing to each pixel to the weighted specially aligned pixels, then a final map is produced.

Chapter 2

A SCUBA-2 Survey for Luminous Far-Infrared Galaxies in Protoclusters at $z > 2$

2.1 Introduction

Current observations and simulations suggest that there has been a strong evolution in the molecular gas fractions in star-forming disk galaxies at $z = 1 - 2$ compared to similar objects at $z < 0.5$ ([34]; [48]; [2]; [13]). However, the gas supplies, star formation efficiencies, and starburst modes (merger driven versus quiescent disk) may vary strongly as a function of their local density. Galaxy evolution should be accelerated in regions of strong over-density. Recent work with *Spitzer* and *Herschel* has demonstrated enhanced star formation rate (SFR), and reversal of the star formation(SF)-environmental density relation, at $z > 1.5$ in galaxy clusters ([28, 29]; [86]). Exceptionally high level of star formation have been found in cluster cores, reaching $> 2000 M_{\odot} \text{ yr}^{-1} \text{ Mpc}^{-3}$. The reversal of the $z < 1$ trend in SF vs environmental density implies that at $z \sim 2$ massive cluster galaxies are still forming a substantial fraction of their stars in protoclusters. These high- z protoclusters are where the morphology-density relation may be established.

The target protoclusters HS1549 ([80]) and HS1700 ([78]) were chosen from the 5 survey fields of the Keck Baryonic Structure Survey (KBSS – e.g., [67]), and represents the strongest over-densities found in the survey. In HS1549 the over-density by number of galaxies is roughly a factor of 13 in a volume of $\sim 5000 \text{ Mpc}^3$, and has almost $10\times$ the surface density of Ly α emitters compared to the average among ~ 20 fields covered to a similar depth, representing the richest field of Ly α -selected objects ever observed, at any redshift.

In § 2.3 I present our sub-millimetre detections, along with their IR counterparts

and determine their cluster membership. In § 2.4 I discuss some possible implications of our results. Throughout this chapter, we use the Vega magnitude system, and assume a flat concordance cosmology with $(\Omega_m, \Omega_\Lambda, H_0) = (0.3, 0.7, 70 \text{ km s}^{-1} \text{ Mpc}^{-1})$.

2.2 Observations and Data Reduction

This work is primarily based on sub-millimetre imaging using the Sub-Millimetre Common-User Bolometer Array 2 (SCUBA-2, § 1.4.2, [36]) mounted on the James Clerk Maxwell Telescope (JCMT, § 1.4.1). Additionally, we accompany our data with complimentary archival multi-wavelength imagery and photometry within our fields from various archives (e.g. *Spitzer*-IRAC, *Spitzer*-MIPS, *Hubble Space Telescope* (*HST*)).

2.2.1 SCUBA-2 Observations

Observations were conducted in Band 1 weather conditions ($\tau_{225\text{GHz}} < 0.05$) over four nights between 26th May, 2012 and 20th April, 2013, totalling 9.8 hours of on-sky integration time (HS1549), and over five nights between 10th April, 2013 and 18th September, 2013, totalling 19.7 hours of on-sky integration (HS1700). The mapping centre of the SCUBA-2 H1549+19 field was $(\alpha, \delta) = (15^{\text{h}}51^{\text{m}}53^{\text{s}}, +19^{\circ}11'04'')$, and the mapping centre for HS1700+64 field was $(\alpha, \delta) = (17^{\text{h}}01^{\text{m}}00.6^{\text{s}}, +64^{\circ}12'09'')$. A standard 3' diameter DAISY mapping pattern was used, which keeps the pointing centre on one of the four SCUBA-2 sub-arrays at all times during exposure.

Individual 30 min scans are reduced using the dynamic iterative map-maker of the SMURF package (§ 1.4.3, [41]; [11]). Maps from independent scans are co-added in an optimal stack using the variance of the data contributing to each pixel to weight spatially aligned pixels. Finally, since we are interested in (generally faint) extragalactic point sources, we apply a beam matched filter to improve point source detectability, resulting in a map that is convolved with an estimate of the 450 μm beam. The average exposure time over the nominal 3' daisy mapping region (in practice there is usable data beyond this) is approximately 9 ksec per $2'' \times 2''$ pixel

for HS1549 and 18 ksec per $2'' \times 2''$ pixel for HS1700. Boosting fluxes by 10% to compensate for the matched filter suppressing the fluxes ([33]).

The sky opacity at JCMT has been obtained by fitting extinction models to hundreds of standard calibrators observed since the commissioning of SCUBA-2 ([21]). These maps have been converted from pW to Jy using the standard flux conversion factors (FCFs) of $\text{FCF}_{450} = 491 \text{ Jy beam}^{-1} \text{ pW}^{-1}$ and $\text{FCF}_{850} = 547 \text{ Jy beam}^{-1} \text{ pW}^{-1}$ ([20]).

The variance map was derived from the pixel integration (e.g., [47]). The RMS within the central 3-arcmin diameter regions are $0.6 \text{ mJy beam}^{-1}$ and $4.6 \text{ mJy beam}^{-1}$ (HS1549) and $0.45 \text{ mJy beam}^{-1}$ and $4.3 \text{ mJy beam}^{-1}$ (HS1700) at $850 \mu\text{m}$ and $450 \mu\text{m}$, respectively. Our depths reached at both $850 \mu\text{m}$ and $450 \mu\text{m}$ and smaller beam sizes allow us to probe sources at these redshifts more effectively than the confusion limited *Herschel* maps (e.g., [44])

2.2.2 SMA Observations

The SMA was used to resolve an elongated sub-millimetre source detected by JCMT at the centre of the HS1549 field. The details of these observations are found in Chapman et al. in preparation, but we will briefly discuss their observations here. A mosaic of three SMA pointings were obtained on August 15 and September 7, 2013 in the compact configuration (synthesized beam size $\sim 2''$ with natural weighting) in good weather ($\tau_{225\text{GHz}} \sim 0.08$) with a total on-source integration time of approximately 18 hr through the three tracks, yielding a final RMS of $0.7 \text{ mJy beam}^{-1}$ in the central regions. The data were calibrated using the MIR software package ([70]), modified for the SMA.

2.2.3 Gemini GNIRS

Near-infrared spectra of several SMG IDs were obtained using the cross-dispersed mode of the Gemini Near-Infrared Spectrograph (GNIRS) on the Gemini North 8.1 m telescope. This configuration provides a continuous spectral coverage from

$\sim 8400\text{\AA}$ to $2.48\ \mu\text{m}$ at a spectral resolution of ~ 1500 with a spatial scale of $0.15''$ per pixel. The $1.0'' \times 7''$ slit centred on the peak of the $2.2\ \mu\text{m}$ emission. The seeing during the galaxy observation was $0.8''$ as measured from the telluric A1V standard HIP 58616, observed right before the galaxy at a similar airmass. The strongest emission features we expect to observe are [OII] 3727, [OIII] 5007, [NII] 6548, [NII] 6583, and $\text{H}\alpha$.

The observations used an object-sky-sky-object pattern, with the sky position $50''$ away from the galaxy nucleus, free of extended emission or background stars. Eight individual on-source integrations of 240 seconds each were carried out.

The spectral reduction, extraction, and wavelength and flux calibration procedures were performed using version 1.9 of the “XDG NIRS” code detailed in [53]. Briefly, the processing consists of removing cosmic ray-like features, dividing by a flat field, subtracting sky emission, and rectifying the tilted, curved spectra. Wavelength calibration is achieved using argon arc spectra, and then a spectrum of each order is extracted, divided by a standard star to cancel telluric absorption lines, and roughly flux-calibrated using the telluric standard star spectrum. The pipeline merges the different spectral orders for each extraction window into a single 1D spectrum from $0.84\ \mu\text{m}$ to $2.48\ \mu\text{m}$. In all cases the agreement in flux between the overlapping regions of two consecutive orders was very good, and scaling factors of $< 3\%$ were necessary.

2.2.4 Auxiliary Data

We also draw on previous imaging taken in this field. Ground based optical images of these fields were obtained using from the *William Herschel 4.2m Telescope* (WHT) on *La Palma* and the *Prime Focus Imager* (see [67]), near-IR imaging from *Palomar 5.1m Hale Telescope* and the *Wide Field Infrared Camera* (see [71]), *Infrared Array Camera* (IRAC), and the *Spitzer Space Telescope* (see e.g., [5]). The IRAC observations were designed to overlap as much as possible with the ground-based K_s and optical images, however the IRAC images in the four IRAC bands completely overlap over only a relatively small fraction of the field observed in the K_s band, with the smallest

overlap in the IRAC channel 1 ($3.6\mu\text{m}$) and channel 3 ($5.8\mu\text{m}$) images, but much larger overlap in channels 2 ($4.5\mu\text{m}$) and 4 ($8.0\mu\text{m}$). The photometric calibrations for the IRAC images were as determined by the IRAC team ([5]). *HST* datasets in F160W with the WFC3, and F814W with the ACS are described previously in [78, 80].

2.3 Results

2.3.1 Sub-Millimetre Source Detection

We have generated sub-millimetre source catalogues from our $850\mu\text{m}$ SCUBA-2 maps. We adopted a cutoff of signal-to-noise ratio (SNR) > 4 by combining the data and variance maps produced from ORACDR’s pipeline process via the STARLINK package. We removed all spurious sources that were false detections in high noise regions near the field edge, where the on-sky exposure time reduced to 10% that of the centre of the map. The regions we selected sources from typically had $\sigma_{850} \sim 1.5\text{ mJy beam}^{-1}$ (HS1549) and $\sigma_{850} \sim 0.9\text{ mJy beam}^{-1}$ (HS1700).

We used a peak finding algorithm to choose sources whose per beam flux exceeded 4σ of the local noise in the variance map. We then found the position of these sources by fitting centroids to their peak position. Within our $850\mu\text{m}$ SCUBA-2 maps we have detected 29 $> 4\sigma$ sources (HS1549) and 27 $> 4\sigma$ sources (HS1700), as shown in Tables 2.1 and 2.2. The source at the centre of the HS1549 map has been resolved by SMA (observations described in § 2.2.2) and separates into three components, which are sufficiently separated to allow for SCUBA-2 $450\mu\text{m}$ measurements at each position (see § 2.3.3).

2.3.2 Number Counts

We show the cumulative number counts for all $> 4\sigma$ $850\mu\text{m}$ sources within each protocluster field in Figure 2.2. We compute the counts by counting up sources within each flux bin and dividing by the area for which we find these sources. For the field counts, if the flux bin is less than the average RMS of the entire field then

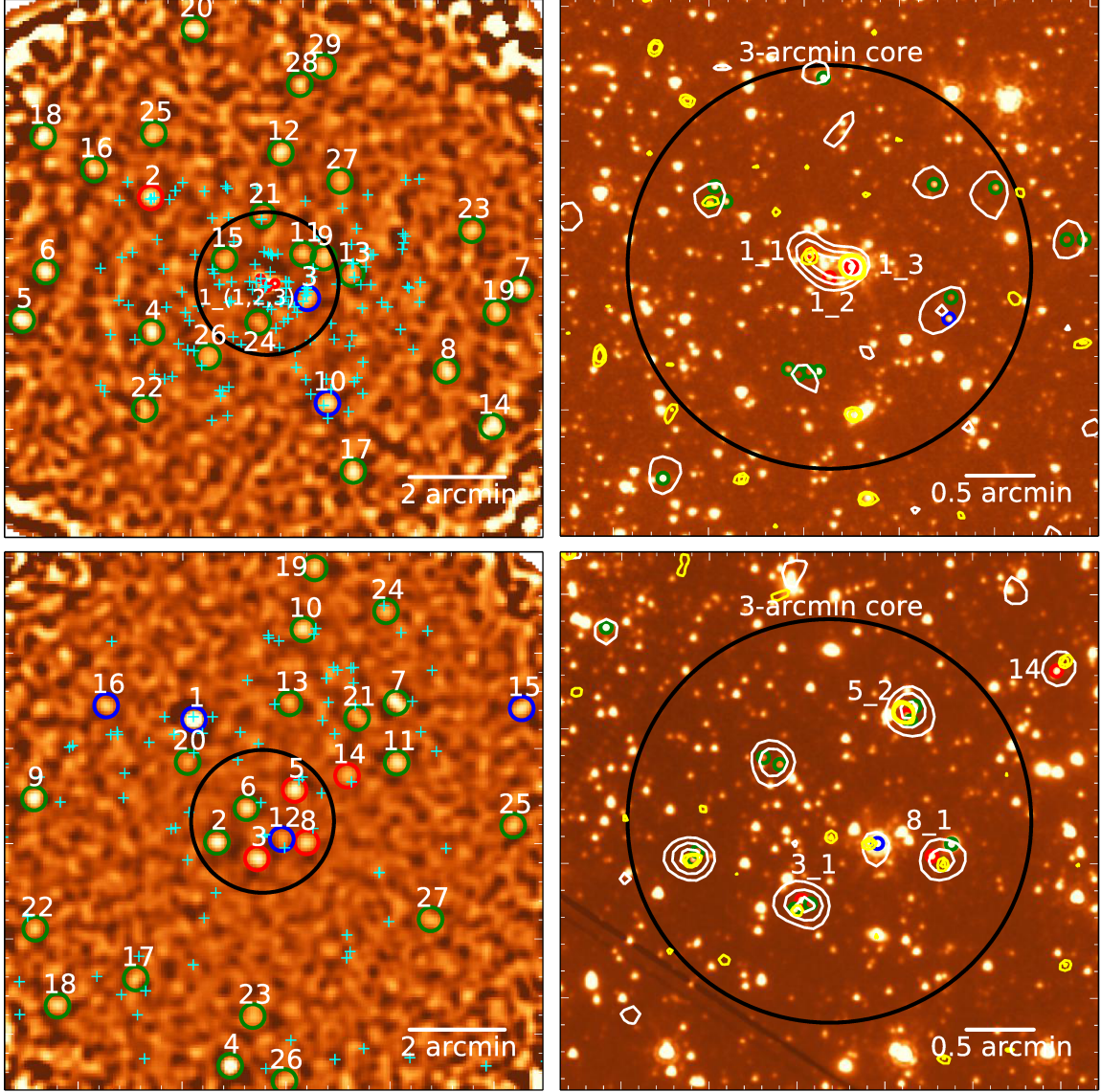


Figure 2.1: **Top:** HS1549. **Bottom:** HS1700. **Left:** SCUBA-2 850 μm images. The red circles are SMGs within the protoclusters, blue circles are SMGs residing outside of the protoclusters, and green circles are $> 4\sigma_{850}$ sources that have no spectroscopically confirmed redshifts. The cyan crosses represent all LBGs that reside within the protoclusters ($z_{\text{protocluster}} \pm 0.05$). **Right:** *Spitzer*-IRAC *ch2* images of the 3-arcmin core region of each protocluster field with white contours of $\text{SNR}_{850} = (3, 7, 11)$ and yellow contours of $\text{SNR}_{450} = (2.5, 3)$.

Table 2.1: 850 μm source catalogue of $> 4\sigma$ sources in HS1549. Sources with 450 μm counterparts have been included for $> 3\sigma$ if they reside within the 850 μm beam and $> 2.5\sigma$ if they match their IR-counterpart.

ID	α (J2000)	δ (J2000)	S_{850} (SNR) (mJy)	S_{450} (SNR) (mJy)
1.1 [†]	15 ^h 51 ^m 53.8 ^s	+19°11'09.9''	9.4 [†] (8.9) [†]	15(3.2)
1.2 [†]	15 ^h 51 ^m 53.2 ^s	+19°10'59.1''	5.6 [†] (5.3) [†]	–
1.3 [†]	15 ^h 51 ^m 52.5 ^s	+19°11'03.9''	8.8 [†] (8.4) [†]	30(6.3)
2	15 ^h 52 ^m 03.6 ^s	+19°12'52.3''	7.0(8.2)	19(3.0)
3	15 ^h 51 ^m 49.6 ^s	+19°10'45.2''	4.9(7.7)	–
4	15 ^h 52 ^m 03.5 ^s	+19°10'02.8''	7.2(7.7)	18(2.5)
5	15 ^h 52 ^m 15.0 ^s	+19°10'17.7''	8.3(7.5)	20(2.7)
6	15 ^h 52 ^m 12.9 ^s	+19°11'18.9''	7.5(7.3)	19(2.7)
7	15 ^h 51 ^m 30.7 ^s	+19°10'56.7''	7.4(7.0)	38(4.9)
8	15 ^h 51 ^m 37.3 ^s	+19°09'14.0''	5.9(6.6)	32(4.5)
9	15 ^h 51 ^m 48.2 ^s	+19°11'36.4''	4.2(6.2)	–
10	15 ^h 51 ^m 47.8 ^s	+19°08'33.1''	5.2(6.1)	–
11	15 ^h 51 ^m 50.0 ^s	+19°11'41.1''	3.9(6.0)	–
12	15 ^h 51 ^m 52.0 ^s	+19°13'48.9''	5.4(5.9)	–
13	15 ^h 51 ^m 45.7 ^s	+19°11'15.7''	4.2(5.7)	–
14	15 ^h 51 ^m 33.2 ^s	+19°08'03.9''	7.0(5.3)	–
15	15 ^h 51 ^m 57.0 ^s	+19°11'34.3''	3.3(4.9)	16(3.1)
16	15 ^h 52 ^m 08.6 ^s	+19°13'27.3''	4.9(4.8)	–
17	15 ^h 51 ^m 45.5 ^s	+19°07'07.6''	5.8(4.7)	–
18	15 ^h 52 ^m 13.1 ^s	+19°14'09.2''	7.8(4.6)	–
19	15 ^h 51 ^m 32.8 ^s	+19°10'27.6''	4.7(4.6)	–
20	15 ^h 51 ^m 59.7 ^s	+19°16'24.3''	6.1(4.5)	–
21	15 ^h 51 ^m 53.6 ^s	+19°12'29.6''	3.1(4.5)	–
22	15 ^h 52 ^m 04.1 ^s	+19°08'25.6''	3.9(4.4)	–
23	15 ^h 51 ^m 35.0 ^s	+19°12'10.9''	4.3(4.3)	–
24	15 ^h 51 ^m 54.0 ^s	+19°10'15.0''	2.7(4.2)	–
25	15 ^h 52 ^m 03.3 ^s	+19°14'13.0''	4.1(4.2)	–
26	15 ^h 51 ^m 58.4 ^s	+19°09'31.6''	3.3(4.2)	–
27	15 ^h 51 ^m 46.7 ^s	+19°13'13.0''	3.3(4.1)	–
28	15 ^h 51 ^m 50.3 ^s	+19°15'15.0''	4.8(4.1)	–
29	15 ^h 51 ^m 48.2 ^s	+19°15'37.6''	4.8(4.1)	–

[†] SMA detections

Table 2.2: 850 μm source catalogue of $> 4\sigma$ sources in HS1549. Sources with 450 μm counterparts have been included for $> 3\sigma$ if they reside within the 850 μm beam and $> 2.5\sigma$ if they match their IR-counterpart.

ID	α (J2000)	δ (J2000)	S_{850} (SNR) (mJy)	S_{450} (SNR) (mJy)
1	17 ^h 01 ^m 17.8 ^s	+64°14'37.3''	16.9(24.7)	30(4.2)
2	17 ^h 01 ^m 13.3 ^s	+64°12'02.8''	6.8(13.6)	18(3.7)
3	17 ^h 01 ^m 05.6 ^s	+64°11'42.1''	6.2(12.9)	14(2.9)
4	17 ^h 01 ^m 10.7 ^s	+64°07'20.7''	10.9(12.9)	30(3.9)
5	17 ^h 00 ^m 58.3 ^s	+64°13'08.3''	6.3(12.8)	21(4.5)
6	17 ^h 01 ^m 07.6 ^s	+64°12'45.3''	5.1(10.9)	–
7	17 ^h 00 ^m 38.7 ^s	+64°14'58.2''	6.6(9.7)	23(3.2)
8	17 ^h 00 ^m 56.1 ^s	+64°12'02.3''	4.6(9.6)	15(3.2)
9	17 ^h 01 ^m 48.6 ^s	+64°12'57.0''	7.3(8.5)	35(3.6)
10	17 ^h 00 ^m 56.7 ^s	+64°16'30.5''	5.0(7.3)	21(3.0)
11	17 ^h 00 ^m 38.6 ^s	+64°13'42.6''	5.0(7.3)	30(4.5)
12	17 ^h 01 ^m 00.8 ^s	+64°12'06.4''	2.6(5.6)	15(3.3)
13	17 ^h 00 ^m 59.3 ^s	+64°14'57.4''	3.3(5.3)	–
14	17 ^h 00 ^m 48.2 ^s	+64°13'26.2''	3.1(5.3)	–
15	17 ^h 00 ^m 14.5 ^s	+64°14'50.5''	4.7(5.1)	–
16	17 ^h 01 ^m 34.8 ^s	+64°14'54.4''	4.1(5.1)	30(3.3)
17	17 ^h 01 ^m 29.0 ^s	+64°09'10.5''	3.7(4.9)	–
18	17 ^h 01 ^m 44.0 ^s	+64°08'36.0''	4.6(4.8)	–
19	17 ^h 00 ^m 54.5 ^s	+64°17'47.5''	4.4(4.6)	–
20	17 ^h 01 ^m 19.0 ^s	+64°13'43.3''	2.7(4.6)	–
21	17 ^h 00 ^m 46.3 ^s	+64°14'38.8''	3.0(4.5)	–
22	17 ^h 01 ^m 48.3 ^s	+64°10'12.9''	3.9(4.5)	–
23	17 ^h 01 ^m 06.4 ^s	+64°08'23.3''	3.2(4.5)	–
24	17 ^h 00 ^m 40.6 ^s	+64°16'53.3''	3.5(4.5)	–
25	17 ^h 00 ^m 16.2 ^s	+64°12'23.0''	3.7(4.4)	–
26	17 ^h 01 ^m 00.3 ^s	+64°07'01.4''	3.8(4.4)	–
27	17 ^h 00 ^m 32.1 ^s	+64°10'25.2''	3.0(4.2)	–

the area is adjusted to the part of the map which is sensitive enough to detect these sources, but only sources that actually reside within these adjusted areas are counted.

We compare our flux counts to that of the SCUBA-2 Cosmology Legacy Survey (S2CLS) ([33]). S2CLS is a sub-millimetre survey which detected 3000 sub-millimetre sources over $\sim 5\text{deg}^2$ with an average $1\sigma_{850}$ sensitivity of 1.2 mJy beam^{-1} . We don't find any statistical over-density in HS1700 over the entire field for any flux bin compared to S2CLS. However, we find HS1549 to be $\sim 10 - 3\times$ overdense over the entire field compared to S2CLS until $S_{850} \lesssim 9\text{ mJy}$.

The number counts over the $< 3\text{-arcmin}$ diameter core show both fields to be significantly overdense compared to S2CLS. We find HS1549 to be $\sim 3-9\times$ overdense, while we find HS1700 to be $\sim 2 - 7\times$ overdense in its core. For fluxes $S_{850} > 3\text{ mJy}$ outside of the core region HS1549 has 23 sources and HS1700 has 20 sources. However, for $S_{850} > 4\text{ mJy}$ outside of the core HS1549 has approximately double the number of sources compared to HS1700. This then raises the question why is HS1700 more overdense at 3 mJy? This is because the area for which you can find 3 mJy sources in HS1549 is smaller, due to its relatively lower sensitivity compared to HS1700.

This analysis shows that although HS1549 doesn't look $\sim 2\times$ more dense in core than HS1700, the HS1549 field is somewhat more over-dense over its entire SCUBA-2 field, which is consistent with the larger and more massive structure.

From spectral identification we find that both protoclusters have 3 SMGs contributing to the protocluster core. This analysis shows that some of the most hyper luminous sources at large radii are in the protocluster, despite the counts at these radii not distinguishing themselves from the field.

We find a clear SMG over-density near HS1700's mean optical galaxy cluster centre, and only find a $\sim 36''$ offset north from average to median centre. [44] (Kato et al. 2016) suggests an offset centre position from a handful of *Herschel*-SPIRE sources, none of which are confirmed to lie within the protocluster. When applying our over-density analysis at the Kato's offset position ($\sim 2.1'$ north) we find no such evidence for excess. The absence of an SMG over-density at their offset position

suggests that Kato’s over-density analysis is likely not valid. Unfortunately, *Herschel*-SPIRE sources are very confusion limited at the protocluster’s redshift, $z = 2.3$, and thus they would be missing a lot of bright, but cold sources, like 850 μm -selected SMGs at $z = 2.3$. So, it is very unlikely their results represent any kind of reliable improvement to the optical centroid of the protocluster, which has to be much more reliable tracer of the mass distribution, as the optical sources are much longer lived.

2.3.3 Counterpart Identification

We use *Spitzer*-IRAC channels 2 and 4 (4.5 μm and 8 μm) in order to precisely determine the IR counterparts to our 850 μm identified sources. Multi-wavelength cutouts for each SCUBA-2 source are found in the Appendix.

The IRAC counterpart identification of sub-millimetre galaxies can be objectively justified by a statistical approach. We determine the reliability of an IRAC source association to the sub-millimetre source using Poisson statistics to calculate the probability of finding a source at random within some area. We employ P-values to each IRAC counterpart, where the P-value is described in [23] as:

$$P = 1 - \exp(-\pi\eta\theta^2) \quad (2.1)$$

where η is the IRAC source density within the 15'' SCUBA-2 beam at 850 μm and θ is the angular offset between IRAC source and the SCUBA-2 ID. A counterpart is considered a reliable match if $P \leq 0.05$, while we consider a counterpart to be a tentative match if $0.05 < P \leq 0.1$ (consistent with e.g. [40, 60, 12, 90, 93]). Using this procedure we have found secure IRAC counterparts for 8/37 (HS1549) and 11/39 (HS1700) SMGs and an additional 5/37 (HS1549) and 9/39 (HS1700) tentative counterparts. We present all IRAC identifications in Tables [2.3] and [2.4].

Within both fields there are five SCUBA-2 sources (1549.1, 1549.3, 1549.7, 1549.25, 1700.15) which are significantly elongated, which suggest they likely have multiple sub-millimetre counterparts.

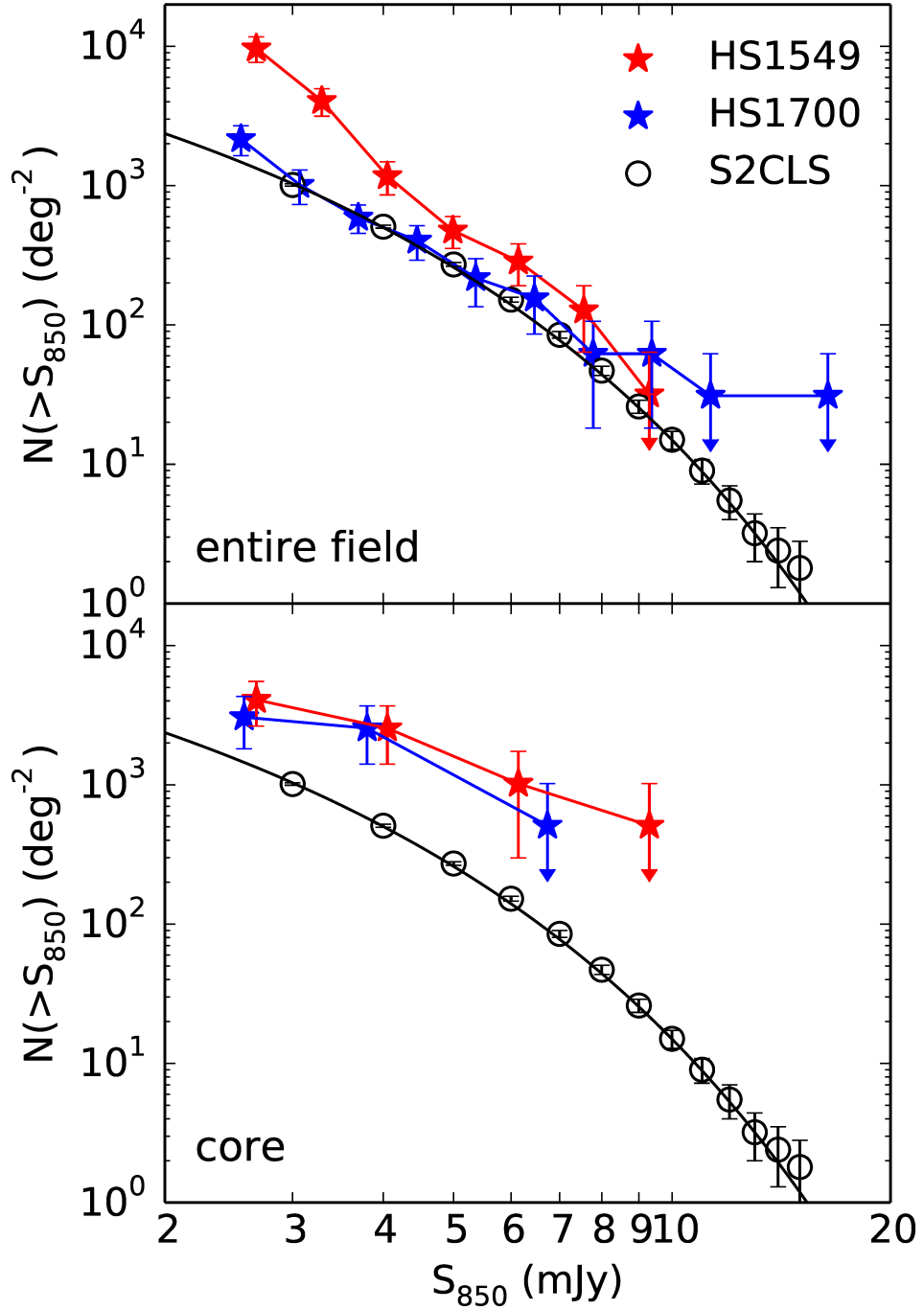


Figure 2.2: Cumulative number counts of $> 4\sigma$ $850 \mu\text{m}$ sources for each protocluster's field (**top**) and $< 3'$ core (**bottom**). The solid line shows a Schechter function fit to the cumulative counts of the SCUBA-2 Cosmology Legacy Survey ([33]). The error bars represent the uncertainties derived from Poisson statistics.

We search for possible gravitationally lensed counterparts and we found the counterpart to the 850 μm source, *1549.16*, is likely being lensed by a massive foreground galaxy, as evidenced by the bright IRAC source offset from the 850/450 μm centroids.

In HS1700 we do not have MIPS or near-IR data for 7/27 SCUBA-2 sources, making ID's more uncertain. Furthermore, in HS1549 there is no available MIPS or IRAC data for 8/29 sources, making IR identification impossible for these sources. We exclude these sources from our protocluster membership analysis.

There are four cases in HS1549 (*1549.12*, *1549.22*, *1549.24*, *1549.27*) and five cases in HS1700 (*1700.2*, *1700.3*, *1700.7*, *1700.10*, *1700.27*) where IRAC identifications cannot be reliably measured at 24 μm because a nearby bright 24 μm source point spread function overlaps the IRAC position, making the precision of the IR identifications less precise.

We use SMA to resolve the central bright source in HS1549, *1549.1*, the SMA observations are described in § 2.2.2. We detect three compact components at $> 5\sigma$, *1549.1-1* (MD17), and *1549.1-2* (PdBI-1), *1549.1-3* (Q1549), which are consistent with the elongated SCUBA-2 morphology, and we present their fluxes and positions in Table 2.1. The astrometric uncertainties are $\Delta\alpha = 0.24\text{-arcsec}$ (0.20-arcsec systematic; 0.13-arcsec statistical) and $\Delta\delta = 0.22\text{-arcsec}$ (0.19-arcsec systematic; 0.10-arcsec statistical).

2.4 Discussion

2.4.1 Cluster Membership

To analyze our SCUBA-2 sources we used several additional spectroscopic and photometric data sets. Using CO detections, near-IR and optical spectroscopy we find 3 (4) SMGs solidly identified in HS1549 (HS1700) and one SMG likely identified within each protocluster.

Table 2.3: IRAC counterparts for all SCUBA-2 $> 4\sigma$ sources in HS1549. The secure identifications at $4.5 \mu\text{m}$ or $24 \mu\text{m}$ with $P \leq 0.05$ are shown in bold and tentative associations ($0.05 < P \leq 0.10$) are presented in italics. SCUBA-2 IDs without any identifiable IRAC counterparts have been left out of the table.

ID	α (J2000)	δ (J2000)	IRAC – $850\mu\text{m}$ (arcsec)	P_{IRAC}
1_1 [†]	+15 ^h 51 ^m 53.7 ^s	+19°11′10.0″	0.00 [†]	0.001 [†]
1_2 [†]	+15 ^h 51 ^m 53.2 ^s	+19°10′59.3″	0.00 [†]	0.001 [†]
1_3 [†]	+15 ^h 51 ^m 52.5 ^s	+19°11′04.0″	0.00 [†]	0.001 [†]
2	+15 ^h 52 ^m 3.3 ^s	+19°12′51.5″	3.31	0.177
3_1	+15 ^h 51 ^m 49.4 ^s	+19°10′40.8″	5.04	0.363
3_2	+15 ^h 51 ^m 49.4 ^s	+19°10′50.3″	6.20	0.496
4	+15 ^h 52 ^m 03.4 ^s	+19°10′01.5″	1.64	0.047
8	+15 ^h 51 ^m 37.1 ^s	+19°09′13.3″	2.36	0.094
9	+15 ^h 51 ^m 48.0 ^s	+19°11′39.3″	4.13	0.262
10	+15 ^h 51 ^m 47.5 ^s	+19°08′33.2″	4.27	0.277
11	+15 ^h 51 ^m 49.9 ^s	+19°11′40.7″	1.54	0.041
12_1	+15 ^h 51 ^m 52.0 ^s	+19°13′53.4″	4.56	0.309
12_2	+15 ^h 51 ^m 52.0 ^s	+19°13′45.8″	3.12	0.159
12_3	+15 ^h 51 ^m 51.8 ^s	+19°13′43.8″	5.59	0.426
12_4	+15 ^h 51 ^m 52.2 ^s	+19°13′41.7″	8.15	0.693
13_1	+15 ^h 51 ^m 45.7 ^s	+19°11′16.1″	0.87	0.013
13_2	+15 ^h 51 ^m 45.2 ^s	+19°11′16.2″	6.96	0.577
15_1	+15 ^h 51 ^m 56.9 ^s	+19°11′32.9″	1.46	0.037
15_2	+15 ^h 51 ^m 56.8 ^s	+19°11′39.7″	5.90	0.461
15_3	+15 ^h 51 ^m 56.5 ^s	+19°11′33.1″	7.42	0.624
17_1	+15 ^h 51 ^m 45.2 ^s	+19°07′09.1″	5.46	0.411
17_2	+15 ^h 51 ^m 46.0 ^s	+19°07′05.9″	7.12	0.593
21	+15 ^h 51 ^m 53.4 ^s	+19°12′28.1″	3.13	0.159
22_1	+15 ^h 52 ^m 04.1 ^s	+19°08′25.5″	1.04	0.019
22_2	+15 ^h 52 ^m 04.1 ^s	+19°08′28.9″	3.28	0.174
23	+15 ^h 51 ^m 35.3 ^s	+19°12′09.2″	4.22	0.271
24_1	+15 ^h 51 ^m 53.5 ^s	+19°10′17.3″	7.07	0.589
24_2	+15 ^h 51 ^m 53.8 ^s	+19°10′17.3″	3.38	0.184
<i>24_3</i>	+15 ^h 51 ^m 54.2 ^s	+19°10′15.8″	2.42	0.099
24_4	+15 ^h 51 ^m 54.5 ^s	+19°10′18.3″	7.63	0.645
25_1	+15 ^h 52 ^m 03.1 ^s	+19°14′14.3″	2.75	0.126
25_2	+15 ^h 52 ^m 03.4 ^s	+19°14′08.2″	5.28	0.391
<i>26_1</i>	+15 ^h 51 ^m 58.4 ^s	+19°09′29.6″	2.07	0.073
<i>27_1</i>	+15 ^h 51 ^m 46.6 ^s	+19°13′13.3″	1.74	0.053
27_2	+15 ^h 51 ^m 46.6 ^s	+19°13′08.5″	4.76	0.332
<i>28_1</i>	+15 ^h 51 ^m 50.2 ^s	+19°15′12.9″	2.29	0.089
28_2	+15 ^h 51 ^m 50.3 ^s	+19°15′09.6″	5.35	0.399

[†] SMA detections

Table 2.4: IRAC counterparts for all SCUBA-2 $> 4\sigma$ sources in HS1700. The secure identifications at $4.5 \mu\text{m}$ or $24 \mu\text{m}$ with $P \leq 0.05$ are shown in bold and tentative associations ($0.05 < P \leq 0.10$) are presented in italics. SCUBA-2 IDs without any identifiable IRAC counterparts have been left out of the table.

ID	α (J2000)	δ (J2000)	IRAC $- 850\mu\text{m}$ (arcsec)	P_{IRAC}
1	+17 ^h 01 ^m 17.6 ^s	+64°14'37.850''	1.11	0.022
<i>2_1</i>	+17 ^h 01 ^m 13.1 ^s	+64°12'01.980''	1.82	0.057
<i>2_2</i>	+17 ^h 01 ^m 12.8 ^s	+64°12'05.420''	4.33	0.283
3_1	+17 ^h 01 ^m 5.7 ^s	+64°11'43.690''	1.64	0.047
<i>3_2</i>	+17 ^h 01 ^m 6.2 ^s	+64°11'39.730''	4.31	0.281
<i>3_3</i>	+17 ^h 01 ^m 5.1 ^s	+64°11'42.100''	3.47	0.192
4	+17 ^h 01 ^m 10.8 ^s	+64°07'20.750''	0.49	0.004
<i>5_1</i>	+17 ^h 00 ^m 57.9 ^s	+64°13'10.310''	3.30	0.176
<i>5_2</i>	+17 ^h 00 ^m 58.5 ^s	+64°13'06.160''	2.28	0.088
<i>5_3</i>	+17 ^h 00 ^m 58.2 ^s	+64°13'03.680''	4.62	0.316
<i>6_1</i>	+17 ^h 01 ^m 7.2 ^s	+64°12'44.240''	3.28	0.174
<i>6_2</i>	+17 ^h 01 ^m 8.3 ^s	+64°12'47.360''	4.76	0.331
<i>7_1</i>	+17 ^h 00 ^m 39.0 ^s	+64°14'58.300''	1.91	0.063
<i>7_2</i>	+17 ^h 00 ^m 38.8 ^s	+64°15'01.270''	3.09	0.156
<i>7_3</i>	+17 ^h 00 ^m 37.7 ^s	+64°14'55.430''	6.78	0.558
<i>7_4</i>	+17 ^h 00 ^m 37.1 ^s	+64°14'53.240''	11.26	0.895
<i>8_1</i>	+17 ^h 00 ^m 56.8 ^s	+64°12'03.430''	4.94	0.352
<i>8_2</i>	+17 ^h 00 ^m 55.4 ^s	+64°12'08.800''	7.67	0.648
<i>9</i>	+17 ^h 01 ^m 48.7 ^s	+64°12'58.700''	1.73	0.052
10_1	+17 ^h 00 ^m 56.6 ^s	+64°16'31.310''	0.99	0.017
<i>10_2</i>	+17 ^h 00 ^m 57.1 ^s	+64°16'29.810''	3.30	0.176
<i>12</i>	+17 ^h 01 ^m 0.5 ^s	+64°12'09.090''	3.46	0.192
13	+17 ^h 00 ^m 59.2 ^s	+64°14'58.180''	1.24	0.027
14	+17 ^h 00 ^m 48.3 ^s	+64°13'26.040''	0.34	0.002
15_1	+17 ^h 00 ^m 14.6 ^s	+64°14'51.340''	1.46	0.037
<i>15_2</i>	+17 ^h 00 ^m 13.7 ^s	+64°14'51.030''	5.06	0.366
<i>16</i>	+17 ^h 01 ^m 34.9 ^s	+64°14'52.810''	1.82	0.057
<i>17</i>	+17 ^h 01 ^m 29.1 ^s	+64°09'07.470''	3.15	0.162
18	+17 ^h 01 ^m 44.2 ^s	+64°08'36.190''	1.47	0.038
<i>19</i>	+17 ^h 00 ^m 54.3 ^s	+64°17'45.830''	2.00	0.069
<i>20</i>	+17 ^h 01 ^m 19.1 ^s	+64°13'45.270''	1.98	0.067
<i>22</i>	+17 ^h 01 ^m 48.5 ^s	+64°10'11.110''	2.10	0.076
<i>23</i>	+17 ^h 01 ^m 6.0 ^s	+64°08'20.090''	4.13	0.261
24	+17 ^h 00 ^m 40.6 ^s	+64°16'53.560''	0.64	0.007
<i>25</i>	+17 ^h 00 ^m 16.1 ^s	+64°12'20.710''	2.40	0.098
<i>26_1</i>	+17 ^h 01 ^m 0.3 ^s	+64°06'58.290''	3.11	0.158
26_2	+17 ^h 01 ^m 0.3 ^s	+64°07'00.760''	0.67	0.008
27_1	+17 ^h 00 ^m 32.1 ^s	+64°10'25.140''	0.14	0.001
<i>27_2</i>	+17 ^h 00 ^m 31.5 ^s	+64°10'24.760''	4.05	0.253

Optical Spectroscopy

We determine the redshift of two of the three sub-millimetre counterparts of the central sub-millimetre source in HS1549, *1549.1* as mentioned in § 2.3.3. Using optical spectroscopy we find *1549.1_1* (MD17) ($z = 2.856$) and *1549.1_3* ($z = 2.847$), both residing within the protocluster and SMA identifies the sub-millimetre emission as coming from these sources.

The central QSO in both protocluster fields, *1549.1_2* (Q1549) *1700.12* (Q1700), were spectroscopically identified at $z = 2.72$ and $z = 2.84$, respectively, in the Hamburg quasar survey ([62]). Thus *1700.12* resides outside of the protocluster and *1549.1_2* resides within the protocluster.

IRAM-PdBI CO(3-2)

We observed the three sub-millimetre counterparts resolved by SMA with IRAM-PdBI, duplicating redshift measurements for both *1549.1_1* (MD17) and *1549.1_3*. The details of these observations are also found in Chapman et al. in preparation. The positions of the 870 μm sources are consistent within $0.2''$ with the centroid of the line and continuum measurements from PdBI for all three counterparts. We find that all three sources to be contained within the protocluster: *1549.1_1* (MD17) ($z = 2.856$), *1549.1_2* (Q1549) ($z = 2.851$), and *1549.1_3* (PdBI-1) ($z = 2.847$).

With the same IRAM-PdBI program we have discovered *1549.3* resides at redshift $z = 2.918$, which is too far from the peak redshift distribution to be in the cluster core, however it resides in a secondary redshift peak which will likely collapse into the same structure by $z = 0$. Additionally, we find *1549.10* to be a null detection of, which suggests this source does not reside at the protocluster's redshift.

In [13] the brightest SMG in the HS1700 field, *1700.1*, was identified at $z = 2.816$, residing outside of the protocluster. In the same PdBI program, we have determined *1700.15* to not reside within the protocluster via a null detection.

Near-IR Spectroscopy

We have followed up eleven sub-millimetre sources within HS1700 using *GNIRS* and the details of these observations are found in § 2.2.3. We have confirmed 4/11 protocluster members while accumulating 6/11 null detection. We found *1700.3_1* ($z = 2.318$), *1700.5_2* ($z = 2.313$), *1700.8_1* ($z = 2.303$), and *1700.14* ($z = 2.306$). In the same *GNIRS* program Ross et al. in preparation found *1700.16_1* to reside out of the protocluster at $z = 1.575$. In all cases the SMG is either a secure identification ($P \leq 0.05$) or a tentative association ($0.05 < P \leq 0.10$) to their IRAC counterpart.

NB-imaging

We determine cluster membership from IRAC IDs discussed in § 2.3.3, which are associated with previously detected LBGs. These catalogues consist of NB-selected galaxies based on deep U_n , G , and \mathcal{R} images using the *William Herschel Telescope* ([79]), as well as spectroscopically identified LBGs using the *LRIS-B* Slitmasks on *Keck* [81]. For the SCUBA-2 ID *1549.2* we found three existing spectroscopic detections within the SCUBA-2's $15''$ beam which all reside within the protocluster: *ID82* ($z = 2.8374$), *ID85* ($z = 2.8353$), and *ID158* ($z = 2.84175$). Although none of these LBGs are associated to the IRAC ID, the LBGs are likely associated to the SCUBA-2 ID.

Using the same technique we've found the SCUBA-2 ID *1549.4* is equally likely associated with two distinguishably different galaxies, an LBG (ID88) and an IRAC ID, both with $P < 0.05$. The LBG resides at $z = 2.3878$, outside of the HS1549 protocluster, and thus *1549.4* might also reside outside of the protocluster.

Photometric Redshifts

We've identified two narrow-band selected LBGs that align with IRAC IDs in HS1700 with no recorded redshift, however as they were photometrically detected and colour-selected they are possible protocluster candidates (*1700.5_1*: *DRG46*, *1700.5_3*: *DRG44*).

2.4.2 Star-Formation Activity

There appears to be significant sub-millimetre overdensities near the core regions of each protocluster. We spectroscopically confirm there to be four SMGs residing within each protocluster, and in this section we determine how much each SMG contributes to the protocluster’s star formation and thus evolution.

Star Formation Rate Calculations

We calculate the star formation rate (SFR) of SCUBA-2 850 μm detected SMGs with a conversion given by [4]:

$$\text{SFR} (M_{\odot} \text{ yr}^{-1}) = 200 \times S_{850\mu\text{m}} \text{ (mJy)} \quad (2.2)$$

which assumes the use of the [45] star formation calculation for sources at $z > 1.5$.

As mentioned in § 2.4.1, we found four SCUBA-2 detected SMGs within each protocluster. Using Equation 2.2 we find that these protocluster SMGs contribute $5900 \pm 700 M_{\odot} \text{ yr}^{-1}$ (HS1549) and $4000 \pm 400 M_{\odot} \text{ yr}^{-1}$ (HS1700), to each protocluster.

To compute star formation rates for all known protocluster galaxies undetected at 850 μm (e.g. LBGs) we assume the conversion given by [63]:

$$\text{SFR} (M_{\odot} \text{ yr}^{-1}) = \begin{cases} 7.8 \times 10^{-10} L(24 \mu\text{m}, L_{\odot}) & (a) \\ 2.6 \times 10^{-10} L(24 \mu\text{m}, L_{\odot})^{1.048} & (b) \end{cases} \quad (2.3)$$

where $L(24 \mu\text{m}, L_{\odot})$ is the rest frame *Spitzer*-MIPS 24 μm luminosity with no band-pass corrections, and where condition (a) is $5 \times 10^9 L_{\odot} \leq L(\text{TIR}) \leq 1 \times 10^{11} L_{\odot}$ and condition (b) is $L(\text{TIR}) > 1 \times 10^{11} L_{\odot}$. Here $L(\text{TIR})$ corresponds to the full infrared 8 – 1000 μm . This conversion does not account for AGN heating of dust in this wavelength regime, even though AGN fractional contribution is known to be non-negligible (10 – 30%).

By applying Equation 2.3 to all known protocluster galaxies undetected at 850 μm we find the total star formation rate from LBGs to be $10,200 \pm 500 M_{\odot} \text{ yr}^{-1}$

Table 2.5: Estimated star formation rates for contributing sources.

SFR _{tot} (M _⊙ yr ⁻¹)	HS1549	HS1700
LBGs (24 μm)	10,200±500	2800±200
Undetected LBGs (24 μm)	560±70	360±60
LBGs (850 μm)	5700±1000	3500±800
SMGs (850 μm)	5900±700	4000±400
All (24 μm + 850 μm)	16,100 ±900	6800±500

(HS1549) and $2800 \pm 200 \text{ M}_{\odot} \text{ yr}^{-1}$ (HS1700). The addition of $24 \text{ }\mu\text{m}$ undetected LBGs only add $\sim 510 \pm 70 \text{ M}_{\odot} \text{ yr}^{-1}$ (HS1549) and $\sim 360 \pm 60 \text{ M}_{\odot} \text{ yr}^{-1}$ (HS1700) to the total SFR, assuming these all have $\text{SFR} \sim 10 \text{ M}_{\odot} \text{ yr}^{-1}$ (consistent with being undetected at $24 \text{ }\mu\text{m}$).

The uncertainty of both the $850 \text{ }\mu\text{m}$ and $24 \text{ }\mu\text{m}$ derived SFRs are dominated by the uncertainties in their fluxes. To adjust for the position of the Polycyclic Aromatic Hydrocarbons emission line at $z = 2.85$ the $24 \text{ }\mu\text{m}$ derived SFR for HS1549’s LBGs has been boosted by a factor of two.

In Table 2.5, we present calculations of the total SFRs of each protocluster. In Figure 2.3 we show the in mass normalized integrated SFR as a function of redshift for HS1549 and HS1700, compared to other galaxy clusters from the literature (SA22 [76, 77]; HDF1.99 [14]; GCLASS [57]; CIJ0218 [75]; RCS [91]; MRC1138 [19]; PCL1002+0222 [9]; XCSJ2215 [50]).

We measure the galaxy over-density by contrasting the background removed redshift spikes from colour selected galaxies from the large spectroscopic survey from [78]. We find highly significant galaxy over-densities at $z = 2.300 \pm 0.015$ with $\delta_g^z \simeq 7$ (HS1700) and $z = 2.85 \pm 0.05$ with $\delta_g^z \simeq 10$ (HS1549). The galaxy over-density of the HS1549 protocluster is about $1.5\times$ that of the HS1700 protocluster, therefore we crudely estimate the mass of the HS1549 protocluster to be $M_{\text{cl}}^{\text{HS1549}} \sim 1.5 \times M_{\text{cl}}^{\text{HS1700}}$, where $M_{\text{cl}}^{\text{HS1700}} \sim 10^{14} M_{\odot}$ [78]. We adopt a 50% systematic uncertainty in the cluster halo mass in our error bars, which is likely a significantly larger source of uncertainty than our SFR estimates.

There must have been large amounts of star formation in the early Universe to have formed the massive galaxies we see today at $z = 0$. Star formation activity peaked around $z \sim 2$ (e.g. [37]), thus we'd expect the $\text{SFR}/M_{\text{cl}} - z$ relation to be steeper for higher z and begin to flatten out at $z \sim 2$. Our findings show that the HS1549 and HS1700 protoclusters generally seem to follow a trend extending from $z < 1$ rich clusters ([61]), with a $(1 + z)^7$ relation.

An interesting aspect of our findings is that our two massive protoclusters reveal mass weighted total SFRs comparable to two systems which show much less significant over densities in LBGs (HDF1.99 and PCL1002), and are plausibly hosted by much more massive dark matter halos. Two other protoclusters showing comparable LBG over densities to HS1549 and HS1700 (SSA22 and MRC1138) are apparently less active in ongoing star formation, suggesting that a range of activities and assembly histories are possible for massive protoclusters at $z \sim 2 - 3$

Combining SMGs and less luminous protocluster members and assuming a 10% uncertainty in volume, we measure central star formation rate densities (SFRDs) of $3800 \pm 1200 \text{ M}_{\odot} \text{ yr}^{-1} \text{ Mpc}^{-3}$ (HS1549) and $1600 \pm 500 \text{ M}_{\odot} \text{ yr}^{-1} \text{ Mpc}^{-3}$ (HS1700). These star formation rate densities are $\sim 10^4 \times$ larger than the global star formation rate densities found at their respective epochs ([51]). The SFRD found for HS1700 is comparable to the SFRD computed by [44] using their *Herschel*-SPIRE sources.

850 μm Stacking

We measure the sub-millimetre flux at each LBG position in the 850 μm beam-convolved map, discarding any LBG position where $-2\sigma \leq S_{850} \leq +4\sigma$. The upper flux limit defines the SCUBA-2 detections. We chose the lower flux limit as we found that the average negative flux of the bowling regions is -2σ , and on average $\sim 10\%$ of the flux outside of the bowling regions is below the -2σ limit. Each 850 μm flux is weighted by the inverse of the variance, where the variance is measured in the noise map. We then stack the weighted fluxes and compute the stack as $\sum(S_i/\sigma_i)/\sum(1/\sigma_i)$. We compare the 24 μm SFR calculations with 850 μm derived SFRs for protocluster

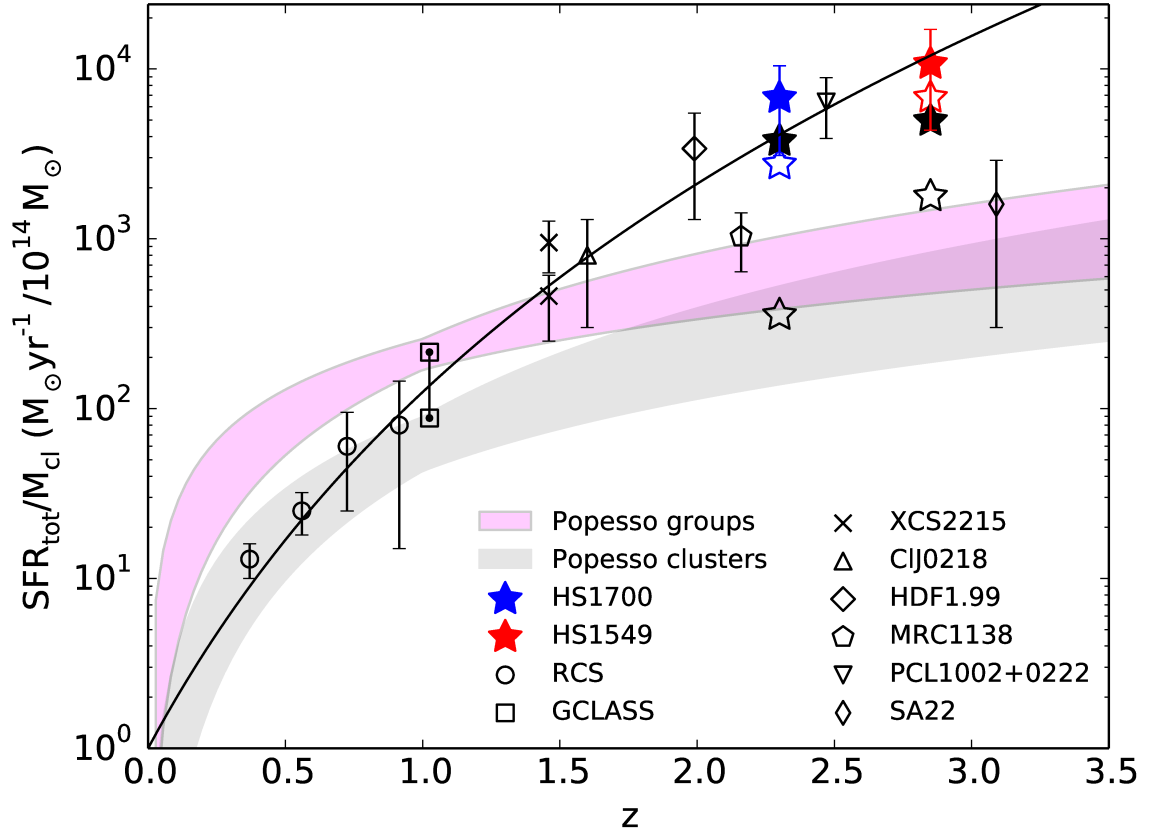


Figure 2.3: Integrated star-formation rate of clusters and groups normalized by their total (virial) mass as a function of redshift. The protoclusters considered in this work are shown as stars. The empty stars represent the contribution from LBGs alone and the filled stars include star formation from SCUBA-2 detected SMGs within each protocluster. The black stars represent the star formation activity within the core of the protocluster. The black curve show a $\propto (1+z)^7$ fit.

LBGs using Equation [2.2](#).

We find the 850 μm stacks to be $\langle S_{850} \rangle = 0.25 \pm 0.05$ mJy (HS1549: 114 galaxies) and $\langle S_{850} \rangle = 0.21 \pm 0.05$ mJy (HS1700: 83 galaxies), resulting in 850 μm SCUBA-2 derived SFRs of $5700 \pm 1000 M_{\odot} \text{ yr}^{-1}$ (HS1549) and $3500 \pm 800 M_{\odot} \text{ yr}^{-1}$ (HS1700).

Stacked 850 μm SFRs are a crude comparison to the 24 μm SFRs, which are much more precise on account of detecting every object and having a precision SFR for each member. Weak or non-detection of 850 μm are a good way to confirm that an ultra-bright 24 μm source is an AGN, rather than driven by star formation.

2.5 Conclusions

We have presented an analysis of a SCUBA-2 sub-millimetre follow up survey for the HS1549 and HS1700 protocluster fields, containing two of the largest know galaxy over-densities at $z > 2$. We conclude:

- We detect 56 SMGs at 850 μm in the deep SCUBA-2 maps over both HS1549 and HS1700 survey fields, containing two of the largest galaxy over-densities at $z > 2$. The number counts indicate significant over-densities in the ~ 500 kpc core region of $\sim 6 \times$ (HS1549) and $\sim 4 \times$ (HS1700).
- IR counterparts are identified for the SMGs via multi-wavelength identification using near- and far-IR archival data. We employ P-values to each IR counterpart and identify one possible member within each protocluster. Using CO detections, near-IR and optical spectroscopy we determine 3 (4) SMGs solidly identified in the HS1549 (HS1700) protocluster.
- Combining SCUBA-2 detected SMGs within the protoclusters and less luminous members we find both protocluster have large integrated mass-normalized star formation rates that are consistent with a $\propto (1+z)^7$ trend. Both protoclusters have star formation rate densities $\sim 10^4 \times$ larger than the global star formation rate densities found at their respective epochs.

- Stacking all known protocluster galaxies and field galaxies we have found a statistically significant increase in sub-millimetre activity of protocluster galaxies.

Chapter 3

The JCMT Transient Survey: Data Reduction and Calibration Methods

3.1 Introduction

Although there have been many advances made in understanding low mass star formation over the past ten years (see, for example, [22], [88], [1]), the manner in which mass assembles onto a forming star remains a crucial open question. As [46] first demonstrated, assuming the mass accretion process onto a young star occurs at a constant rate (steady inside out collapse; [73]) gives rise to “The Low Luminosity Problem”: the empirical result that the median protostellar luminosity is measured to be approximately an order of magnitude less than the expected value. In recent years, this problem has been confirmed and emphasised by *Spitzer Space Telescope* observations through which even lower luminosities have been discovered (see [26], [31], [30], [25], [27]). One solution to this problem is that the accretion does not proceed at a constant rate. Rather, it occurs during episodic events which may be accompanied by outbursts that can be detected at infrared and sub-millimetre wavelengths (see [54] and [42]). Outside of the JCMT Transient Survey, there have already been two confirmed millimetre sources (both embedded protostars) which have shown direct evidence of an active burst accretion phase accompanied by a dramatic brightening, HOPS 383 in Orion ([68]; using *Spitzer Space Telescope* and *Wide-field Infrared Survey Explorer* (*WISE*) data), and MM1 in NGC6334I ([39]; using Atacama Large Millimeter/Sub-Millimeter Array and Sub-Millimeter Array data).

The JCMT Transient survey (Herczeg et al. in preparation) is a three year project dedicated to observing variability in deeply embedded protostars at sub-millimetre wavelengths with the sub-millimetre Common User Bolometer Array 2 (SCUBA-2;

[36]). The Transient survey monitors eight regions selected from the JCMT Gould Belt Survey [89] that have a high density of known protostellar and disk sources at an approximate 28 day cadence when they are observable in the sky. SCUBA-2 uses approximately 10,000 bolometers subdivided into two arrays to observe at both 450 μm and 850 μm simultaneously (see § 1.4.2). While we expect sources undergoing an accretion burst event to show a stronger signal at 450 μm [42], in this thesis we focus only on the 850 μm data. The noise levels in 450 μm maps are much more dependent on the weather than their 850 μm counterparts, causing the signal-to-noise ratio (SNR) to fall dramatically when there is more water vapour in the atmosphere (see § 1.4.1). In addition, the beam profile is less stable than at 850 μm requiring careful attention in order to make precise measurements of compact objects. We thus start here by defining the 850 μm calibration, which will then be used to calibrate the 450 μm data at a later date.

In order to track the peak brightnesses of sub-millimetre emission sources over each epoch, we test and employ a robust data reduction method and use multiple observations of the same regions to derive post-reduction image alignment. Reducing SCUBA-2 data is a complex process with several user-defined parameters which affect the final image produced (for detailed information on SCUBA-2 data reduction procedures, see § 1.4.3 and [11]). A large amount of work has been invested in understanding the optimal data reduction parameters to use for differing science goals (see, for example, [52]) depending on the scan pattern of the telescope and the amount of large-scale structure that needs to be robustly recovered. In all cases, the nominal JCMT pointing error is $\sim 2 - 6''$ (EAO staff, *private communication*) and the flux calibration is uncertain to $\sim 5 - 10\%$ [20]. While this is sufficient for most projects which use JCMT data, both of these uncertainties can be improved upon when there are multiple observations of regions with bright sources taken in a consistent manner. In this thesis, I seek to improve the spatial alignment of the JCMT Transient Survey data by approaching the problem from a relative point of view.

Properly matching faint, potential protostellar sources over the observed epochs

and co-adding those observations with high precision for the highest SNR requires sub-pixel accuracy ($\ll 3''$ at $850 \mu\text{m}$) in the spatial alignment. Thus, my goal is to increase the spacial alignment in order to reduce the uncertainty in the flux calibration. Small flux variations due to episodic accretion over few year timescales are expected to occur much more frequently than large flux variations (see, for examples, the models of [3], [87], and Herczeg et al. in preparation) and observations like those performed throughout the JCMT Transient Survey will help constrain the current models. Note that the techniques I have developed cater to any JCMT data obtained in a similar manner, and thus I am able to successfully align and calibrate archival data such as those which were obtained by the Gould Belt Survey and Mairs et al. in preparation will include these data in a follow-up analysis.

This chapter is organised as follows: In Section 3.2 I summarise the details of the SCUBA-2 observations for the JCMT Transient Survey. In Section 3.3 I outline the data reduction methods and showcase four tests performed which altered the amount of large-scale structure recovered in a given map or the initial conditions offered to the map-making pipeline in order to select the most robust techniques for the purpose of detecting transient events in deeply embedded protostars. In Section 3.4 I detail the post-reduction spatial alignment method applied to all current JCMT Transient data and propose an alternative approach to align images to a higher degree of precision and accuracy. In Section 3.5 and 3.6 I present an analysis on my alternative alignment method and compare it's results to current post-reduction methods. Finally, I present the conclusions in Section 3.7.

3.2 Observations

The JCMT Transient Survey observations are performed simultaneously at 450 and $850 \mu\text{m}$ with effective beam sizes of $9.8''$ and $14.6''$ (§ 1.4.2, [20]), respectively, using the Sub-Millimetre Common User Bolometer Array 2 (SCUBA-2; [36]). Transient uses the PONG1800 mapping mode (§ 1.4.2, [43]) which yields circular maps 0.5° in

diameter. There are eight nearby (<500 pc) regions selected from the Gould Belt Survey ([89], Herczeg et al. in preparation) which are each monitored at an approximate 28 day cadence when they are observable in the sky. Contained within these regions are a total of 984 young stellar objects (YSOs) identified by *Spitzer Space Telescope* ([55], [24]) and *Herschel Space Observatory* [82] observations. Table 3.1 shows a list of the regions and their central coordinates along with the average $850 \mu\text{m}$ RMS noise measured in the individual maps. Due to the weather, the $450 \mu\text{m}$ observations have noise values 10 to 40 times higher than the $850 \mu\text{m}$ observations and, thus, throughout this work I focus on the $850 \mu\text{m}$ data. Observations began in December 2015 and will continue until December 2018. Here, I present results between December 22nd, 2015 and September 29th, 2016. All of the regions are shown in Figures 3.1 and 3.2.

As mentioned in § 1.4.1, there are five weather grades defined for JCMT observations from Band 1 (very dry: $\tau_{225 \text{ GHz}} < 0.05$, where $\tau_{225 \text{ GHz}}$ is the opacity of the atmosphere at 225 GHz) to Band 5 (very wet: $\tau_{225 \text{ GHz}} > 0.2$). All of the observations performed in this survey were taken in either Band 1, Band 2, or Band 3 weather ($\tau_{225 \text{ GHz}} < 0.08$).

3.3 Data Reduction Methods

The data reduction procedure was performed using the iterative map-making technique *makemap* (explained in detail by [11]) in the SMURF package [41] found within the STARLINK software [18]. Please refer to § 1.4.3 and § 2.2 for detailed explanations of this map-making process. In the case of the JCMT Transient Survey, the final maps are gridded to $3''$ pixels for the $850 \mu\text{m}$ data and $2''$ pixels for the $450 \mu\text{m}$ data.

To apply additional constraints to the solution derived by *makemap*, the user can also supply an *external mask* which surrounds the astronomical signal deemed to be significant. To construct an external mask, the individual maps produced by the iterative mapmaker are co-added in order to achieve a higher signal-to-noise ratio (SNR) and the resulting image is used to define the regions of genuine astronomical emission

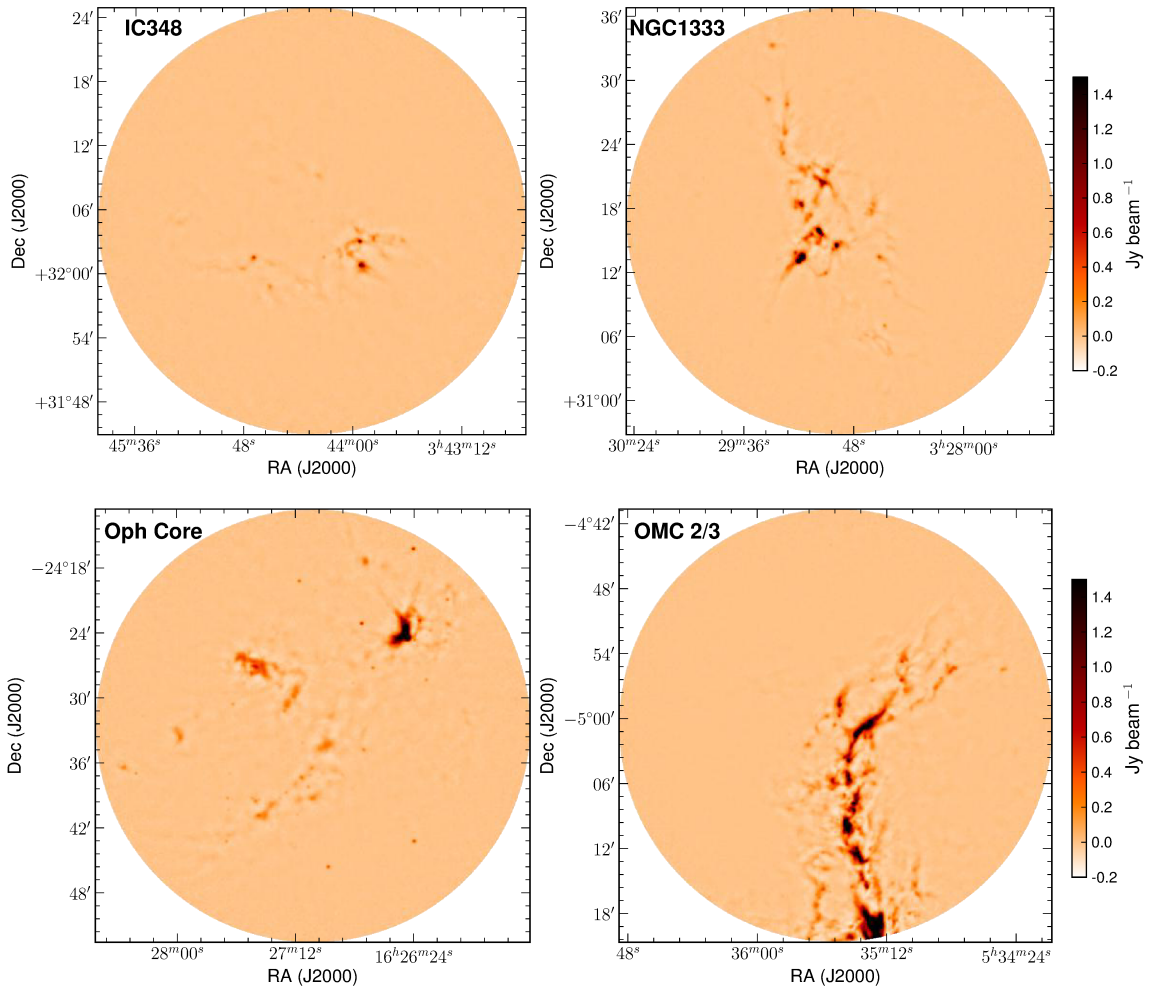


Figure 3.1: Four of the Transient fields. All data taken between December 22nd, 2015 and September 29th, 2016 has been co-added to produce these images. The images are presented with the same colour scale.

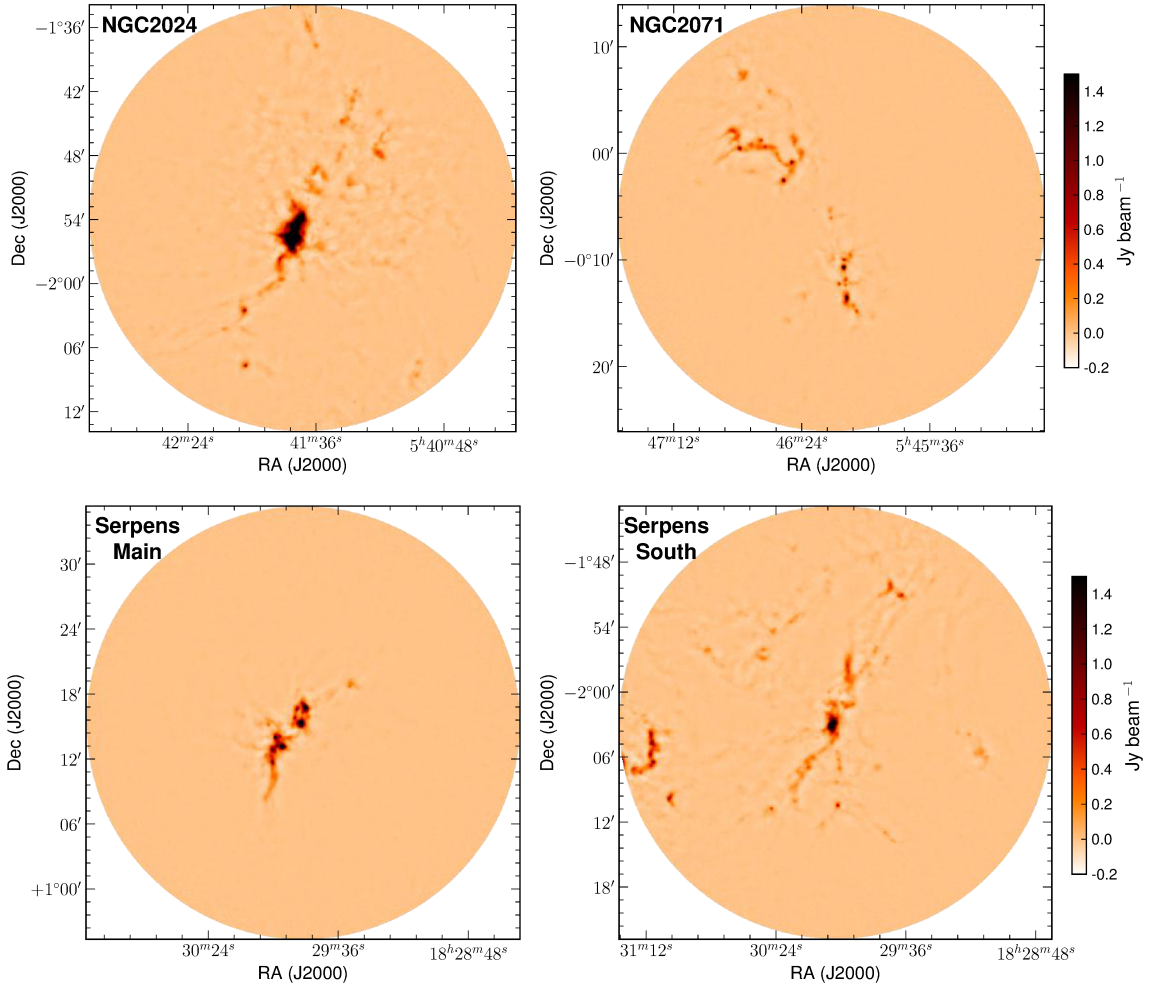


Figure 3.2: Four of the Transient fields. All data taken between December 22nd, 2015 and September 29th, 2016 has been co-added to produce these images. The images are presented with the same colour scale.

Table 3.1: A summary of the observed JCMT Transient Survey regions between the first observations on December 22nd, 2015 and September 29th, 2016.

Region	Central RA (J2000)	Central DEC (J2000)	Number of Epochs	Average 850 μm Noise ^{a,b} (mJy beam ⁻¹)	Std. Dev. 850 μm Noise ^c (mJy beam ⁻¹)
Perseus: NGC1333	03:28:54	+31:16:52	7	12.26	0.40
Perseus: IC348	03:44:18	+32:04:59	7	12.18	0.43
Orion: OMC 2/3	05:35:33	-05:00:32	7	11.72	0.54
Orion: NGC2024	05:41:41	-01:53:51	8	11.29	0.40
Orion: NGC2071	05:46:13	+00:06:05	7	11.75	0.38
Ophiuchus: Core	16:27:05	-24:32:37	7	13.35	0.75
Serpens: Main	18:29:49	+01:15:20	8	12.01	0.27
Serpens: South	18:30:02	-02:02:48	8	14.56	1.18

^aThese measurements of the 850 μm noise levels are based on a point source detection in a single observation using 3'' pixels and a 14.6'' FWHM beam.

^bThe reduction method *R3* was used to derive these noise estimates (see § 3.3).

^cThe standard deviation of the average 850 μm noise across all epochs.

(pixels with a signal-to-noise ratio of at least 3 are generally deemed significant for the Transient Survey). This mask is then used in a second round of data reduction in order to recover better any faint and extended structure.

The Transient Survey performs four individual data reductions labeled *R1*, *R2*, *R3*, and *R4* (Mairs et al. in preparation), yielding four sets of maps exhibiting different models of the recovered, astronomical structure.

1. *R1*: An effective spatial filter of 200'' was applied and no external mask was used.
2. *R2*: An effective spatial filter of 600'' was applied and no external mask was used.
3. *R3*: An external mask was constructed from a co-add of the *R1* reduction and was used to constrain the solution derived by *makemap*. Thus, the structure was filtered to 200''.

4. R_4 : Similarly to R_3 , an external mask was constructed from a co-add of the R_2 reduction and applied to the data. Thus, the structure was filtered to $600''$.

Figure 3.3 shows an example of a single observation of the Ophiuchus Core region (see Table 3.1). The top two panels show the resulting maps produced by reductions R_3 (left) and R_4 (right) while the bottom two panels show the subtraction of the R_3 image from the R_4 image (left) to highlight the effect of changing the effective spatial filter and the subtraction of the R_2 image from the R_4 image to highlight the effect of the external mask. Clearly, though more extended structure is present in the R_2 and R_4 maps, the compact structure is recovered whether a $200''$ or a $600''$ filter is used. As well, for the extended emission reconstructions, the mask returns additional flux some of which appears point-like. As [52] discuss, the amount of extended structure which is recovered can produce slightly different results for the compact structure present in the map as the larger-scale background may add an additional base value to the flux. This, however, is of little concern for the detection of variability since the Transient Survey is only searching for relative changes in brightness and, therefore, as long as a consistent data reduction procedure is used, the results will be robust.

The dominant uncertainty between these different reduction methods is how the recovered extended structure and external masks alter how compact emission sources are fit with models. The measurement of the peak brightness of a source relies on a consistent procedure from observation to observation in conjunction with the optimal data reduction method. By fitting Gaussian profiles to compact emission sources and comparing their centroid positions and peak brightnesses, the Transient Survey determine reduction R_3 to be the most stable (Mairs et al. in preparation). The external mask limits the flux distribution during the map-making procedure while the harsher filter removes large-scale structure, which is not expected to vary (but is hard to recover due to signal from the atmosphere and the instrumentation).

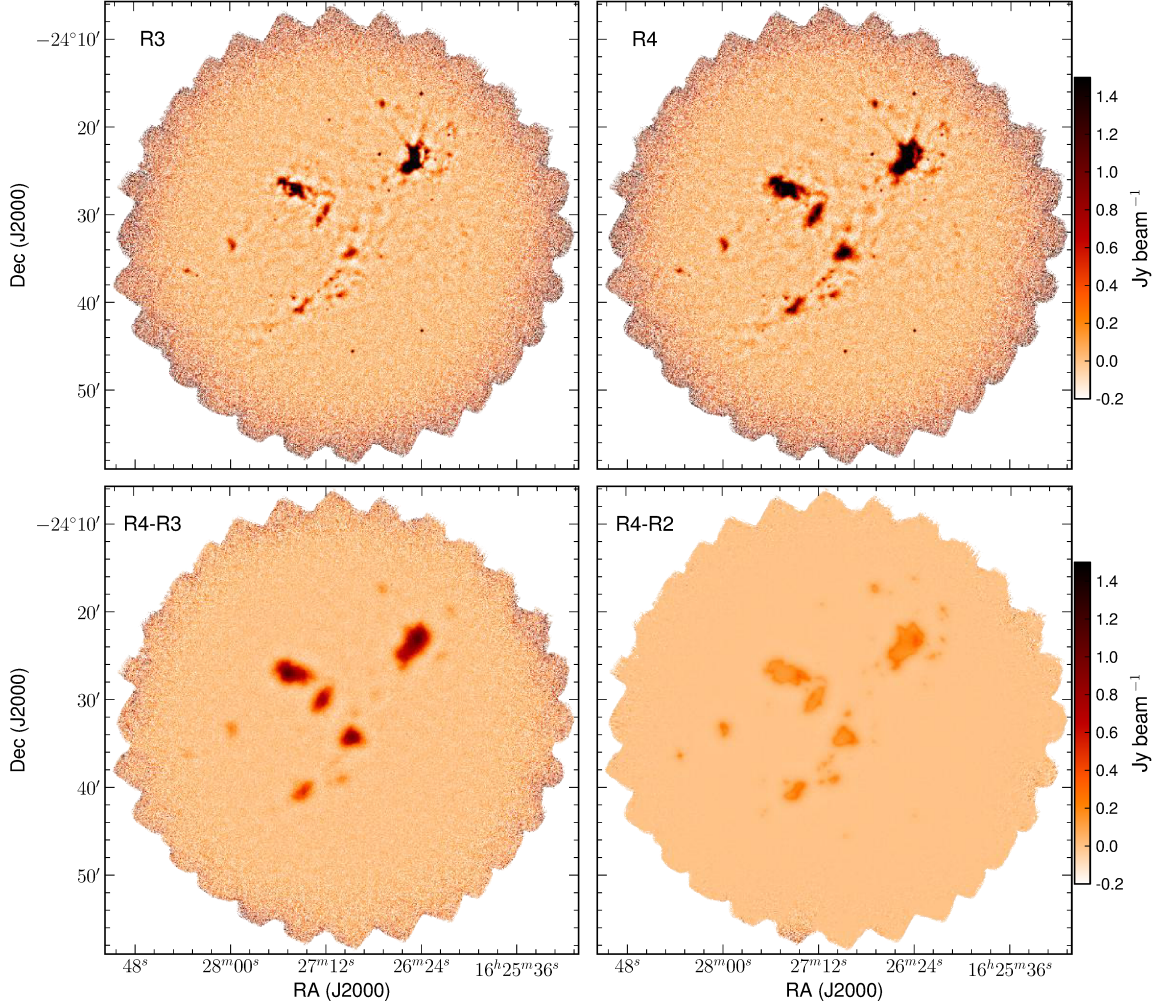


Figure 3.3: **Top:** A single observation of the Ophiuchus Core region reduced using reduction methods $R3$ (left) and $R4$ (right). **Bottom:** Reduction $R4$ minus reduction $R3$ (left) and reduction $R4$ minus reduction $R2$ (right).

3.4 Image Alignment

Since the JCMT Transient Survey is interested in measuring the peak brightness of individual compact sources over time, it is important to take into consideration the pointing uncertainty of the telescope (expected to be 2 to 6 arcseconds; EAO staff *private communication*). I perform a post-reduction calibration where I derive and apply a pointing correction to more precisely align the maps with one another in order to then in future derive and apply a relative flux calibration factor for each image produced in order to consistently compare a given source from observation

to observation. This calibration is a relative correction for each region, thus I can use the most robust, compact emission sources present in each map to calibrate self-consistently.

3.4.1 The GAUSSCLUMPS Method

In this thesis I am comparing my work to the current post-reduction image alignment methods the JCMT Transient Survey are currently using (Mairs et al. in preparation). The Transient Survey has tried a variety of publicly available algorithm designed to extract structure from a given region, (e.g. GAUSSCLUMPS [83], CLUMPFIND [92], ASTRODENDRO [66], GETSOURCES [56], and FELLWALKER [6]). Each method, however, combines detected emission differently based on user supplied criteria and, thus, the use of such algorithms requires discernment and a goal-based approach. In this work, we are interested in accurately determining the brightnesses of localised, compact sources in dust emission convolved with the JCMT beam, which we expect to have approximately Gaussian features [20]. Therefore, the Transient team has selected the algorithm GAUSSCLUMPS [83] to identify and extract sources in each observation of a given field, as this program is designed to robustly characterise Gaussian structure and subtract background structure. Specifically, they use the STARLINK software [18] implementation of GAUSSCLUMPS found within the CUPID [7] package.

GAUSSCLUMPS [83] identifies first the brightest peak in a user-supplied map and fits a Gaussian to the surrounding structure with a least-squares method. If the structure is deemed to be real (i.e. not a spurious detection of a noise spike, a test which is based on a series of user-defined parameters), the fit is subtracted from the data and the algorithm iteratively identifies and fits a Gaussian to the next brightest peak until all of the significant structure is identified. The algorithm is designed to weight the Gaussian fits to smaller-scale structures (at least the size of the instrument beam) such that locally peaked objects are preferred over underlying, larger-scale features. Identified sources are allowed to overlap.

3.4.2 The Cross Correlation Method

As an alternative approach to calibrating the image alignment I present a method based on cross correlation between epochs. As mentioned in § 3.2, each region is imaged approximately once a month. These snapshots in time are referred to as epochs. In this section I present results from the *R1* 850 μm reductions, however this Cross Correlation method has proven to be successful for all four of the 850 μm reductions (Mairs et al. in preparation).

The Cross Correlation method computes the cross correlation between a reference epoch to each succeeding science epoch:

$$\text{cor}(\text{RA}, \text{DEC}) = \sum_{\text{pixels}_x} \sum_{\text{pixels}_y} \mathcal{R}(x, y) \times \mathcal{S}(x - \text{RA}, y - \text{DEC}) \quad (3.1)$$

where \mathcal{R} is a reference epoch map, which we choose to be the first epoch from each region, \mathcal{S} is a succeeding science epoch map to be aligned, and both maps have identical dimensions. The cross correlation of a reference epoch to a science epoch is the measure of how similar the two maps are as a function of the displacement of the science map relative to the reference map. If the two maps were identical and there were zero offset, then the measure of the cross correlation would be an auto correlation, where the peak $\text{max}(\text{cor}(\text{RA}, \text{DEC}))$ resides at $(\text{RA}, \text{DEC}) = (0, 0)$. The measured radial offset between the reference map and the science map is:

$$\text{Radial offset} = \sqrt{(\Delta\text{RA})^2 + (\Delta\text{DEC})^2} \quad (3.2)$$

where ΔRA and ΔDEC are the angular offsets between $\text{max}(\text{cor}(\text{RA}, \text{DEC}))$ and $(\text{RA}, \text{DEC}) = (0, 0)$ in the right ascension and declination.

To determine the position of $\text{max}(\text{cor}(\text{RA}, \text{DEC}))$ a non-linear least squares regression is used to fit a 2D Gaussian to the inner 5×5 px² area, equivalent to a 15'' beam at 850 μm ([20]) surrounding the most correlated pixel (e.g. Figure 3.4).

The Cross Correlation method is advantageous to the GAUSSCLUMPS method as the GAUSSCLUMPS method considers a flux-limited sample, where it uses a list of

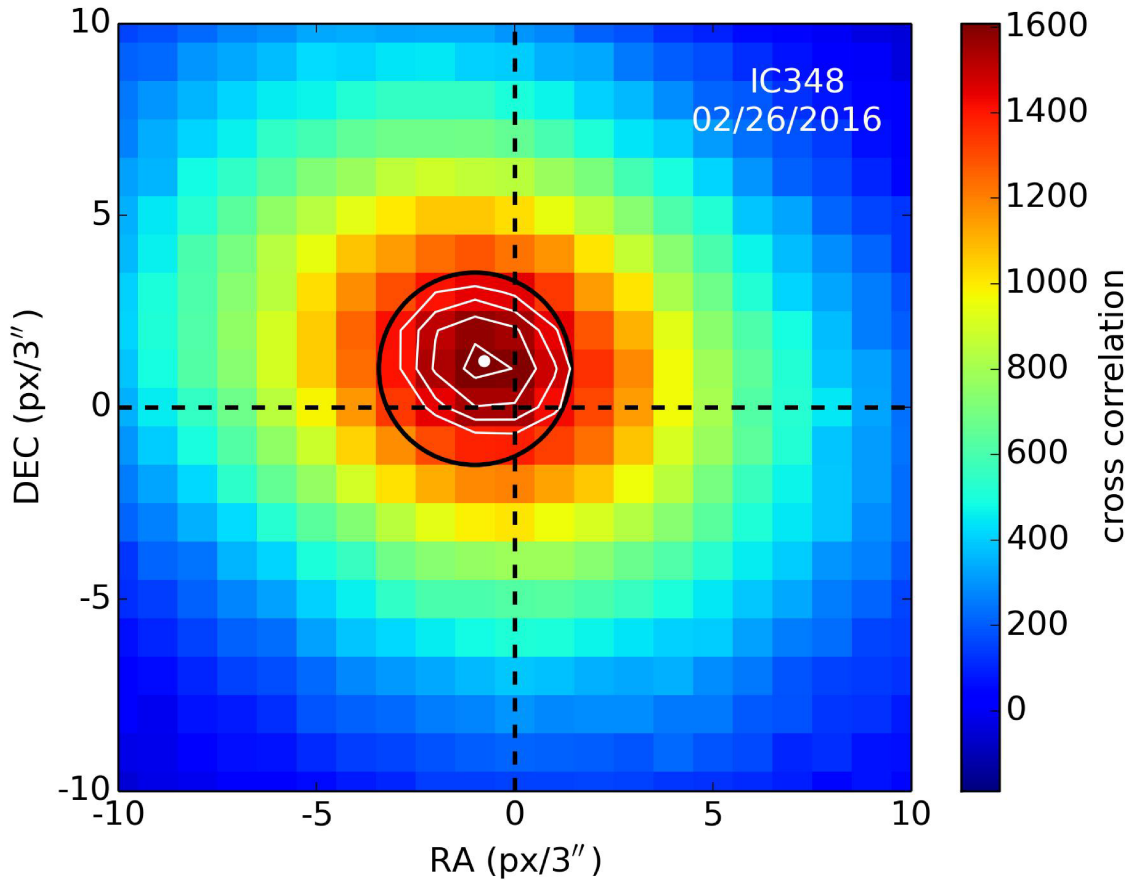


Figure 3.4: An example cross correlation of the IC348 region on 02/26/2016 for an $R1$ reduction at $850 \mu\text{m}$. The black circle represents an effective $15''$ beam, the white contours represent the 2D Gaussian fit to the data, the white filled circle represents the maximum of the fit, and the dashed black lines represent the zero offset position.

bright compact small-scale structures, for which there could only be a handful in some cases (e.g. IC348). Comparatively, the Cross Correlation method takes in consideration the entire map, including fainter large-scale structures possibly missed by GAUSSCLUMPS. The GAUSSCLUMPS algorithm is also based on a series of user-defined parameters, allowing a large set of variables to be altered, giving it a higher chance of false positives. The only parameter in the Cross Correlation method is the 2D Gaussian fit, which GAUSSCLUMPS does as well.

3.5 Results

Positional offsets are measured for a total of $N = 51$ science epochs over all eight regions, and the median offset is 3.41 ± 1.74 arcsec, comparable to what is found using the GAUSSCLUMPS method (Mairs et al. in preparation). Subsequently, each science epoch is re-reduced with *makemap* with an applied offset relative to its reference map. Then, same correlation and fitting method as described in § 3.4.2 is applied to the original data to the aligned maps. Next, the algorithm measures a residual offsets between the reference maps and the aligned maps. The median residual offset after alignment is $0.03_{-0.02}^{+0.03}$ arcsec. This alignment is $100\times$ smaller than a the pixel size at $850 \mu\text{m}$, and a factor of $\sim 80\times$ better aligned than the telescope’s pointing error (EAO staff *private communication*). The uncertainty median residual offset is a measure of a standard deviation from the median (see Figure 3.5).

Using the GAUSSCLUMPS method, the Transient Survey has found a comparable offsets distribution for the unaligned maps, however their median residual offsets after alignment is $\sim 0.6''$ (Mairs et al. in preparation). The Cross Correlation method is able to align maps to a $\sim 20\times$ finer scale than the Transient Survey’s current method.

Figure 3.5 shows the results of applying the post-reduction alignment to the JCMT Transient Survey observations using reduction *R1* (all four reduction methods tested show consistent results, see Mairs et al. in preparation). The black histograms show the original pointing error (note that the absolute pointing error with respect to a central reference never exceeds $\sim 4-5''$), while the blue histograms show the corrected pointing error. Although both methods result in comparable offset distributions before alignment, the offsets for each specific epoch are more correctly derived from the Cross Correlation method.

3.6 Discussion

Although the median offset is $0.03_{-0.02}^{+0.03}$ arcsec, the uncertainty in the residual offset is limited by the uncertainty in the 2D Gaussian fit to the cross correlation. As show in the bottom panel of Figure 3.6, the median offset uncertainty is ~ 0.03 arcsec,

which is limited by the large spread of the cross correlation product (see Figure 3.4). Therefore, this image alignment method is limited to a single iteration of the Cross Correlation method, as it will not improve on it self with succeeding iterations.

There don't seem to be any correlations between measured residual offset and maximum cross correlation value, nor any biases due to the fitting algorithm (see Figure 3.6). The larger the peak cross correlation value the more bright compact small scale structure resides within the region, as there is less weather dependant variable large-scale structure, which would lower the correlation between epochs. The top panel of Figure 3.6 shows offset and offset uncertainty as functions of peak cross correlation value, and it is clear that as large-scale structure begins to become prevalent the measure offset does not become any more uncertain. While using GAUSSCLUMPS, the Transient Survey finds their data exhibit a higher uncertainty in fitting the NGC2024 region, which contains more clustered sources mixed with larger-scale structure (Mairs et al. in preparation). Isolated, bright emission sources have less fitting uncertainties in GAUSSCLUMPS ([83]) and therefore produce the best alignments for the Transient Survey's current data. Namely, the GAUSSCLUMPS method is biased towards having more accurate alignments for fields with compact bright sources embedded within small-scale structure, whereas the Cross Correlation method is found to be unbiased towards fields with either small-scale or large-scale structure.

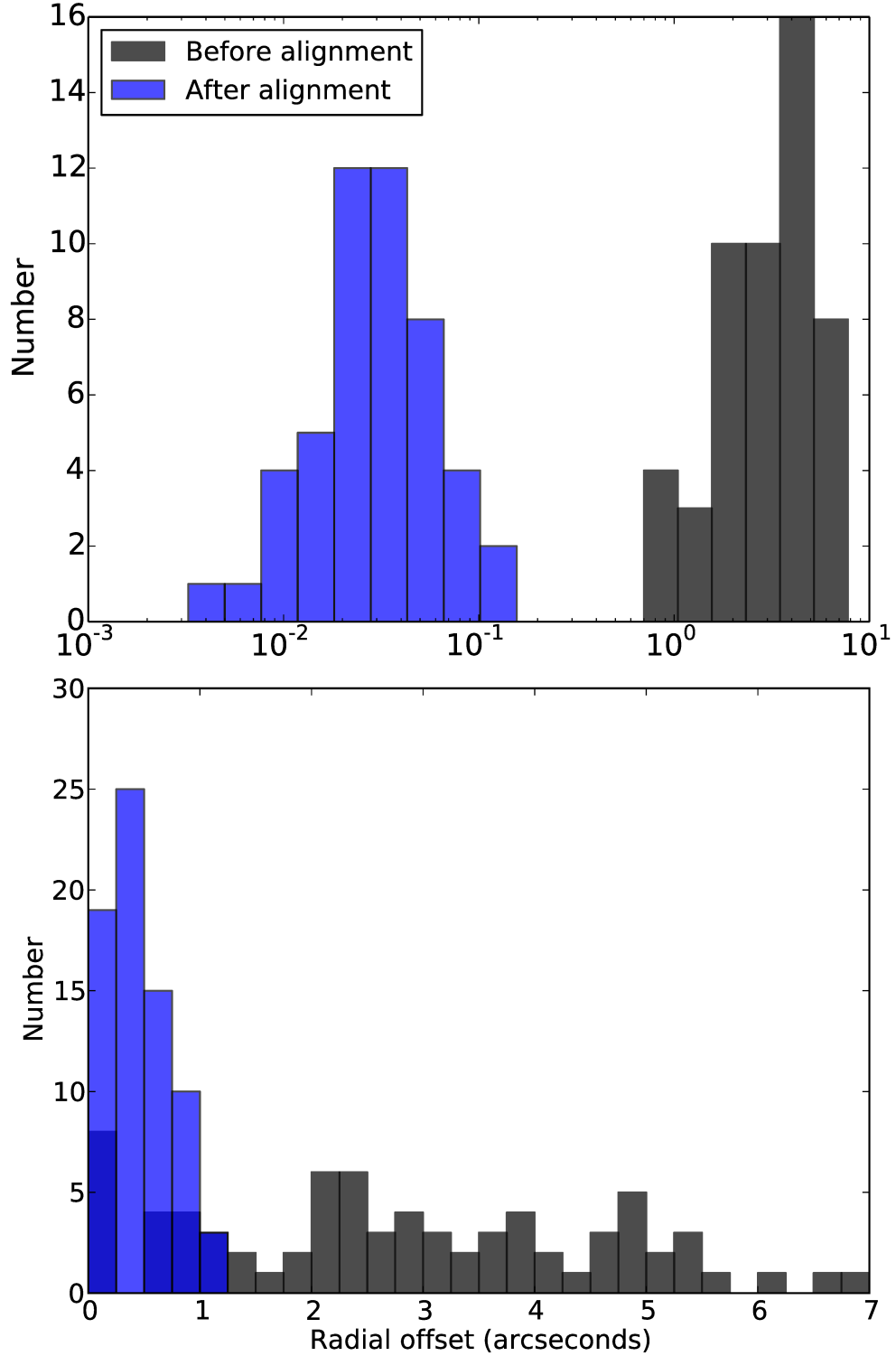


Figure 3.5: **Top:** The Cross Correlation method. **Bottom:** The GAUSSCLUMPS method (Mairs et al. in preparation). Distributions of the measured radial offset between each region’s reference field and its subsequent observations. The black distributions represent the original offsets before alignment, and the blue distributions represent the residual offsets of the aligned maps.

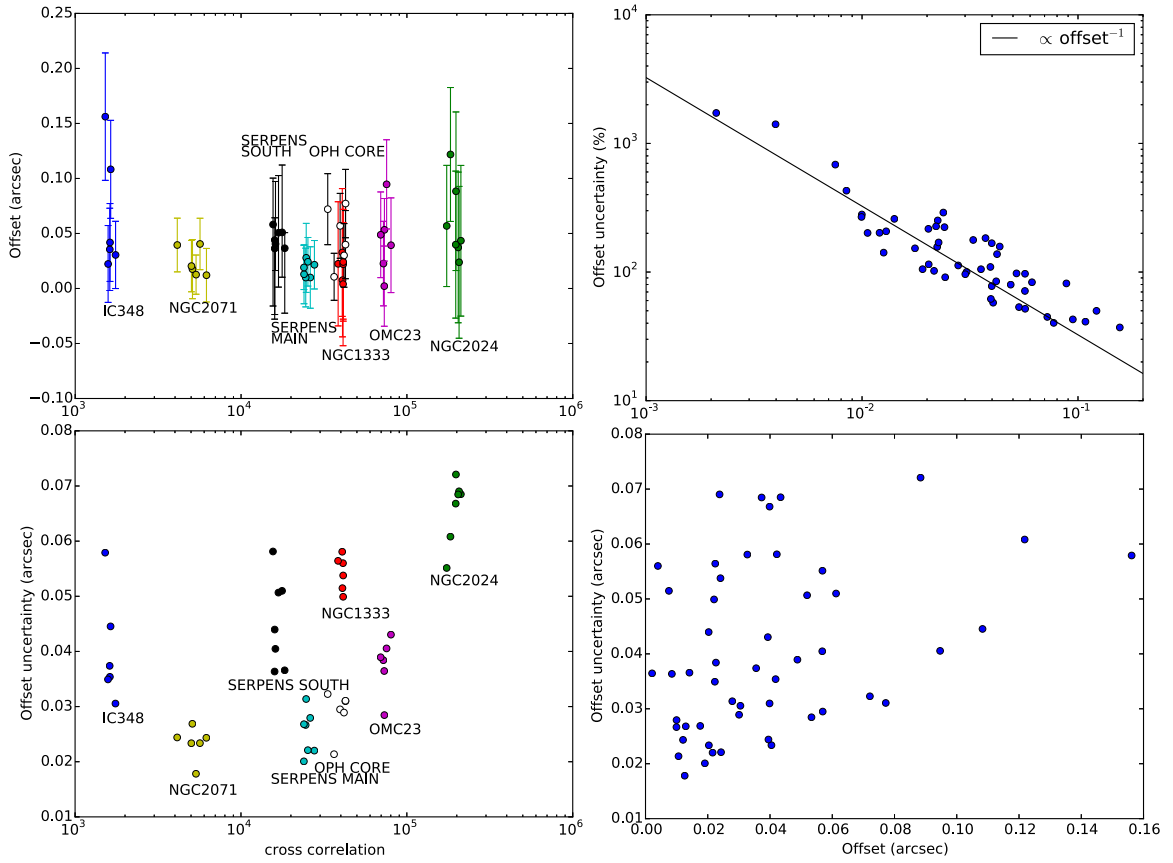


Figure 3.6: **Left:** Offset and offset uncertainty as functions of maximum cross correlation value for aligned maps. **Right:** Offset uncertainty as a function of offset for aligned maps.

Figure 3.7 shows measured offsets in right ascension in each of the four reduction methods ($R1$, $R2$, $R3$, and $R4$) as a function of right ascension offset in $R3$ (and same for declination). The vertical axes are 1 pixel large in either direction from zero. This figure is used to distinguish between observations and to show that the reliability of the alignment is independent of the original pointing error at the telescope. This figure also shows that the difference in offsets between reduction methods is much smaller for the Cross Correlation method than for the GAUSSCLUMPS method, thus showing that the Cross Correlation method is more reliable between the four reductions compared to the GAUSSCLUMPS method. Quantitatively, the Cross Correlation method has a standard deviation of $\sim 0.1''$ between reductions, whereas the GAUSSCLUMPS method results in a $\sim 1''$ standard deviation between reduction methods.

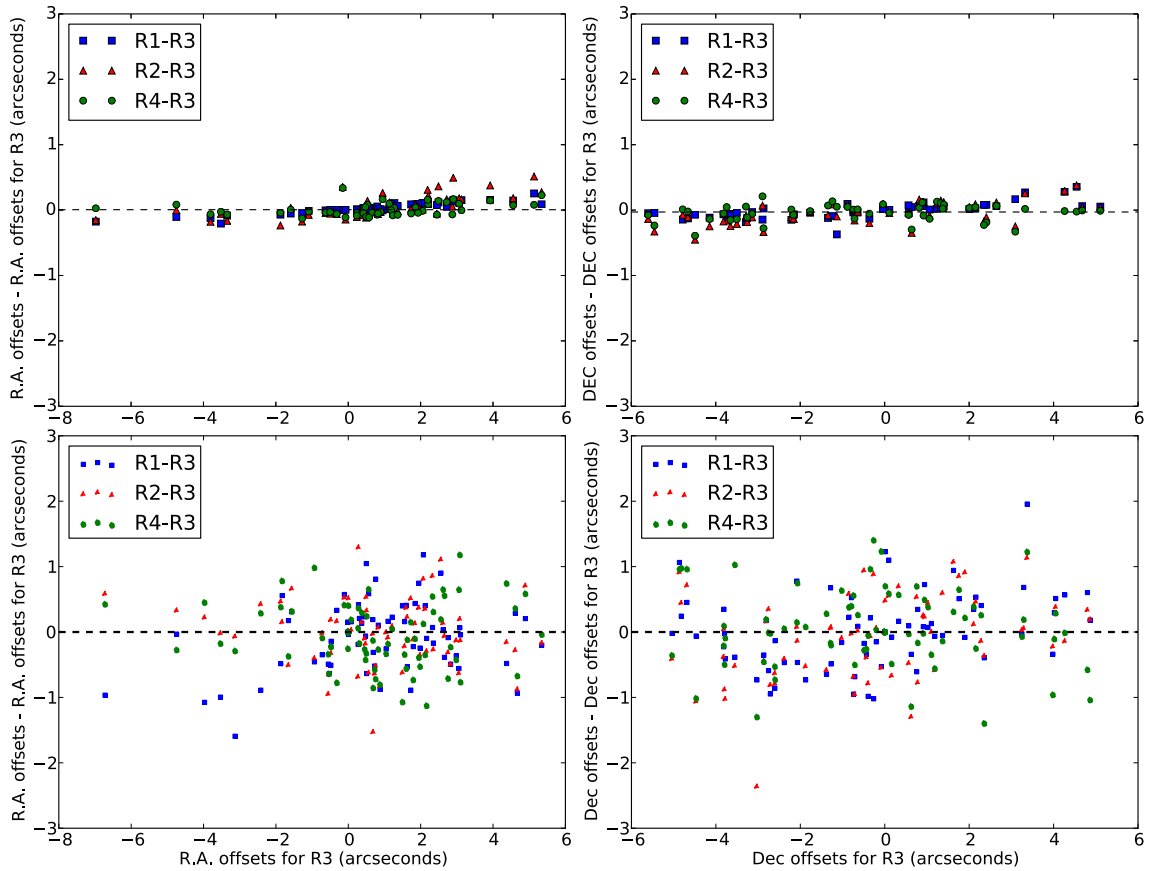


Figure 3.7: **Top:** The Cross Correlation (C.C.) method. **Bottom:** The GAUSSCLUMPS (G.C.) method, courtesy of Mairs et al. in preparation. **Left:** The derived right ascension offsets measured in each of the four reductions compared to reduction $R3$. **Right:** Same as the left, but showing the declination offsets.

3.7 Conclusions

The JCMT Transient Survey’s main goal is to detect variability in the brightness of deeply embedded protostars. The pointing accuracy of the JCMT is nominally 2 to 6 arcseconds, and in order to dramatically increase our sensitivity to variable signals, I have developed a calibration pipeline which further spatially aligns multiple observations of a given field, which provides the survey team with reliable maps to measure flux variability. I use a cross correlation algorithm to align the maps and compare the the Transient Survey’s current `Gaussclumps` method. The Cross Correlation method could be applied to any astronomical data with multiple observations of bright, compact objects, residing within large- or small-scale structure. My main results can be summarised as follows:

1. The JCMT Transient Survey thoroughly tested four different data reduction methods and found the most robust parameters for the scientific goals (Mairs et al. in preparation).
2. The Cross Correlation method is able to align maps reliably and achieve ~ 0.03 arcsec in residual offsets ($100\times$ smaller than a single pixel), improving on the survey’s current `Gaussclumps` method by a factor of $\sim 20\times$, and improving on the telescope’s pointing error by a factor of $\sim 80\times$.
3. The Cross Correlation method does not show any biases towards different types of structure or sources within regions, eliminating the biases found by the Transient Survey’s current methods.
4. The Cross Correlation method works independent from the original pointing error from the telescope. Additionally, this method has proven to be exceptionally reliable between all four reduction methods, and a factor of $10\times$ more reliable than the surveys’s current methods.

The JCMT Transient Survey will continue through at least December, 2018. Throughout this time, we will be working to improve the data reduction and calibration procedures in order to detect fainter signals and working to achieve similar results for the image alignment at $450\ \mu\text{m}$. Together, we will work to integrate the Cross Correlation method for the next data release, which will provide scientists with the opportunity to have more accurate and precise flux calibration factors. By the end of the survey, we will have the deepest sub-millimetre maps of these eight regions, which will create many opportunities for additional science, including co-adding across several epochs to reach fainter sources, but with a lower cadence.

Chapter 4

Conclusion

4.1 Chapter 2: A SCUBA-2 Survey for Luminous Far-Infrared Galaxies in Protoclusters at $z > 2$

The brightest high-redshift sub-millimetre galaxies (SMGs) represent the rarest and most extreme star-forming events in the Universe and are thought to be the progenitors to some of the most massive local galaxies. While short-lived, these SMGs contain intense stellar nurseries, which greatly affect the Universe's evolution, and are found in protoclusters, the progenitors of the most massive local galaxy clusters. In this chapter I presented a sub-millimetre study of two high-redshift protoclusters in attempt to understand how galaxy assembly is accelerated in over-dense environments in the early Universe.

4.2 Chapter 3: The JCMT Transient Survey: Data Reduction and Calibration Methods

The evolution of the mass accretion rate remains largely unconstrained for the early stages of low-mass star formation. Examining the variation in the rate at which mass is accreted onto the central protostar is critical to understanding the physics of star formation. In this chapter I presented The JCMT Transient Survey's data reduction techniques and proposed an improvement on their post-calibration image alignment methods.

Bibliography

- [1] P. André, J. Di Francesco, D. Ward-Thompson, S.-I. Inutsuka, R. E. Pudritz, and J. E. Pineda. From Filamentary Networks to Dense Cores in Molecular Clouds: Toward a New Paradigm for Star Formation. *Protostars and Planets VI*, pages 27–51, 2014.
- [2] M. Aravena, C. L. Carilli, M. Salvato, M. Tanaka, L. Lentati, E. Schinnerer, F. Walter, D. Riechers, V. Smolcic, P. Capak, H. Aussel, F. Bertoldi, S. C. Chapman, D. Farrah, A. Finoguenov, E. Le Floch, D. Lutz, G. Magdis, S. Oliver, L. Riguccini, S. Berta, B. Magnelli, and F. Pozzi. Deep observations of CO line emission from star-forming galaxies in a cluster candidate at $z=1.5$. *Monthly Notices of the Royal Astronomical Society, Volume 426, Issue 1, pp. 258-275.*, 426:258–275, July 2012.
- [3] J. Bae, L. Hartmann, Z. Zhu, and R. P. Nelson. Accretion Outbursts in Self-gravitating Protoplanetary Disks. *ApJ*, 795:61, November 2014.
- [4] A. J. Barger, L. L. Cowie, C.-C. Chen, F. N. Owen, W.-H. Wang, C. M. Casey, N. Lee, D. B. Sanders, and J. P. Williams. Is There a Maximum Star Formation Rate in High-Redshift Galaxies? *The Astrophysical Journal*, 784(1):9, January 2014.
- [5] P. Barmby, J.S. Huang, G. G Fazio, J. A. Surace, R. G. Arendt, J. L. Hora, M. A. Pahre, K. L. Adelberger, P. Eisenhardt, D. K. Erb, M. Pettini, W. T. Reach, N. A. Reddy, A. E. Shapley, C. C. Steidel, D. Stern, Z. Wang, and S. P. Willner. Deep MidInfrared Observations of Lyman Break Galaxies. *The Astrophysical Journal Supplement Series*, 154(1):97–102, May 2004.
- [6] D. S. Berry. FellWalker-A clump identification algorithm. *Astronomy and Computing*, 10:22–31, April 2015.
- [7] D. S. Berry, K. Reinhold, T. Jenness, and F. Economou. CUPID: A Clump Identification and Analysis Package. In R. A. Shaw, F. Hill, and D. J. Bell, editors, *Astronomical Data Analysis Software and Systems XVI*, volume 376 of *Astronomical Society of the Pacific Conference Series*, page 425, October 2007.
- [8] Andrew W. Blain, Ian Smail, R. J. Ivison, J. P. Kneib, and David T. Frayer. Submillimeter galaxies. *Physics Report*, 369(2):111–176, February 2002.
- [9] C. M. Casey, A. Cooray, P. Capak, H. Fu, K. Kovac, S. Lilly, D. B. Sanders, N. Z. Scoville, and E. Treister. A massive, distant proto-cluster at $z=2.47$ caught in a phase of rapid formation? *The Astrophysical Journal Letters, Volume 808, Issue 2, article id. L33, 8 pp. (2015).*, 1002:4–10, June 2015.

- [10] Caitlin M. Casey, Desika Narayanan, and Asantha Cooray. Dusty star-forming galaxies at high redshift. *Physics Reports*, 541(2):45–161, February 2014.
- [11] Edward L. Chapin, David S. Berry, Andrew G. Gibb, Tim Jenness, Douglas Scott, Remo P. J. Tilanus, Frossie Economou, and Wayne S. Holland. SCUBA-2: iterative map-making with the Sub-Millimetre User Reduction Facility. *Monthly Notices of the Royal Astronomical Society, Volume 430, Issue 4, p.2545-2573*, 430:2545–2573, January 2013.
- [12] Edward L. Chapin, Alexandra Pope, Douglas Scott, Itziar Aretxaga, Jason E. Austermann, Ranga Ram Chary, Kristen Coppin, Mark Halpern, David H. Hughes, James D. Lowenthal, Glenn E. Morrison, Thushara A. Perera, Kimberly S. Scott, Grant W. Wilson, and Min S. Yun. An AzTEC 1.1 mm survey of the GOODS-N field - II. Multiwavelength identifications and redshift distribution. *Monthly Notices of the Royal Astronomical Society*, 398(4):1793–1808, June 2009.
- [13] S. C. Chapman, F. Bertoldi, Ian Smail, A. W. Blain, J. E. Geach, M. Gurwell, R. J. Ivison, G. R. Petitpas, N. Reddy, and C. C. Steidel. A blind CO detection of a Distant Red Galaxy in the HS1700+64 proto-cluster. *Monthly Notices of the Royal Astronomical Society: Letters, Volume 449, Issue 1, p.L68-L72*, 449:L68–L72, January 2015.
- [14] S. C. Chapman, A. Blain, R. Ibata, R. J. Ivison, Ian Smail, and G. Morrison. Do submillimetre galaxies really trace the most massive dark-matter halos? Discovery of a high- z cluster in a highly active phase of evolution. *The Astrophysical Journal*, 691(1):560–568, September 2009.
- [15] S. C. Chapman, A. W. Blain, Ian Smail, and R. J. Ivison. A Redshift Survey of the Submillimeter Galaxy Population. *The Astrophysical Journal*, 622(2):772–796, December 2005.
- [16] Chian-Chou Chen, Lennox L. Cowie, Amy J. Barger, Caitlin M. Casey, Nicholas Lee, David B. Sanders, Wei-Hao Wang, and Jonathan P. Williams. Faint submillimeter galaxy counts at 450 μm . *The Astrophysical Journal*, 762(2):81, September 2013.
- [17] K. Coppin, E. L. Chapin, A. M. J. Mortier, S. E. Scott, C. Borys, J. S. Dunlop, M. Halpern, D. H. Hughes, A. Pope, D. Scott, S. Serjeant, J. Wagg, D. M. Alexander, O. Almaini, I. Aretxaga, T. Babbedge, P. N. Best, A. Blain, S. Chapman, D. L. Clements, M. Crawford, L. Dunne, S. A. Eales, A. C. Edge, D. Farrah, E. Gaztanaga, W. K. Gear, G. L. Granato, T. R. Greve, M. Fox, R. J. Ivison, M. J. Jarvis, T. Jenness, C. Lacey, K. Lepage, R. G. Mann, G. Marsden, A. Martinez-Sansigre, S. Oliver, M. J. Page, J. A. Peacock, C. P. Pearson, W. J. Percival, R. S. Priddey, S. Rawlings, M. Rowan-Robinson, R. S. Savage, M. Seigar, K. Sekiguchi, L. Silva, C. Simpson, I. Smail, J. A. Stevens, T. Takagi,

- M. Vaccari, E. van Kampen, and C. J. Willott. The SCUBA Half Degree Extragalactic Survey (SHADES) – II. Submillimetre maps, catalogue and number counts. *Monthly Notices of the Royal Astronomical Society, Volume 372, Issue 4*, pp. 1621-1652., 372:1621–1652, September 2006.
- [18] M. J. Currie, D. S. Berry, T. Jenness, A. G. Gibb, G. S. Bell, and P. W. Draper. Starlink Software in 2013. In N. Manset and P. Forshay, editors, *Astronomical Data Analysis Software and Systems XXIII*, volume 485 of *Astronomical Society of the Pacific Conference Series*, page 391, May 2014.
- [19] H. Dannerbauer, J. D. Kurk, C. De Breuck, D. Wylezalek, J. S. Santos, Y. Koyama, N. Seymour, M. Tanaka, N. Hatch, B. Altieri, D. Coia, A. Galametz, T. Kodama, G. Miley, H. Röttgering, M. Sanchez-Portal, I. Valtchanov, B. Venemans, and B. Ziegler. An excess of dusty starbursts related to the Spiderweb galaxy. *Astronomy & Astrophysics*, 570:A55, October 2014.
- [20] Jessica T. Dempsey, Per Friberg, Tim Jenness, Remo P. J. Tilanus, Holly S. Thomas, Wayne S. Holland, Dan Bintley, David S. Berry, Edward L. Chapin, Antonio Chrysostomou, Gary R. Davis, Andrew G. Gibb, Harriet Parsons, and E. Ian Robson. SCUBA-2: on-sky calibration using submillimetre standard sources. *Monthly Notices of the Royal Astronomical Society, Volume 430, Issue 4*, p.2534-2544, 430:2534–2544, January 2013.
- [21] Jessica T. Dempsey, Wayne S. Holland, Antonio Chrysostomou, David S. Berry, Daniel Bintley, Edward L. Chapin, Simon C. Craig, Iain M. Coulson, Gary R. Davis, Per Friberg, Tim Jenness, Andy G. Gibb, Harriet A. L. Parsons, Douglas Scott, Holly S. Thomas, Remo P. J. Tilanus, Ian Robson, and Craig A. Walther. A new era of wide-field submillimetre imaging: on-sky performance of SCUBA-2. *Millimeter, Submillimeter, and Far-Infrared Detectors and Instrumentation for Astronomy VI. Proceedings of the SPIE, Volume 8452, article id. 845202, 18 pp. (2012).*, 8452, August 2012.
- [22] J. di Francesco, N. J. Evans, II, P. Caselli, P. C. Myers, Y. Shirley, Y. Aikawa, and M. Tafalla. An Observational Perspective of Low-Mass Dense Cores I: Internal Physical and Chemical Properties. *Protostars and Planets V*, pages 17–32, 2007.
- [23] A. J. B. Downes, J. A. Peacock, A. Savage, and D. R. Carrie. The Parkes selected regions - Powerful radio galaxies and quasars at high redshifts. *Monthly Notices of the Royal Astronomical Society (ISSN 0035-8711)*, 218(1):31–62, January 1986.
- [24] M. M. Dunham, L. E. Allen, N. J. Evans, II, H. Broekhoven-Fiene, L. A. Cieza, J. Di Francesco, R. A. Gutermuth, P. M. Harvey, J. Hatchell, A. Heiderman, T. L. Huard, D. Johnstone, J. M. Kirk, B. C. Matthews, J. F. Miller, D. E. Peterson, and K. E. Young. Young Stellar Objects in the Gould Belt. *ApJs*, 220:11, September 2015.

- [25] M. M. Dunham, H. G. Arce, L. E. Allen, N. J. Evans, II, H. Broekhoven-Fiene, N. L. Chapman, L. A. Cieza, R. A. Gutermuth, P. M. Harvey, J. Hatchell, T. L. Huard, J. M. Kirk, B. C. Matthews, B. Merín, J. F. Miller, D. E. Peterson, and L. Spezzi. The Luminosities of Protostars in the Spitzer c2d and Gould Belt Legacy Clouds. *AJ*, 145:94, April 2013.
- [26] M. M. Dunham, A. Crapsi, N. J. Evans, II, T. L. Bourke, T. L. Huard, P. C. Myers, and J. Kauffmann. Identifying the Low-Luminosity Population of Embedded Protostars in the c2d Observations of Clouds and Cores. *ApJS*, 179:249–282, November 2008.
- [27] M. M. Dunham, A. M. Stutz, L. E. Allen, N. J. Evans, II, W. J. Fischer, S. T. Megeath, P. C. Myers, S. S. R. Offner, C. A. Poteet, J. J. Tobin, and E. I. Vorobyov. The Evolution of Protostars: Insights from Ten Years of Infrared Surveys with Spitzer and Herschel. *Protostars and Planets VI*, pages 195–218, 2014.
- [28] D. Elbaz, E. Daddi, D. Le Borgne, M. Dickinson, D. M. Alexander, R-R Chary, J-L Starck, W. N. Brandt, M. Kitzbichler, E. MacDonald, M. Nonino, P. Popesso, D. Stern, and E. Vanzella. The reversal of the star formation–density relation in the distant universe. *Astronomy and Astrophysics, Volume 468, Issue 1, June II 2007*, pp.33-48, 468:33–48, March 2007.
- [29] D. Elbaz, M. Dickinson, H. S. Hwang, T. Diaz-Santos, G. Magdis, B. Magnelli, D. Le Borgne, F. Galliano, M. Pannella, P. Chanial, L. Armus, V. Charmandaris, E. Daddi, H. Aussel, P. Popesso, J. Kartaltepe, B. Altieri, I. Valtchanov, D. Coia, H. Dannerbauer, K. Dasyra, R. Leiton, J. Mazzarella, V. Buat, D. Burgarella, R. R. Chary, R. Gilli, R. J. Ivison, S. Juneau, E. LeFloc’h, D. Lutz, G. E. Morrison, J. Mullaney, E. Murphy, A. Pope, D. Scott, D. Alexander, M. Brodwin, D. Calzetti, C. Cesarsky, S. Charlot, H. Dole, P. Eisenhardt, H. C. Ferguson, N. Foerster-Schreiber, D. Frayer, M. Giavalisco, M. Huynh, A. M. Koekemoer, C. Papovich, N. Reddy, C. Surace, H. Teplitz, M. S. Yun, and G. Wilson. GOODS-Herschel: an infrared main sequence for star-forming galaxies. *Astronomy & Astrophysics, Volume 533, id.A119, 26 pp.*, 533, May 2011.
- [30] M. L. Enoch, N. J. Evans, II, A. I. Sargent, and J. Glenn. Properties of the Youngest Protostars in Perseus, Serpens, and Ophiuchus. *ApJ*, 692:973–997, February 2009.
- [31] N. J. Evans, II, M. M. Dunham, J. K. Jørgensen, M. L. Enoch, B. Merín, E. F. van Dishoeck, J. M. Alcalá, P. C. Myers, K. R. Stapelfeldt, T. L. Huard, L. E. Allen, P. M. Harvey, T. van Kempen, G. A. Blake, D. W. Koerner, L. G. Mundy, D. L. Padgett, and A. I. Sargent. The Spitzer c2d Legacy Results: Star-Formation Rates and Efficiencies; Evolution and Lifetimes. *ApJS*, 181:321–350, April 2009.

- [32] Neal J. Evans, Jeong-Eun Lee, Jonathan M. C. Rawlings, and Minh Choi. B335: A Laboratory for Astrochemistry in a Collapsing Cloud. *The Astrophysical Journal*, 626:919–932, March 2005.
- [33] J. E. Geach, J. S. Dunlop, M. Halpern, Ian Smail, P. van der Werf, D. M. Alexander, O. Almaini, I. Aretxaga, V. Arumugam, V. Asboth, M. Banerji, J. Beanlands, P. N. Best, A. W. Blain, M. Birkinshaw, E. L. Chapin, S. C. Chapman, C-C. Chen, A. Chrysostomou, C. Clarke, D. L. Clements, C. Conscience, K. E. K. Coppin, W. I. Cowley, A. L. R. Danielson, S. Eales, A. C. Edge, D. Farrah, A. Gibb, C. M. Harrison, N. K. Hine, D. Hughes, R. J. Ivison, M. Jarvis, T. Jenness, S. F. Jones, A. Karim, M. Koprowski, K. K. Knudsen, C. G. Lacey, T. Mackenzie, G. Marsden, K. McAlpine, R. McMahon, R. Meijerink, M. J. Michalowski, S. J. Oliver, M. J. Page, J. A. Peacock, D. Rigopoulou, E. I. Robson, I. Roseboom, K. Rotermond, Douglas Scott, S. Serjeant, C. Simpson, J. M. Simpson, D. J. B. Smith, M. Spaans, F. Stanley, J. A. Stevens, A. M. Swinbank, T. Targett, A. P. Thomson, E. Valiante, T. M. A. Webb, C. Willott, J. A. Zavala, and M. Zemcov. The SCUBA-2 Cosmology Legacy Survey: 850 μm maps, catalogues and number counts. *Monthly Notices of the Royal Astronomical Society*, Volume 465, Issue 2, p.1789-1806, 465(2):1789–1806, July 2017.
- [34] James E. Geach, Ian Smail, Kristen Coppin, Sean M. Moran, Alastair C. Edge, and Richard S. Ellis. CO interferometry of gas-rich spiral galaxies in the outskirts of an intermediate redshift cluster. *Monthly Notices of the Royal Astronomical Society: Letters*, Volume 395, Issue 1, pp. L62-L66., 395:L62–L66, February 2009.
- [35] Christopher C. Hayward, Dušan Kereš, Patrik Jonsson, Desika Narayanan, T. J. Cox, and Lars Hernquist. What Does a Submillimeter Galaxy Selection Actually Select? the Dependence of Submillimeter Flux Density on Star Formation Rate and Dust Mass. *The Astrophysical Journal*, 743(2):159, December 2011.
- [36] W. S. Holland, D. Bintley, E. L. Chapin, A. Chrysostomou, G. R. Davis, J. T. Dempsey, W. D. Duncan, M. Fich, P. Friberg, M. Halpern, K. D. Irwin, T. Jenness, B. D. Kelly, M. J. MacIntosh, E. I. Robson, D. Scott, P. A. R. Ade, E. Atad-Ettinger, D. S. Berry, S. C. Craig, X. Gao, A. G. Gibb, G. C. Hilton, M. I. Hollister, J. B. Kycia, D. W. Lunney, H. McGregor, D. Montgomery, W. Parkes, R. P. J. Tilanus, J. N. Ullom, C. A. Walther, A. J. Walton, A. L. Woodcraft, M. Amiri, D. Atkinson, B. Burger, T. Chuter, I. M. Coulson, W. B. Dorise, C. Dunare, F. Economou, M. D. Niemack, H. A. L. Parsons, C. D. Reintsema, B. Sibthorpe, I. Smail, R. Sudiwala, and H. S. Thomas. SCUBA-2: The 10000 pixel bolometer camera on the James Clerk Maxwell Telescope. *Monthly Notices of the Royal Astronomical Society*, Volume 430, Issue 4, p.2513-2533, 430:2513–2533, January 2013.

- [37] Andrew M. Hopkins and John F. Beacom. On the Normalization of the Cosmic Star Formation History. *The Astrophysical Journal*, 651(1):142–154, January 2006.
- [38] M. L. Humason, N. U. Mayall, and A. R. Sandage. Redshifts and magnitudes of extragalactic nebulae. *The Astronomical Journal*, 61:97–162, April 1956.
- [39] T. R. Hunter, C. L. Brogan, G. MacLeod, C. J. Cyganowski, C. J. Chandler, J. O. Chibueze, R. Friesen, R. Indebetouw, C. Thesner, and K. H. Young. An Extraordinary Outburst in the Massive Protostellar System NGC6334I-MM1: Quadrupling of the Millimeter Continuum. *ApJL*, 837:L29, March 2017.
- [40] R. J. Ivison, T. R. Greve, Ian Smail, J. S. Dunlop, N. D. Roche, S. E. Scott, M. J. Page, J. A. Stevens, Omar Almaini, A. W. Blain, C. J. Willott, M. J. Fox, D. G. Gilbank, Steve Serjeant, and D. H. Hughes. Deep radio imaging of the SCUBA 8-mJy survey fields: Submillimetre source identifications and redshift distribution. *Monthly Notices of the Royal Astronomical Society*, 337(1):1–25, June 2002.
- [41] Tim Jenness, Edward L. Chapin, David S. Berry, Andy G. Gibb, Remo P. J. Tilanus, Jennifer Balfour, Vincent Tilanus, and Malcolm J. Currie. SMURF: SubMillimeter User Reduction Facility. *Astrophysics Source Code Library*, 2013.
- [42] D. Johnstone, B. Hendricks, G. J. Herczeg, and S. Bruderer. Continuum Variability of Deeply Embedded Protostars as a Probe of Envelope Structure. *ApJ*, 765:133, March 2013.
- [43] R. Kackley, D. Scott, E. Chapin, and P. Friberg. JCMT Telescope Control System upgrades for SCUBA-2. In T. G. Phillips and J. Zmuidzinas, editors, *Proc. SPIE*, volume 7740, pages 1. SPIE, Bellingham, WA, July 2010.
- [44] Y. Kato, Y. Matsuda, Ian Smail, A. M. Swinbank, B. Hatsukade, H. Umehata, I. Tanaka, T. Saito, D. Iono, Y. Tamura, K. Kohno, D. K. Erb, B. D. Lehmer, J. E. Geach, C. C. Steidel, D. M. Alexander, T. Yamada, and T. Hayashino. Herschel protocluster survey: A search for dusty star-forming galaxies in protoclusters at $z=2-3$. *Monthly Notices of the Royal Astronomical Society, Volume 460, Issue 4, p.3861-3872*, 460:3861–3872, May 2016.
- [45] Robert C. Kennicutt. The Global Schmidt Law in Starforming Galaxies. *The Astrophysical Journal*, 498:541–552, December 1998.
- [46] S. J. Kenyon, L. W. Hartmann, K. M. Strom, and S. E. Strom. An IRAS survey of the Taurus-Auriga molecular cloud. *AJ*, 99:869–887, March 1990.
- [47] M. Koprowski, J. S. Dunlop, M. J. Michalowski, I. Roseboom, J. E. Geach, M. Cirasuolo, I. Aretxaga, R. A. A. Bowler, M. Banerji, N. Bourne, K. E. K. Coppin, S. Chapman, D. H. Hughes, T. Jenness, R. J. McLure, M. Symeonidis,

- and P. van der Werf. The SCUBA-2 Cosmology Legacy Survey: galaxies in the deep 850-micron survey, and the star-forming ‘main sequence’. *Monthly Notices of the Royal Astronomical Society, Volume 458, Issue 4, p.4321-4344*, 458:4321–4344, September 2015.
- [48] Claudia del P. Lagos, Carlton M. Baugh, Cedric G. Lacey, Andrew J. Benson, Han-Seek Kim, and Chris Power. Cosmic evolution of the atomic and molecular gas content of galaxies. *Monthly Notices of the Royal Astronomical Society, Volume 418, Issue 3, pp. 1649-1667.*, 418:1649–1667, May 2011.
- [49] A. Leger and J. L. Puget. Identification of the ‘unidentified’ IR emission features of interstellar dust? *Astronomy and astrophysics*, 137:L5–L8, 1984.
- [50] Brian Ma, Asantha Cooray, J. A. Calanog, H. Nayyeri, N. Timmons, C. Casey, M. Baes, S. Chapman, H. Dannerbauer, E. da Cunha, G. De Zotti, L. Dunne, D. Farrah, Hai Fu, J. Gonzalez-Nuevo, G. Magdis, M. J. Michałowski, I. Oteo, D. A. Riechers, D. Scott, M. W. L. Smith, L. Wang, J. Wardlow, M. Vaccari, S. Viaene, and J. D. Vieira. Spitzer imaging of strongly lensed Herschel-selected dusty star-forming galaxies. *The Astrophysical Journal*, 814(1):17, April 2015.
- [51] Piero Madau and Mark Dickinson. Cosmic Star Formation History. *Annual Review of Astronomy and Astrophysics*, 52:415–486, February 2014.
- [52] S. Mairs, D. Johnstone, H. Kirk, S. Graves, J. Buckle, S. F. Beaulieu, D. S. Berry, H. Broekhoven-Fiene, M. J. Currie, M. Fich, J. Hatchell, T. Jenness, J. C. Mottram, D. Nutter, K. Pattle, J. E. Pineda, C. Salji, J. D. Francesco, M. R. Hogerheijde, D. Ward-Thompson, and JCMT Gould Belt survey Team. The JCMT Gould Belt Survey: a quantitative comparison between SCUBA-2 data reduction methods. *MNRAS*, 454:2557–2579, December 2015.
- [53] R. E. Mason, A. Rodríguez-Ardila, Lucimara Martins, R. Riffel, O. González Martín, C. Ramos Almeida, D. Ruschel Dutra, L. C. Ho, K. Thanjavur, H. Flohic, A. Alonso-Herrero, P. Lira, R. McDermid, R. A. Riffel, R. P. Schiavon, C. Winge, M. D. Hoenig, and E. Perlman. The nuclear near-infrared spectral properties of nearby galaxies. *The Astrophysical Journal Supplement Series*, 217(1):13, March 2015.
- [54] C. F. McKee and S. R. R. Offner. The Luminosity Problem: Testing Theories of Star Formation. In J. Alves, B. G. Elmegreen, J. M. Girart, and V. Trimble, editors, *Computational Star Formation*, volume 270 of *IAU Symposium*, pages 73–80, April 2011.
- [55] S. T. Megeath, R. Gutermuth, J. Muzerolle, E. Kryukova, K. Flaherty, J. L. Hora, L. E. Allen, L. Hartmann, P. C. Myers, J. L. Pipher, J. Stauffer, E. T. Young, and G. G. Fazio. The Spitzer Space Telescope Survey of the Orion A and B Molecular Clouds. I. A Census of Dusty Young Stellar Objects and a Study of Their Mid-infrared Variability. *AJ*, 144:192, December 2012.

- [56] A. Men'shchikov, P. André, P. Didelon, F. Motte, M. Hennemann, and N. Schneider. A multi-scale, multi-wavelength source extraction method: getsources. *A&A*, 542:A81, June 2012.
- [57] Adam Muzzin, Gillian Wilson, H. K. C. Yee, David Gilbank, Henk Hoekstra, Ricardo Demarco, Michael Balogh, Pieter van Dokkum, Marijn Franx, Erica Ellingson, Amalia Hicks, Julie Nantais, Allison Noble, Mark Lacy, Chris Lidman, Alessandro Rettura, Jason Surace, and Tracy Webb. The Gemini Cluster Astrophysics Spectroscopic Survey (GCLASS): The Role of Environment and Self-Regulation in Galaxy Evolution at $z \sim 1$. *Science*, 746(2):26, December 2011.
- [58] P. C. Myers and P. J. Benson. Dense cores in dark clouds. II - NH₃ observations and star formation. In *Herbig-Haro Objects and T Tauri Stars. Revista Mexicana de Astronomia y Astrofisica*, volume 7, page 238, March 1983.
- [59] J. B. Oke and Allan Sandage. Energy Distributions, K Corrections, and the Stebbins-Whitford Effect for Giant Elliptical Galaxies. *The Astrophysical Journal*, 154:21, October 1968.
- [60] Alexandra Pope, Douglas Scott, Mark Dickinson, Ranga Ram Chary, Glenn Morrison, Colin Borys, Anna Sajina, David M. Alexander, Emanuele Daddi, David Frayer, Emily MacDonald, and Daniel Stern. The Bubble Deep Field-North SCUBA Super-map - IV. Characterizing submillimetre galaxies using deep Spitzer imaging. *Monthly Notices of the Royal Astronomical Society*, 370(3):1185–1207, May 2006.
- [61] P. Popesso, A. Biviano, G. Rodighiero, I. Baronchelli, M. Salvato, A. Saintonge, A. Finoguenov, B. Magnelli, C. Gruppioni, F. Pozzi, D. Lutz, D. Elbaz, B. Altieri, P. Andreani, H. Aussel, S. Berta, P. Capak, A. Cava, A. Cimatti, D. Coia, E. Daddi, H. Dannerbauer, M. Dickinson, K. Dasyra, D. Fadda, N. Förster Schreiber, R. Genzel, H. S. Hwang, J. Kartaltepe, O. Ilbert, E. Le Floch, R. Leiton, G. Magdis, R. Nordon, S. Patel, A. Poglitsch, L. Riguccini, M. Sanchez Portal, L. Shao, L. Tacconi, A. Tomczak, K. Tran, I. Valtchanov, N. Förster Schreiber, R. Genzel, H. S. Hwang, J. Kartaltepe, O. Ilbert, E. Le Floch, R. Leiton, G. Magdis, R. Nordon, S. Patel, A. Poglitsch, L. Riguccini, M. Sanchez Portal, L. Shao, L. Tacconi, A. Tomczak, K. Tran, and I. Valtchanov. The evolution of the star formation activity per halo mass up to redshift ~ 1.6 as seen by Herschel. *Astronomy & Astrophysics*, 537:A58, October 2012.
- [62] D. Reimers, J. Clavel, D. Groote, D. Engels, H. J. Hagen, T. Naylor, W. Wamsteker, and U. Hopp. The luminous quasar HS1700+6416 and the shape of the “big bump” below 500Å. *Astronomy & Astrophysics*, 218:71, 1989.
- [63] G. H. Rieke, A. Alonso-Herrero, B. J. Weiner, P. G. Perez-Gonzalez, M. Blaylock, J. L. Donley, D. Marcillac, and . Determining Star Formation Rates for Infrared

Galaxies. *The Astrophysical Journal*, Volume 692, Issue 1, pp. 556-573 (2009)., 692:556–573, October 2008.

- [64] Thomas P. Robitaille, Erik J. Tollerud, Perry Greenfield, Michael Droettboom, Erik Bray, Tom Aldcroft, Matt Davis, Adam Ginsburg, Adrian M. Price-Whelan, Wolfgang E. Kerzendorf, Alexander Conley, Neil Crighton, Kyle Barbary, Demitri Muna, Henry Ferguson, Frédéric Grollier, Madhura M. Parikh, Prasanth H. Nair, Hans M. Günther, Christoph Deil, Julien Woillez, Simon Conseil, Roban Kramer, James E. H. Turner, Leo Singer, Ryan Fox, Benjamin A. Weaver, Victor Zabalza, Zachary I. Edwards, K. Azalee Bostroem, D. J. Burke, Andrew R. Casey, Steven M. Crawford, Nadia Dencheva, Justin Ely, Tim Jenness, Kathleen Labrie, Pey Lian Lim, Francesco Pierfederici, Andrew Pontzen, Andy Ptak, Brian Refsdal, Mathieu Servillat, and Ole Streicher. Astropy: A community Python package for astronomy. *Astronomy & Astrophysics*, 558:A33, July 2013.
- [65] Thomas P. Robitaille and Barbara A. Whitney. the Present-Day Star Formation Rate of the Milky Way Determined From Spitzer -Detected Young Stellar Objects. *The Astrophysical Journal*, 710(1):L11–L15, January 2010.
- [66] E. W. Rosolowsky, J. E. Pineda, J. Kauffmann, and A. A. Goodman. Structural Analysis of Molecular Clouds: Dendrograms. *ApJ*, 679:1338–1351, June 2008.
- [67] Gwen C. Rudie, Charles C. Steidel, Ryan F. Trainor, Olivera Rakic, Milan Bogosavljevic, Max Pettini, Naveen Reddy, Alice E. Shapley, Dawn K. Erb, and David R. Law. The Gaseous Environment of High- z Galaxies: Precision Measurements of Neutral Hydrogen in the Circumgalactic Medium of $z \sim 2$ -3 Galaxies in the Keck Baryonic Structure Survey. *The Astrophysical Journal*, Volume 750, Issue 1, article id. 67, 32 pp. (2012)., 750, February 2012.
- [68] E. J. Safron, W. J. Fischer, S. T. Megeath, E. Furlan, A. M. Stutz, T. Stanke, N. Billot, L. M. Rebull, J. J. Tobin, B. Ali, L. E. Allen, J. Booker, D. M. Watson, and T. L. Wilson. Hops 383: an Outbursting Class 0 Protostar in Orion. *ApJL*, 800:L5, February 2015.
- [69] Marcin Sawicki. The 1.6 Micron Bump as a Photometric Redshift Indicator. *The Astronomical Journal*, 124:3050, September 2002.
- [70] N Z Scoville, J E Carlstrom, C J Chandler, J A Phillips, S L Scott, R P J Tilanus, and Z Wang. The relational database and calibration software for the Caltech millimeter array, 1993.
- [71] Alice E. Shapley, Charles C. Steidel, Dawn K. Erb, Naveen A. Reddy, Kurt L. Adelberger, Max Pettini, Pauline Barmby, and Jiasheng Huang. Ultraviolet to MidInfrared Observations of Starforming Galaxies at $z \sim 2$: Stellar Masses and Stellar Populations. *The Astrophysical Journal*, 626(2):698–722, March 2005.

- [72] F. H. Shu. Self-similar collapse of isothermal spheres and star formation. *The Astrophysical Journal*, 214:488, June 1977.
- [73] F. H. Shu, F. C. Adams, and S. Lizano. Star formation in molecular clouds - Observation and theory. *ARA&A*, 25:23–81, 1987.
- [74] Ian Smail, S. C. Chapman, A. W. Blain, and R. J. Ivison. The Rest-Frame Optical Properties of SCUBA Galaxies. *The Astrophysical Journal*, 616(1):71–85, December 2004.
- [75] Ian Smail, J. E. Geach, A. M. Swinbank, K. Tadaki, V. Arumugam, W. Hartley, O. Almaini, M. N. Bremer, E. Chapin, S. C. Chapman, A. L. R. Danielson, A. C. Edge, D. Scott, C. J. Simpson, J. M. Simpson, C. Conselice, J. S. Dunlop, R. J. Ivison, A. Karim, T. Kodama, A. Mortlock, E. I. Robson, I. Roseboom, A. P. Thomson, P. P. van der Werf, and T. M. A. Webb. The SCUBA-2 Cosmology Legacy Survey: Ultraluminous star-forming galaxies in a $z = 1.6$ cluster. *The Astrophysical Journal*, 782(1):19, December 2014.
- [76] C. Steidel, K. Adelberger, M. Dickinson, M. Giavalisco, M. Pettini, and M. Kellogg. A Large Structure of Galaxies At Redshift $z \sim 3$ and its Cosmological Implications. *The Astrophysical Journal*, Volume 492, Issue 2, pp. 428-438., 492:428–438, August 1997.
- [77] C. C. Steidel, K. L. Adelberger, A. E. Shapley, M. Pettini, M. Dickinson, and M. Giavalisco. Lyman Alpha Imaging of a Proto-Cluster Region at $z=3.09$. *The Astrophysical Journal*, Volume 532, Issue 1, pp. 170-182., 532:170–182, October 1999.
- [78] Charles C. Steidel, Kurt L. Adelberger, Alice E. Shapley, Dawn K. Erb, Naveen A. Reddy, and Max Pettini. Spectroscopic Identification of a Proto-Cluster at $z=2.300$: Environmental Dependence of Galaxy Properties at High Redshift. *The Astrophysical Journal*, Volume 626, Issue 1, pp. 44-50., 626:44–50, February 2005.
- [79] Charles C Steidel, Kurt L Adelberger, Alice E Shapley, Max Pettini, Mark Dickinson, and Mauro Giavalisco. Lyman break galaxies at redshift $z \sim 3$: survey description and full data set 1. *ApJ*, 592(2):728–754, 2003.
- [80] Charles C Steidel, Milan Bogosavljevi, Alice E Shapley, Juna A Kollmeier, Naveen A Reddy, and Dawn K Erb. Diffuse lyman alpha emitting halos: A generic property of high redshift star forming galaxies. *ApJ*, 736:160, 2011.
- [81] Charles C. Steidel, Alice E. Shapley, Max Pettini, Kurt L. Adelberger, Dawn K. Erb, Naveen A. Reddy, and Matthew P. Hunt. $\lesssim 2.5$ Redshift Desert: Overview. *The Astrophysical Journal*, 604(2):534–550, January 2004.

- [82] A. M. Stutz, J. J. Tobin, T. Stanke, S. T. Megeath, W. J. Fischer, T. Robitaille, T. Henning, B. Ali, J. Di Francesco, E. Furlan, L. Hartmann, M. Osorio, T. L. Wilson, L. Allen, O. Krause, and P. Manoj. A Herschel and APEX Census of the Reddest Sources in Orion: Searching for the Youngest Protostars. *ApJ*, 767:36, April 2013.
- [83] J. Stutzki and R. Guesten. High spatial resolution isotopic CO and CS observations of M17 SW - The clumpy structure of the molecular cloud core. *ApJ*, 356:513–533, June 1990.
- [84] A. M. Swinbank, J. M. Simpson, Ian Smail, C. M. Harrison, J. A. Hodge, A. Karim, F. Walter, D. M. Alexander, W. N. Brandt, C. de Breuck, E. da Cunha, S. C. Chapman, K. E. K. Coppin, A. L. R. Danielson, H. Dannerbauer, R. Decarli, T. R. Greve, R. J. Ivison, K. K. Knudsen, C. D. P. Lagos, E. Schinnerer, A. P. Thomson, J. L. Wardlow, A. Wei??, and P. van der Werf. An ALMA survey of sub-millimetre galaxies in the extended chandra deep field south: The far-infrared properties of SMGs. *Monthly Notices of the Royal Astronomical Society*, 438(2):1267–1287, 2014.
- [85] Richard C. Tolman. On the Estimation of Distances in a Curved Universe with a Non-Static Line Element. *Proceedings of the National Academy of Sciences of the United States of America*, 16(7):511, July 1930.
- [86] Kim-Vy H. Tran, Casey Papovich, Amélie Saintonge, Mark Brodwin, James S. Dunlop, Duncan Farrah, Keely D. Finkelstein, Steven L. Finkelstein, Jennifer Lotz, Ross J. McLure, Ivelina Momcheva, and Christopher N. A. Willmer. Reversal of fortune: Confirmation of an increasing star formation–density relation in a cluster at $z = 1.62$. *The Astrophysical Journal*, 719(2):L126–L129, May 2010.
- [87] E. I. Vorobyov and S. Basu. Variable Protostellar Accretion with Episodic Bursts. *ApJ*, 805:115, June 2015.
- [88] D. Ward-Thompson, P. André, R. Crutcher, D. Johnstone, T. Onishi, and C. Wilson. An Observational Perspective of Low-Mass Dense Cores II: Evolution Toward the Initial Mass Function. *Protostars and Planets V*, pages 33–46, 2007.
- [89] D. Ward-Thompson, J. Di Francesco, J. Hatchell, M. R. Hogerheijde, D. Nutter, P. Bastien, S. Basu, I. Bonnell, J. Bowey, C. Brunt, J. Buckle, H. Butner, B. Cavanagh, A. Chrysostomou, E. Curtis, C. J. Davis, W. R. F. Dent, E. van Dishoeck, M. G. Edmunds, M. Fich, J. Fiege, L. Fissel, P. Friberg, R. Friesen, W. Frieswijk, G. A. Fuller, A. Gosling, S. Graves, J. S. Greaves, F. Helmich, R. E. Hills, W. S. Holland, M. Houde, R. Jayawardhana, D. Johnstone, G. Joncas, H. Kirk, J. M. Kirk, L. B. G. Knee, B. Matthews, H. Matthews, C. Matzner, G. H. Moriarty-Schieven, D. Naylor, R. Padman, R. Plume, J. M. C. Rawlings, R. O. Redman, M. Reid, J. S. Richer, R. Shipman, R. J. Simpson, M. Spaans,

- D. Stamatellos, Y. G. Tsamis, S. Viti, B. Weferling, G. J. White, A. P. Whitworth, J. Wouterloot, J. Yates, and M. Zhu. The James Clerk Maxwell Telescope Legacy Survey of Nearby Star-forming Regions in the Gould Belt. *PASP*, 119:855–870, August 2007.
- [90] J. L. Wardlow, Ian Smail, K. E. K. Coppin, D. M. Alexander, W. N. Brandt, A. L. R. Danielson, B. Luo, A. M. Swinbank, F. Walter, A. Weiss, Y. Q. Xue, S. Zibetti, F. Bertoldi, A. D. Biggs, S. C. Chapman, H. Dannerbauer, J. S. Dunlop, E. Gawiser, R. J. Ivison, K. K. Knudsen, A. Kovacs, C. G. Lacey, K. M. Menten, N. Padilla, H. W. Rix, and P. P. van der Werf. The LABOCA survey of the Extended Chandra Deep Field South: A photometric redshift survey of submillimetre galaxies. *MNRAS*, page 31, June 2011.
- [91] Tracy Webb, Daniel O’Donnell, Howard K. C. Yee, David Gilbank, Kristen Coppin, Erica Ellingson, Ashley Faloon, James E. Geach, Mike Gladders, Allison Noble, Adam Muzzin, Gillian Wilson, and Renbin Yan. The Evolution of Dusty Star formation in Galaxy Clusters to $z = 1$: Spitzer IR Observations of the First Red-Sequence Cluster Survey. *The Astronomical Journal, Volume 146, Issue 4, article id. 84, 13 pp. (2013).*, 146:1–16, April 2013.
- [92] J. P. Williams, E. J. de Geus, and L. Blitz. Determining structure in molecular clouds. *ApJ*, 428:693–712, June 1994.
- [93] Min S. Yun, K. S. Scott, Yicheng Guo, I. Aretxaga, M. Giavalisco, J. E. Austermann, P. Capak, Yuxi Chen, H. Ezawa, B. Hatsukade, D. H. Hughes, D. Iono, S. Johnson, R. Kawabe, K. Kohno, J. Lowenthal, N. Miller, G. Morrison, T. Oshima, T. A. Perera, M. Salvato, J. Silverman, Y. Tamura, C. C. Williams, and G. W. Wilson. Deep 1.1mm-wavelength imaging of the GOODS-S field by AzTEC/ASTE - II. Redshift distribution and nature of the submillimetre galaxy population. *Monthly Notices of the Royal Astronomical Society*, 420(2):957–985, September 2012.

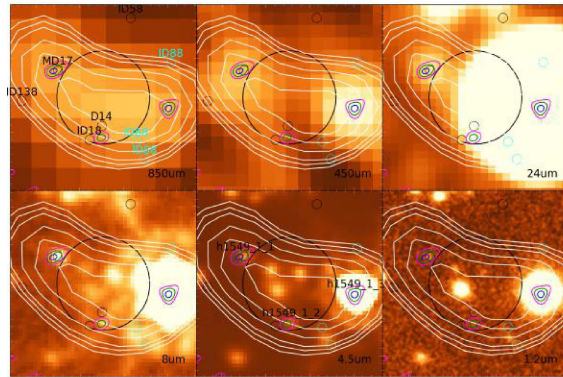
Appendix A

30×30 -arcsec² multi-wavelength cutouts of each 850 μm SCUBA-2 source from Tables [2.1](#) and [2.2](#). From left to right: **Top:** SCUBA-2 850 μm , SCUBA-2 450 μm , *Spitzer*-MIPS 24 μm . **Bottom:** *Spitzer*-IRAC *ch4* 8 μm , *Spitzer*-IRAC *ch2* 4.5 μm , 1.2 μm R-band. We used *Spitzer*-IRAC *ch3* 5.6 μm and *Spitzer*-IRAC *ch1* 3.6 μm when *ch4* and *ch2* were unavailable. The green circles represent the IRAC ID's shown in Tables [2.3](#) and [2.4](#). LBGs are shown as black circles if they reside within the protocluster, red circles if they are at $z > z_{\text{protocluster}}$ and cyan circles if they are at $z < z_{\text{protocluster}}$. The black circle at the centre of each cutout represents an effective 15'' SCUBA-2 beam at 850 μm . The white contours represent SNR levels of (4, 5, 6, 8, 10, 12) at 850 μm .

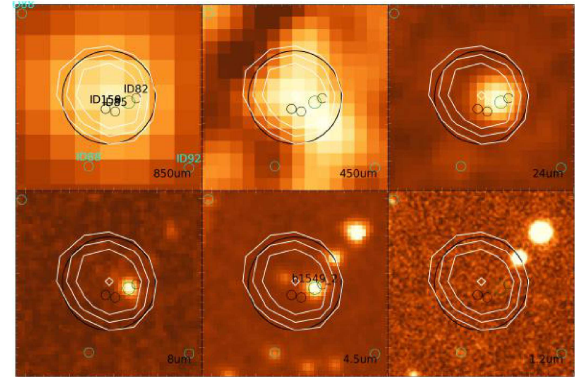
HS1549 Cutouts

The multi-wavelength cutouts for *1549_1* – *1549_29* are found throughout the next four pages.

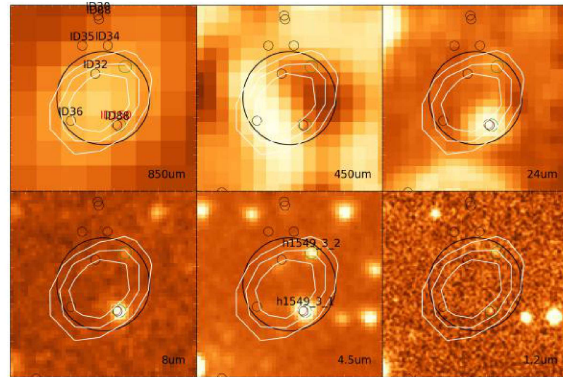
1549_1



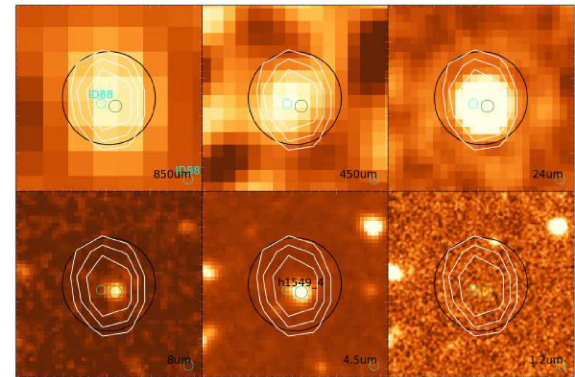
1549_2



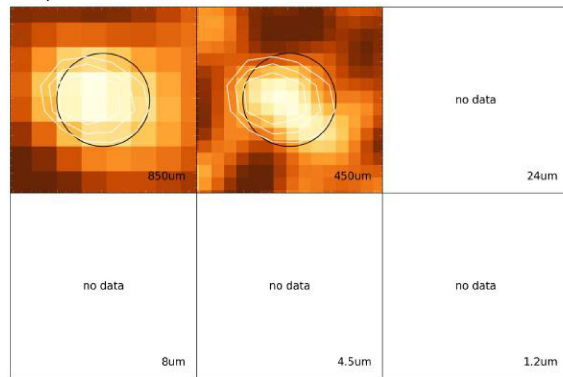
1549_3



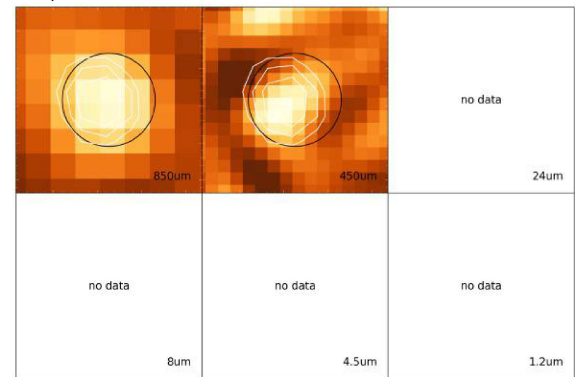
1549_4



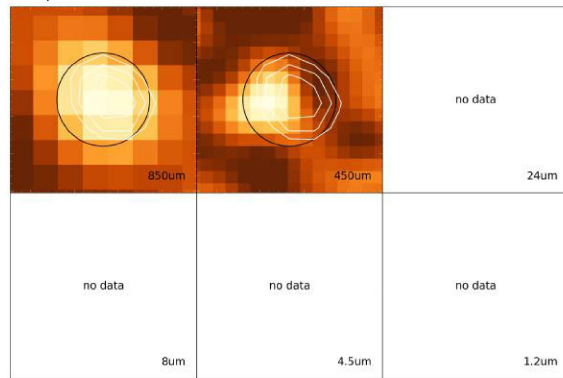
1549_5



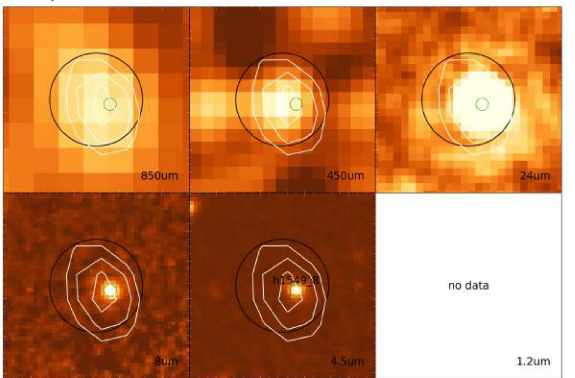
1549_6



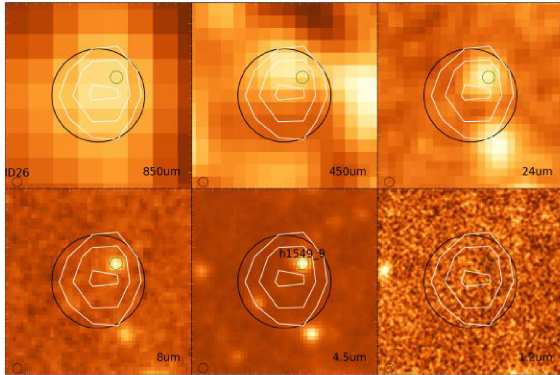
1549_7



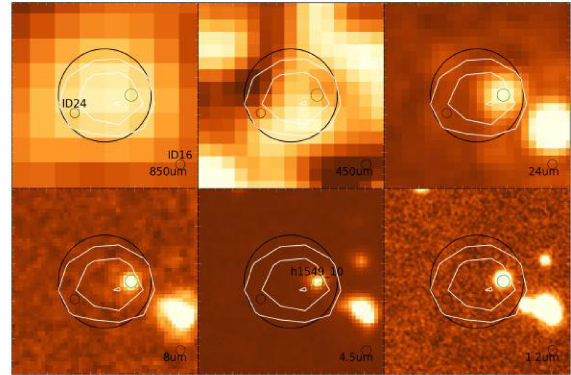
1549_8



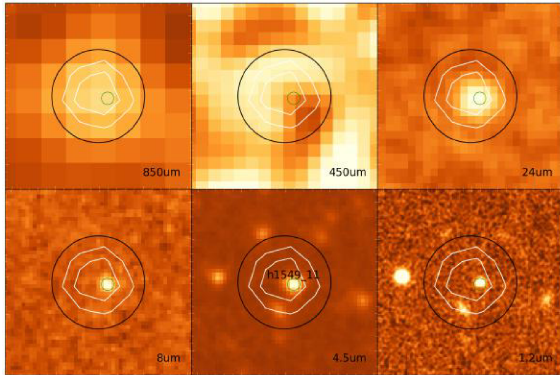
1549_9



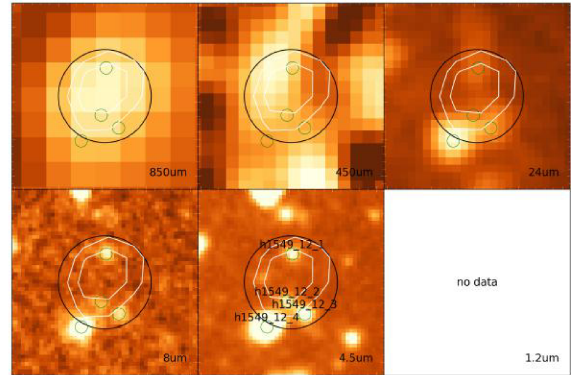
1549_10



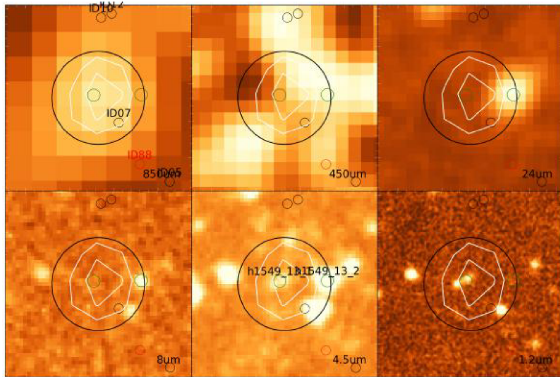
1549_11



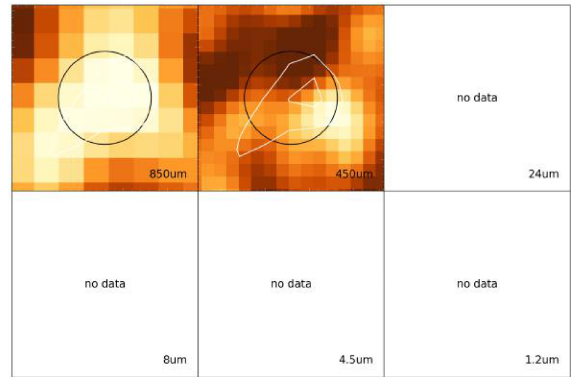
1549_12



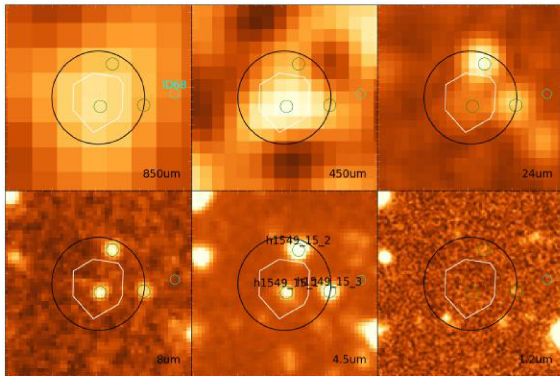
1549_13



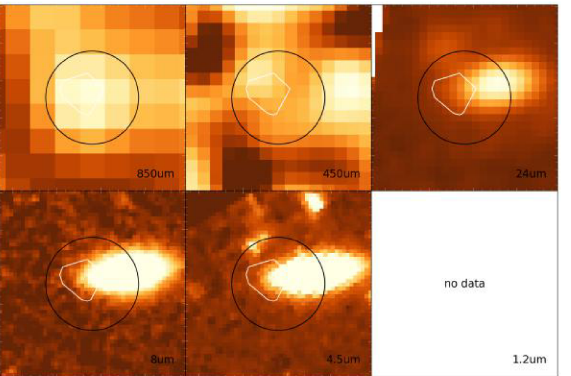
1549_14



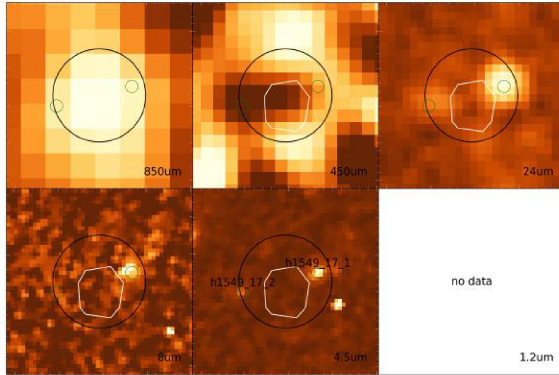
1549_15



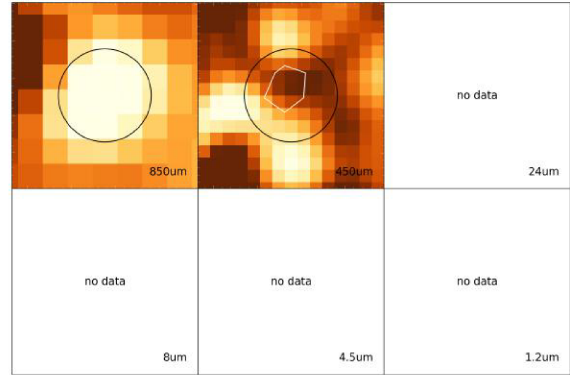
1549_16



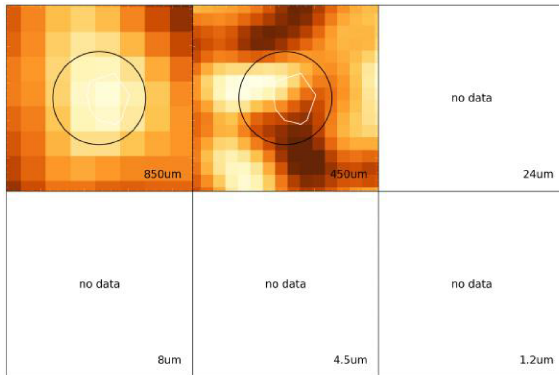
1549_17



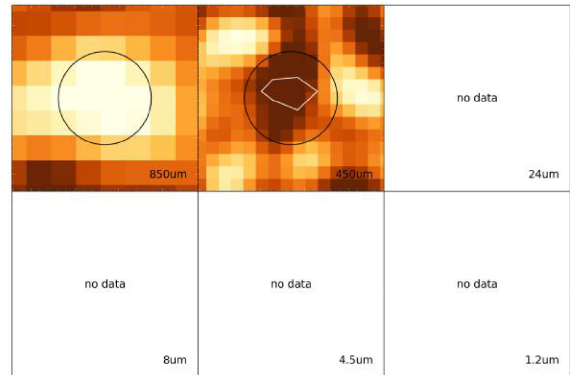
1549_18



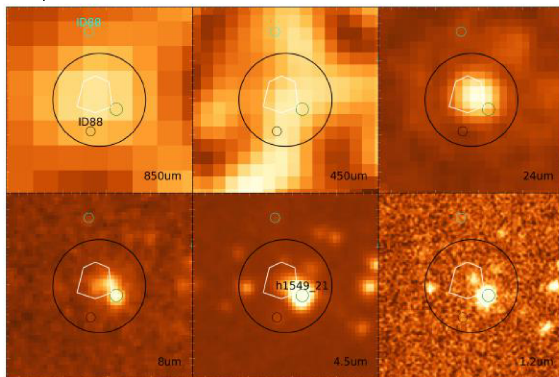
1549_19



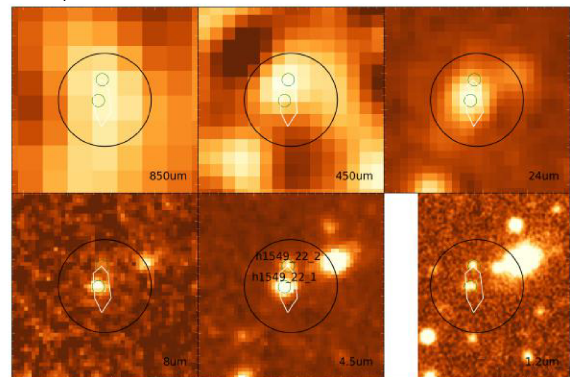
1549_20



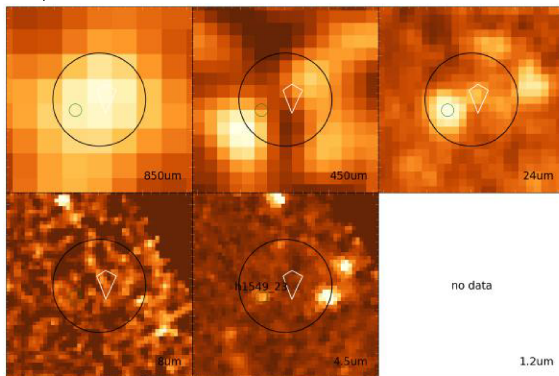
1549_21



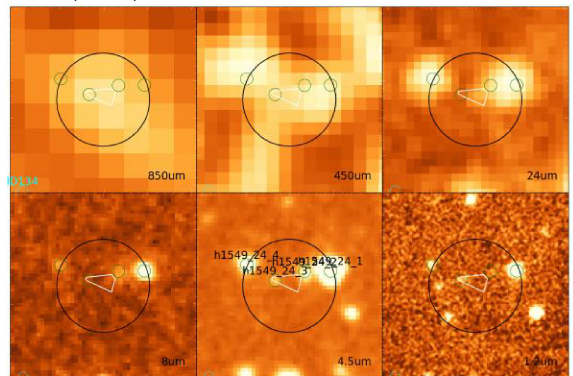
1549_22



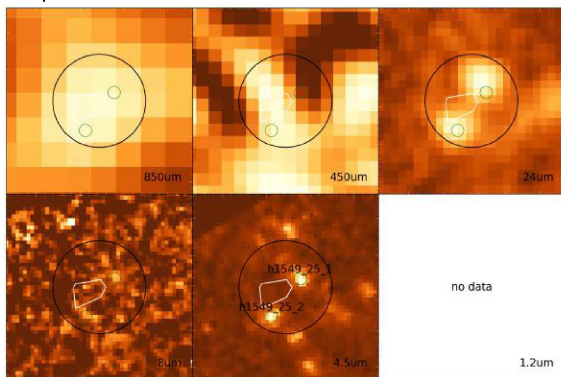
1549_23



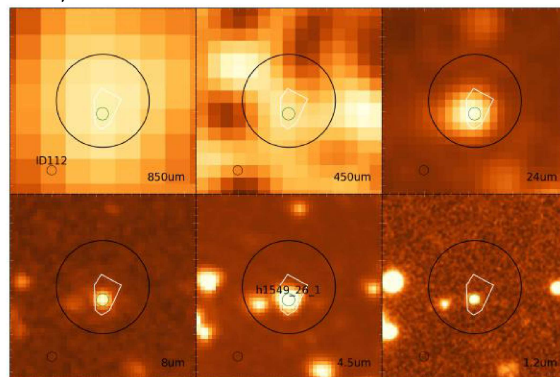
1549_24



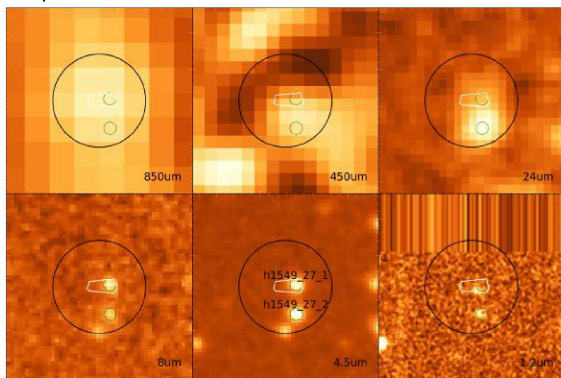
1549_25



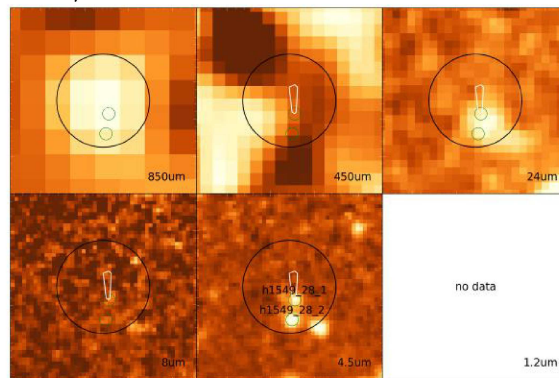
1549_26



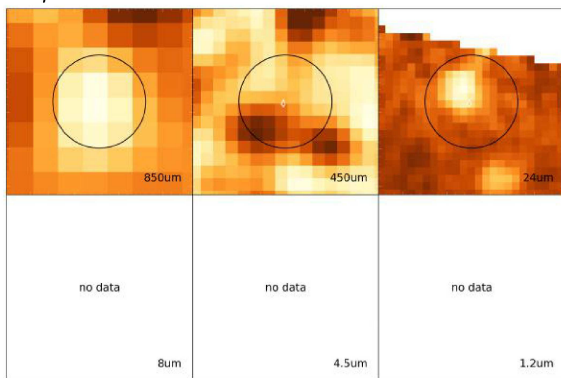
1549_27



1549_28



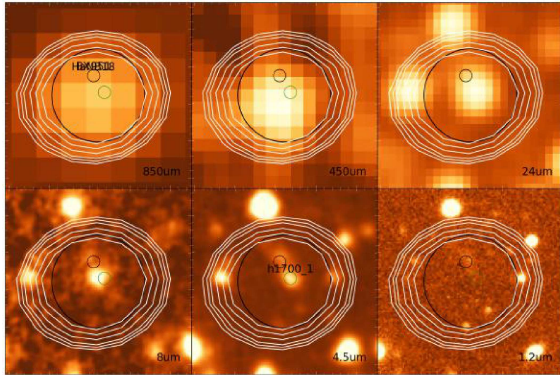
1549_29



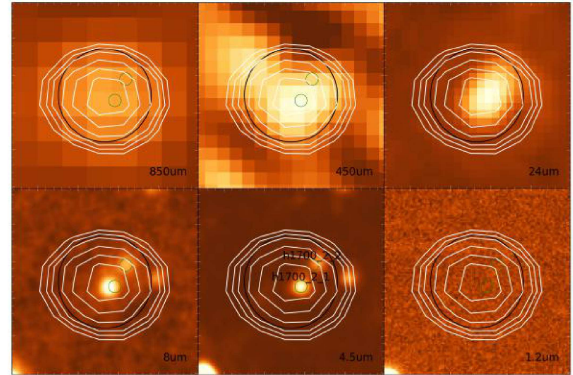
HS1700 Cutouts

The multi-wavelength cutouts for *1700_1* – *1700_27* are found throughout the next four pages.

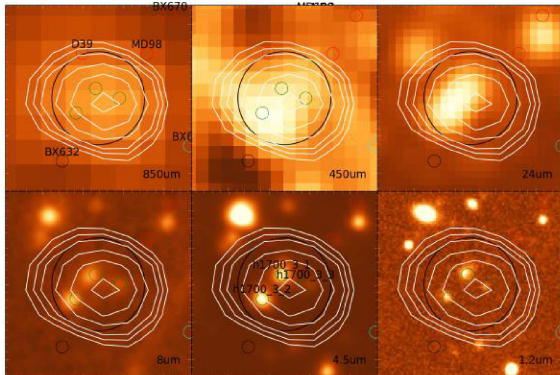
1700_1



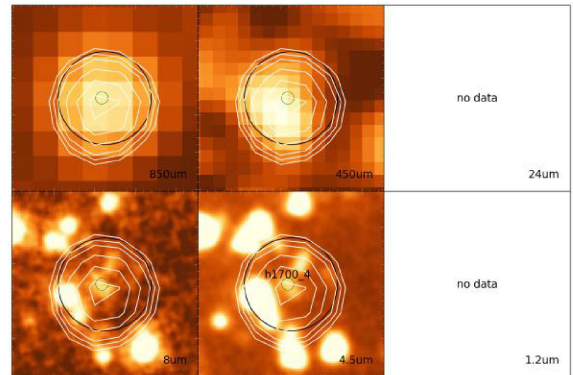
1700_2



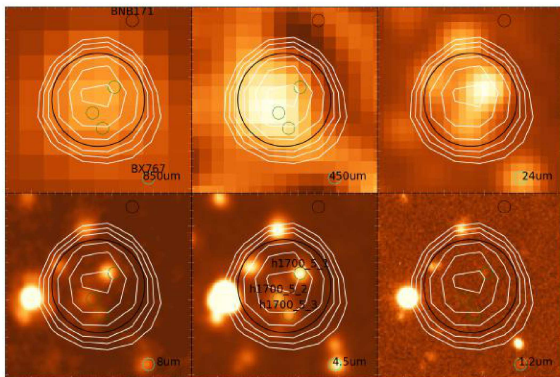
1700_3



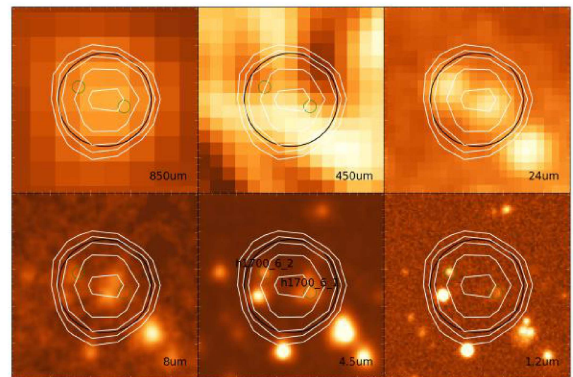
1700_4



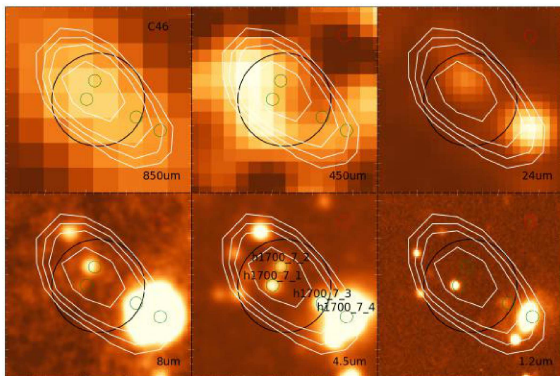
1700_5



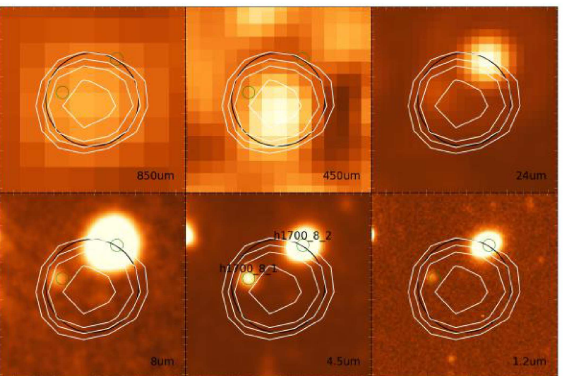
1700_6



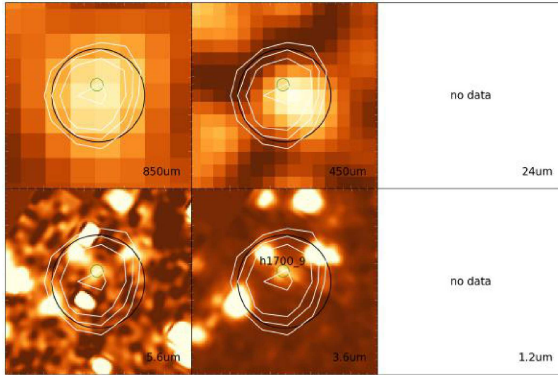
1700_7



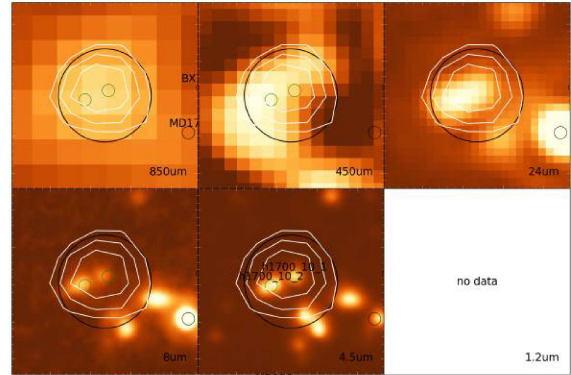
1700_8



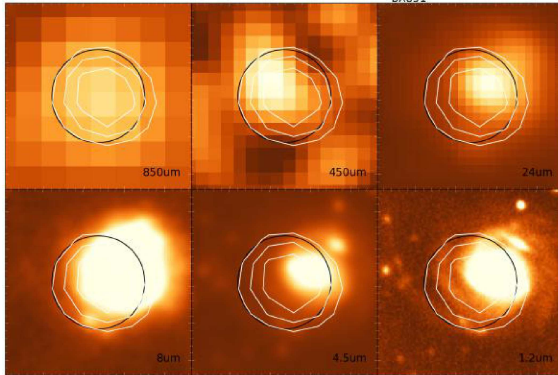
1700_9



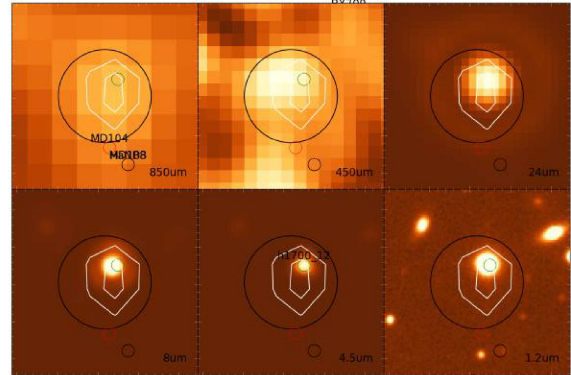
1700_10



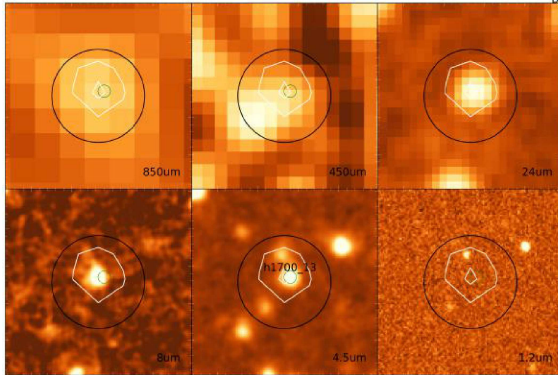
1700_11



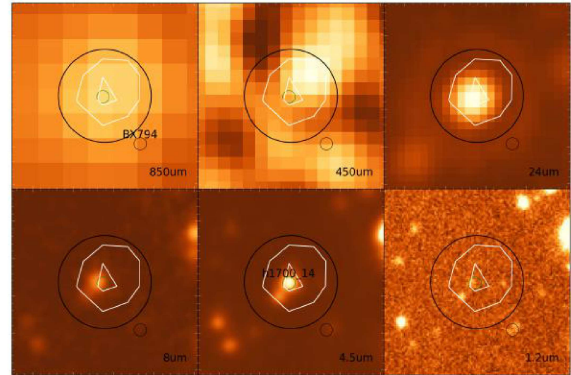
1700_12



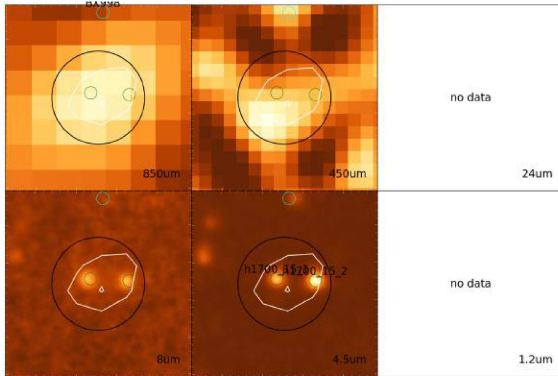
1700_13



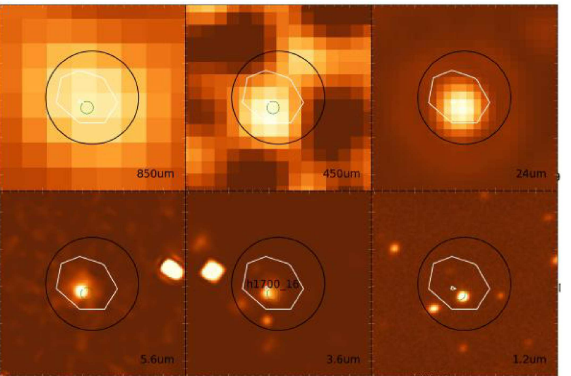
1700_14



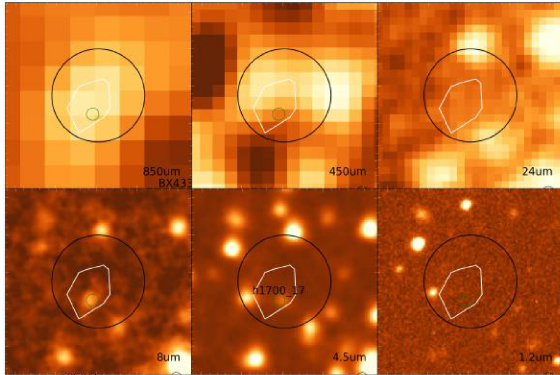
1700_15



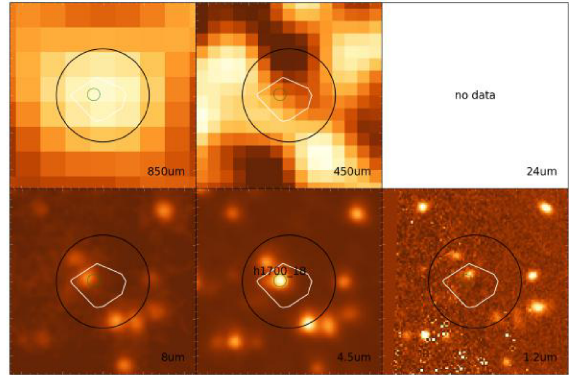
1700_16



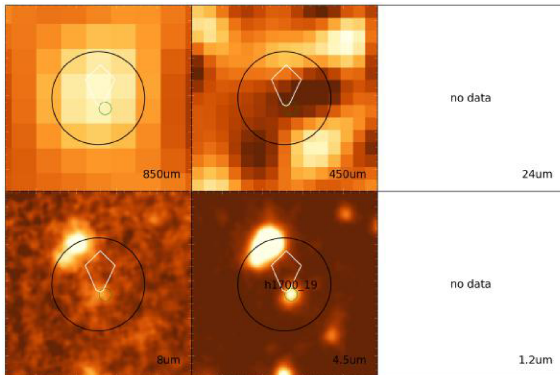
1700_17



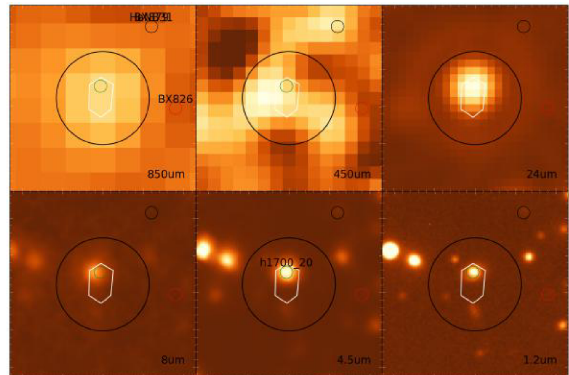
1700_18



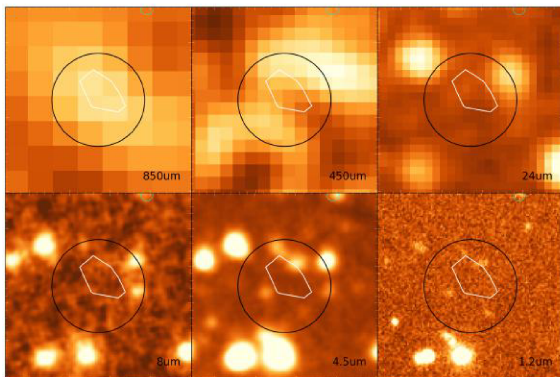
1700_19



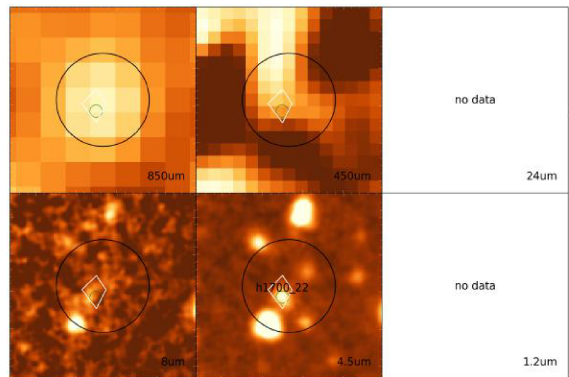
1700_20



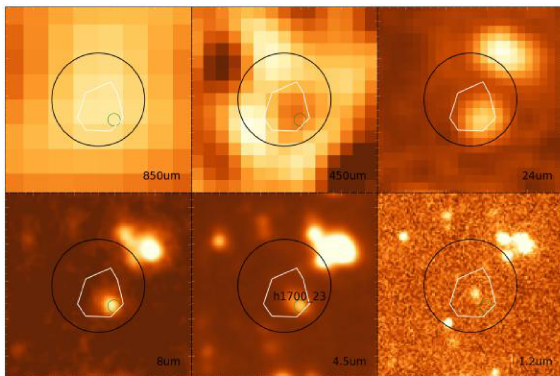
1700_21



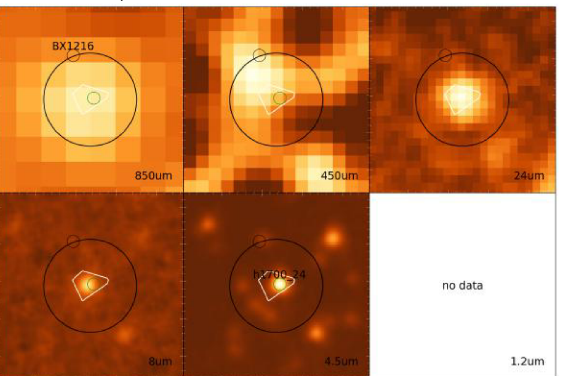
1700_22



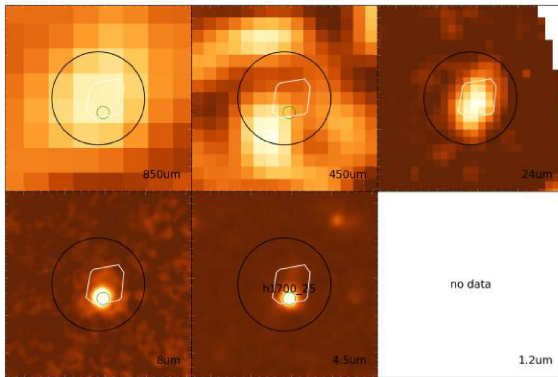
1700_23



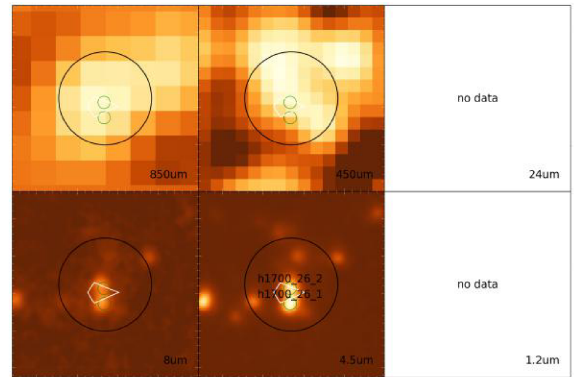
1700_24



1700_25



1700_26



1700_27

